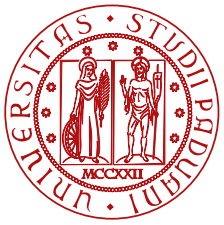

UNIVERSITÀ
DEGLI STUDI
DI PADOVA

Università degli Studi di Padova

Dipartimento di Ingegneria Industriale DII

Corso di Laurea Magistrale in Ingegneria dei Materiali

Study of the effect of hot forging and continuous cooling on the precipitation of secondary phases and corrosion properties of UNS J93380 duplex stainless steel

Relatore Ing. Luca Pezzato

Laureando Emma Pitacco

Correlatore Ing. Mirko Pigato

Matricola 2052484

Anno Accademico 2023-2024

09/04/2024

A mia nonna Bianca,
che mi dice sempre che avrei dovuto
studiare qualcosa di più semplice

Abstract

Owing to their dual-phase morphology, duplex stainless steels offer an excellent compromise in terms of corrosion resistance and mechanical properties. Upon thermo-mechanical processing, these alloys are subject to the precipitation of intermetallic phases such as sigma (σ), chi (χ) and chromium nitrides, which might severely affect their overall performance. The objective of the present work is to evaluate the effect of hot forging on secondary phases in cast UNS J93380 super duplex stainless steels, characterized by the addition of copper and tungsten, which make them particularly suitable when employed in environments containing high amounts of chlorides. The hot forging simulations were carried out at a solution annealing temperature of 1100 °C, followed by continuous cooling at various rates to determine how they affect the kinetics of precipitation. Secondary phases were quantified and investigated by means of both microstructural analysis and corrosion testing. Specifically, DL-EPR technique was employed to test the material's behaviour towards intergranular corrosion and obtain the degree of sensitization of the specimens, which was then compared to the volume fraction of secondary phase precipitates to assess how the two variables might relate to each other. Pitting corrosion resistance of the steel was also evaluated by means of potentiodynamic polarization and critical pitting temperature measurements, to investigate the correlation between pitting and sensitization. The study revealed that hot forging and slow cooling rates always cause an increase in the precipitation of σ and χ as well as a decay in the corrosion properties, also confirmed by macroindentation measurements. On the other hand, rapid cooling favours the precipitation of quenched-in nitrides, which were demonstrated to aggravate the corrosion performance in terms of both IGC and pitting. To overcome such precipitation issues during forging, a possibility would be to perform an intermediate cooling step at low rate and quenching from lower temperatures. In addition to this, heating to higher solubilization temperatures and applying a higher degree of deformation should also be considered to enhance recrystallization.

In virtù della loro natura bifasica, gli acciai inossidabili duplex costituiscono un eccellente compromesso in termini di resistenza alla corrosione e proprietà meccaniche. Quando soggette a trattamenti termo-meccanici, le leghe duplex subiscono la precipitazione di fasi intermetalliche quali sigma (σ), chi (χ) e nitruri di cromo, che portano ad un drastico peggioramento delle prestazioni del materiale. L'obiettivo del presente lavoro è quello di valutare l'effetto della forgiatura a caldo sulle fasi secondarie nella lega duplex da fonderia UNS J93380, caratterizzata dalla presenza di rame e tungsteno, che ne migliorano il comportamento in ambienti ad alto contenuto di cloruri. I test di forgiatura a caldo sono stati realizzati ad una temperatura di solubilizzazione di 1100 °C, seguiti da un raffreddamento continuo a varie velocità per determinarne l'influenza sulla cinetica di precipitazione. La quantificazione delle fasi secondarie è stata effettuata sia attraverso un'analisi microstrutturale che per mezzo di test a corrosione. In particolare, è stata utilizzata la tecnica DL-EPR per testare il comportamento del materiale nei confronti della corrosione intergranulare e per ottenere il grado di sensibilizzazione dei campioni, il quale è stato poi comparato alla frazione volumetrica delle fasi secondarie precipitate, in modo tale da trovare una correlazione tra le due variabili. Inoltre è stata valutata la resistenza della lega al pitting tramite test di polarizzazione anodica e temperatura critica di pitting, per verificare la relazione tra corrosione per pitting e sensibilizzazione. Lo studio ha rivelato che la forgiatura a caldo associata a una velocità di raffreddamento lenta è sempre causa di precipitazione di fasi σ e χ, oltre che di una riduzione della resistenza a corrosione, confermato anche dalle prove di macrodurezza. D'altro canto, velocità di raffreddamento rapide promuovono la formazione di nitruri di tipo *quenched-in* che, come dimostrato da vari studi, peggiorano il comportamento a corrosione sia intergranulare che di pitting. Per aggirare i problemi di precipitazione che si innescano durante la forgiatura, si potrebbe considerare uno step di raffreddamento intermedio a bassa velocità seguito da tempra a temperature più elevate. Inoltre, è possibile effettuare un riscaldamento a temperature di solubilizzazione più alte e applicare un grado di deformazione maggiore per promuovere il fenomeno di ricristallizzazione.

Contents

1 Introduction **1**

1.1 Duplex Stainless Steels (DSS) . . . 1

1.1.1 A brief overview . . . 1

1.1.2 Role of alloying elements . . . 2

1.1.3 Metallurgy of duplex stainless steels . . . 4

1.1.4 Characteristics and morphology of precipitates . . . 6

1.1.5 Hot deformation behaviour of DSSs . . . 9

1.1.6 Continuous cooling regime . . . 12

1.2 Corrosion of Duplex Stainless Steels . . . 14

1.2.1 Pitting corrosion . . . 14

1.2.2 Crevice corrosion . . . 15

1.2.3 Stress corrosion cracking (SCC) . . . 16

1.2.4 Intergranular corrosion (IGC) . . . 18

1.3 Testing . . . 19

1.3.1 Double Loop Electrochemical Potentiokinetic Reactivation (DL-EPR) . . . 19

1.3.2 Anodic polarization . . . 22

1.3.3 Critical pitting temperature (CPT) . . . 22

1.4 Reasons and objectives of the thesis . . . 24

2 Materials and methods **27**

2.1 UNS J93380 duplex stainless steel . . . 27

2.2 Experimental set-up . . . 29

2.2.1 Processing . . . 29

2.2.2 Microstructural, crystallographic and hardness characterization . . . 32

2.2.3 Electrochemical characterization . . . 33

3 Experimental results **35**
3.1 Microstructural analysis 35
3.1.1 Primary phase quantification 35
3.1.2 Secondary phase quantification 36
3.1.3 EBSD analysis 44
3.2 Hardness evaluation 50
3.3 Corrosion tests 52
3.3.1 DL-EPR results 52
3.3.2 Anodic polarization results 63
3.3.3 CPT results 64

4 Conclusions **71**

Bibliography **77**

List of Figures

1.1 Basic crystallographic structures: a) body-centered cubic (ferrite) and b) face-centered cubic (austenite), after reference [4] 3
1.2 Equilibrium diagram of SAF2507 using Cr% as a variable, after reference [1] . 5
1.3 Schaeffler diagram showing stable phases for a given alloy composition after heating to 1050°C for 30 minutes and quenching in water, after reference [5] . . 5
1.4 Precipitation diagram of duplex stainless steels, after reference [6] 7
1.5 Example of secondary phase precipitation in Zeron100 sample continuously cooled at 0.7 °C/s at lower (a) and higher (b) magnification (source:[7]) 7
1.6 SEM-BSE of 2507: left (900 °C, 5 min) and right (950 °C, 40 min) nitrides and chi-phase transforming to sigma-phase (source: [8]) 8
1.7 Comparison of the mechanical properties values of austenitic, ferritic and solution annealed duplex stainless steels, after reference [9] 10
1.8 Hot working range for various duplex grades (source:[4]) 11
1.9 Average depth of dissolution after corrosion testing for each phase versus deformation temperature for ferrite and austenite phases (source: [15]) 11
1.10 Open-die forging in the ideal case (a, b) and with barreling effect (c), after reference [17] 12
1.11 Examples of continuous cooling from solution annealing temperature: at slow rates (B) σ-phase may be formed, while fast cooling (A) avoids it (source: [4]) 13
1.12 Pitting morphologies of UNS S32760 DSS at different surface roughnesses, after reference [19] 14
1.13 PREn plotted against CPT of commercially available DSSs, showing a linear correlation (source: [1]) 16
1.14 Depth of crevice corrosion in seawater at 16°C with 1mg/L chlorine, after reference [20] 17
1.15 SCC in the gauge length of a duplex stainless steel specimen strained to failure in NACE-01-77 solution at 20°C (source:[21]) 17

1.16 Effect of nickel content on stress intensity factor KISCC (source: [1]) 18
1.17 Representation of Cr carbides precipitation and profile of %Cr at grain boundaries (source:[22]) 19
1.18 Effect of DL-EPR on aged UNS S31250 DSS with 33 pct H2SO4 + 0.3 pct HCl at 20 °C and a scan rate of 2.5 mV/s, after reference [23] 20
1.19 Schematic representation of a DL-EPR curve (source:[28]) 21
1.20 Microstructural aspects of aged UNS S32750 DSS before and after DL-EPR, obtained by SEM (source:[29]) 21
1.21 a) Anodic characteristic of an active-passive metal, from [22] and b) typical potentiodynamic anodic polarization plot from ASTM G5-14 standard [30] . . 23
1.22 a) CPT determined by a potentiodynamic technique for duplex unwelded sheets in 1M NaCl, after reference [2]; b) Determination of CPT, after ASTM G150-18 standard [35] 23

2.1 Typical microstructure of DSS in cast form, source:[37] 27
2.2 Common cast duplex grades listed in the Unified Numbering System (source: [2]) 28
2.3 a) 0.1 mm/yr iso-corrosion curves in sulphuric acid plus 2000 ppm chloride; b) CPT data for wrought stainless steels in sea water plotted against PREN (source: [2]) 29
2.4 Picture of AR (left) and post-compression (right) specimens 30
2.5 Schematic representation of the two experiments, without and with deformation 31
2.6 Example of image analysis with ImageJ software 32
2.7 Three-electrode cell (a) and schematic diagram of specimen holder, after ASTM G61-86 standard [40] (b) 34

3.1 BSE micrographs showing the microstructure of AR sample obtained after electrolytic etching with 20% NaOH at 300x magnification 35
3.2 Optical micrographs after electrolytic etching in 20% NaOH 38
3.3 SEM-BSE secondary phase morphologies after electropolishing for 20 s at 21 V of continuously cooled specimens: a) at 10 °C/s DEF, b) at 0.25 °C/s ND . . 39
3.4 Morphology of σ and γ_2 secondary phases precipitated in sample F025 in SEM-BSE (left) and SEM-SE (right) images 39
3.5 Morphology of intergranular nitrides precipitated at γ/δ interface in sample F10 in SEM-BSE (left) and SEM-SE (right) images 40
3.6 SEM-BSE image sample F05 after mechanical polishing 41
3.7 SEM-BSE image of intergranular nitrides precipitated in sample F1 42

3.8 SEM-BSE images of a) sample S05 after mechanical polishing; b) morphology of intragranular rodlike nitride colonies in sample SQ after electropolishing . . 43
3.9 SEM-BSE morphology of re-crystallized austenite after deformation in sample F10 43
3.10 GROD maps 45
3.11 IPF of specimens SQ and FQ 46
3.12 IPF of specimen F025 with zoom on austenite twinning crystals 47
3.13 Phase map of specimen F025 with zoom on allotriomorphic austenite bulging from δ/δ interfaces 48
3.14 Histogram of hardness level trend 50
3.15 Linear DL-EPR polarization plots of selected samples without deformation (a) and post-deformation (b) with local zoom where I_r appears 53
3.16 DL-EPR parameters of specimens without deformation with different cooling rates obtained in solutions of 33% H_2SO_4 + 2.5% HCl at 1.68 mV/s: a) Ia, Ir; b) DOS % 54
3.17 DL-EPR parameters of specimens with 50% true deformation with different cooling rates obtained in solutions of 33% H_2SO_4 + 2.5 % HCl at 1.68 mV/s: a) Ia, Ir; b) DOS % 55
3.18 DL-EPR polarization plots in 33% H_2SO_4 + 2.5% HCl at 1.68 mV/s 56
3.19 DL-EPR plots of sample F05 and S025 58
3.20 Optical micrographs of specimens after DL-EPR 59
3.21 Schematic representation of the heat treatment of thin- and thick-walled components, after reference [6] 60
3.22 SEM-SE images at 2000x mag. of microstructural evolution of the samples after DL-EPR, before (left) and after (right) hot forging; examples of sensitized areas are highlighted with dashed circlets 62
3.23 Potentiodynamic anodic polarization curves obtained in 3.5% NaCl solution at 0.3 mV/s 63
3.24 Evaluation of CPT in UNS J93380 with potentiostatic measurements of various continuous cooling rates 65
3.25 CPT results 66
3.26 SEM-BSE pit morphologies on the surface of specimen F025 after CPT test (2000x mag.) 67

3.27 SEM-SE images at 1000x (left) and 2000x mag. (right) of pit morphologies after CPT on specimens: a), b) S025; c), d) Sstep; images e), f): comparison between SEM-SE and BSE at 2000x mag. of pit formed on simply quenched sample 69

4.1 Correlation between the DOS and CPT of UNS J93380 in various thermo-mechanical processing conditions 74

List of Tables

2.1 Chemical composition of the super duplex UNS J93380 in weight % 29
2.2 Classification of the samples based on thermo-mechanical processing parameters 29

3.1 Ferrite volume fraction calculated by IA 36
3.2 Intermetallic phases content at different cooling rates and deformation degree, from 1100 °C 42
3.3 Vickers hardness measurements with 10 kg load 50
3.4 Parameters obtained from anodic polarization plots in 3.5% NaCl solution at 0.3 mV/s 64
3.5 Critical pitting temperatures (CPT) of UNS J93380 in various thermal processing conditions 65

Acknowledgements

First of all, I would like to express my deepest gratitude to my academic supervisor, prof. Luca Pezzato, for being the best and most inspiring teacher I've met during my University years. I also could not have undertaken this journey without the invaluable help and advice of my co-supervisor, Mirko Pigato: thank you for not banishing me from the lab after my experiments with acids.
I'm extremely grateful to all the wonderful people I met in the lab, whose kind support and friendship will always be very dear to me. Special thanks go to Alice, Gaja, Amira, Nicolò, Marco, Mattia and Arshad, amongst many others.
Finally, words cannot express my gratitude to my amazing parents, who believed in me when I couldn't believe in myself; to my boyfriend Mattia, who's the only one that really knows the *blood, toil, sweat and tears* I put into this work and who bravely powered through all my whining, and to my brother Giovanni, whose quiet praise is indispensable to me.

Prima di tutto, vorrei esprimere la mia più sincera gratitudine al mio relatore, il prof. Luca Pezzato: grazie per avermi trasmesso l'amore per la metallurgia e per essere stato in assoluto il miglior professore che abbia incontrato durante la mia carriera accademica. Questa ricerca poi non sarebbe stata possibile senza il costante aiuto e gli insegnamenti del mio correlatore, Mirko Pigato: grazie per non avermi cacciata dal laboratorio dopo i miei esperimenti con l'acido.
Sarò sempre infinitamente grata a tutte le persone meravigliose che ho avuto la fortuna di incontrare in laboratorio: Alice, Gaja, Amira, Nicolò, Marco, Mattia, Arshad e tanti altri. Ricorderò sempre con affetto il vostro supporto e amicizia.
Infine, non ci sono parole per descrivere quanto io ringrazi i miei genitori, che hanno sempre creduto in me anche quando io non credevo in me stessa; il mio ragazzo Mattia, l'unico che davvero sa quanto io abbia sudato per portare a termine questa tesi e che con coraggio ha sopportato ogni mia singola lamentela, e mio fratello Giovanni, il cui flemmatico sostegno è per me indispensabile.

Chapter 1

Introduction

1.1 Duplex Stainless Steels (DSS)

1.1.1 A brief overview

Quoting the perfect words of J. O. Nilsson, *duplex* is a latin word which means *two-fold*, referring to the synergistic effect of the ferrite and austenite phases that compose these alloys [1]. In 1927, Bain and Griffiths at U.S. Steel published a paper where phase diagrams of the iron-chromium-nickel system were presented in order to introduce austenite-ferrite alloys with 23 to 30 % chromium and 1.2 to 9.7 % nickel [2]; however, their paper did not provide any information on the properties of such alloys [3]. The first DSS cast dates back to 1930 and was produced in Sweden by Avesta Ironworks (now Outokumpu) for applications such as autoclaves for gunpowder production and valves for sulphite processing in paper manufacturing. However, it was not until 1968 that duplex grades became commercially available, thanks to the outstanding development of Vacuum and Argon Oxygen Decarburization (VOD and AOD), refining processes that allowed to create low carbon and high nitrogen stainless steels. The advent of such techniques was important for the advancement of duplex stainless steels for two main reasons: first, it allowed to replace the early standard austenitic grades, which were prone to intergranular corrosion due to the significant content of carbon; second, it opened the possibility of adding nitrogen as an alloying element, especially beneficial in terms of high temperature stability (mainly regarding the heat affected zone resulting from welding, which suffered from low toughness as well as low corrosion resistance with respect to the base metal). Together with the increasing demand for a stainless steel capable of operating in offshore oil production, these factors contributed to the commercial success of duplex grades.

DSS are commonly characterized by almost equal volume fractions of ferrite and austenite:

the former contributes to the improved mechanical properties and the latter provides not only low temperature toughness but also resistance towards generalized corrosion. Such alloys can therefore be employed in a variety of applications, where a balance between mechanical and corrosion performance is required, such as in oil and refinery heat exchangers, brewing tanks and desalination plants. Since duplex grades find no correspondence in the AISI classification, which is usually employed for austenitic and ferritic stainless steels, the SAF (Sandvik Austenite Ferrite) or the North American UNS (Unified Numbering System) are used. Depending on their alloying elements content, DSS can be divided into four main groups:

- **Lean duplex**, introduced in the market in order to compete with austenitic AISI 316, provides twice the yield strength as well as better resistance to stress corrosion cracking (SCC). Lean DSS are molybdenum-free and have a chemical composition of 20-23 % chromium, 4 % nickel and nitrogen close to the solubility limit of 0.02 % (e.g. SAF 2304);

- **Standard duplex**, with around 22 %Cr, 5 %Ni, 3 %Mo and N $\leq$ 0.2 % (e.g. SAF 2205). They account for 60 % of the duplex use and provide a resistance to localized corrosion intermediate between that of the austenitic grade AISI 317 and the 5-6 % Mo super austenitic alloys;

- **Super duplex**, developed to compete with nickel base alloys, required to withstand severely aggressive chloride-containing environments. Their composition consists of 25 % Cr and 3 % Mo, such as SAF 2507. Their high alloy content sets the main disadvantage of their sensitivity to the precipitation of intermetallic phases;

- **Hyper duplex**, including SAF 2707, characterized by higher Cr and Mo contents with respect to the previous grade. It complements the 2507 grade, providing increased strength and resistance to more aggressive conditions, such as hot seawater and acidic chloride solutions.

1.1.2 Role of alloying elements

In order to obtain a stable and reliable duplex structure, a careful selection of the alloying elements must be carried out. Infact, alloy composition is responsible of microstructure, mechanical properties and, last but not least, corrosion resistance of DSSs. The following is a brief list of the most important alloying elements and their main related function.

- **Chromium** is an α stabilizing element, meaning that it promotes the formation of the body-centered cubic (BCC) structure of iron (i.e. ferrite), as depicted in fig. 1.1. A Cr

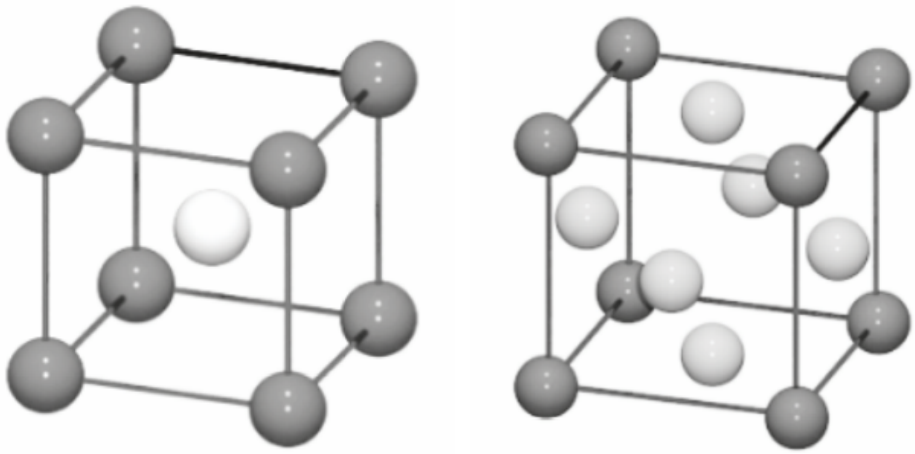

(a) (b)

Figure 1.1: *Basic crystallographic structures: a) body-centered cubic (ferrite) and b) face-centered cubic (austenite), after reference [4]*

content higher than 10.5 % ensures the *passivation* of the steel, that is the formation of a thin surface oxy-hydroxide film ensuring resistance towards localized corrosion. In duplex stainless steels, at least 20 % Cr is required in order to achieve the desired properties. There is however a limit in the beneficial effect provided by the addition of Cr, due to the enhanced precipitation of unwanted secondary phases (see section 1.1.3).

- **Nickel** is an austenite former, which promotes a change in the crystal lattice from BCC to face-centered cubic (FCC); γ stabilizers are required in order to balance the ferrite volume fraction and maintain it to a 40 to 60 %. In duplex grades, Ni content is kept at a 1.5 to 7 % content, which is relatively low compared to 300-series austenitic steels. This not only allows for lower production cost, but also provides excellent resistance against localized corrosion phenomena, such as SCC. Ni infact has been confirmed to increase the stacking-fault energy in stainless steels, meaning that it provides interruptions in the normal stacking sequence of atomic planes in the steel crystal structure, inhibiting the propagation of cracks. Moreover, its presence in half of the microstructure greatly increases the material toughness.

- **Molybdenum** extends the passive potential range and reduces the corrosion current density in the active range. It significantly contributes to the improved pitting and crevice corrosion resistance of DSSs in chloride-containing environments. It is a ferrite former and it is usually restricted to less than 4 % due its tendency to form intermetallic precipitates.

- **Carbon** promotes the formation of austenite and at the same time, being an interstitial

solid solution element, it magnifies hardness and wear resistance through solid solution strengthening. Nevertheless, its content should be kept at a minimum due to the *sensitization* phenomenon, occurring through the precipitation of Cr carbides at grain boundaries.

- **Nitrogen** is by far the most effective solid solution strengthening element and being an austenite stabilizer, it can partially replace the more expensive Ni in stainless steels. It partitions preferentially to the austenite, which has higher solubility towards interstitial elements, and tends to concentrate at the metal-passive film interface. Its presence in the alloy composition allows to delay the formation of intermetallics by promoting short-range ordering and thus reducing Cr-partitioning, improving processing and fabrication of duplex stainless steels. Nitrogen is also associated to an increase of the yield strength of DSSs and of pitting corrosion resistance, as will be seen when PRE number is introduced in section 1.2.1. Nitrogen presence is only beneficial as long as it is completely solubilized in the lattice sites, so provided that nitride precipitation is suppressed. Increased Cr content can improve the solubility of N, although in conjunction with a heightened tendency of CrN formation, thus posing a limitation in the amounts of Cr and N that can be included in the alloying composition.

- **Manganese** expands the austenite phase region and its addition improves the solubility of nitrogen, thus allowing to increase its content without the risk of out-gassing. Mn also has a beneficial effect on hot ductility, thanks to its increased stacking fault energy.

- **Copper** has recently been recognised to increase the corrosion resistance of DSSs in non-oxidizing environments, such as sulphuric acid. This is why some commercial DSSs with 25 % Cr add 0.5 wt.%–1.0 wt.% Cu to reduce corrosion rates and often to convey excellent antibacterial properties to the material. Cu improves the stability of austenite, leading to an increase in strength and plasticity of the steel.

- **Tungsten**, being a ferrite stabilizer, is added in some DSSs up to 2 % in order to broaden the passive potential range and achieve better pitting and crevice corrosion resistance. Such an effect is probably related to tungsten being adsorbed into the passive layer with no change in the oxidation state. The addition of W to the base alloy leads to a delay in the precipitation of secondary phases as well as to a reduction in their volume fraction.

1.1.3 Metallurgy of duplex stainless steels

The metallurgical behaviour of duplex stainless steels can be effectively represented by iron-nickel-chromium ternary phase diagrams. In figure 1.2 a section of the diagram is displayed at 68 % iron, showing that the alloy solidifies ferritically. Austenite starts forming at around

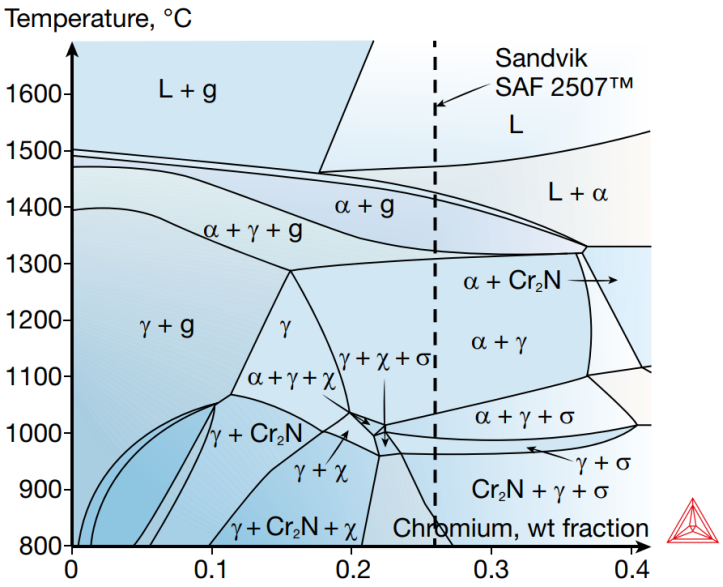

Figure 1.2: *Equilibrium diagram of SAF2507 using Cr% as a variable, after reference [1]*

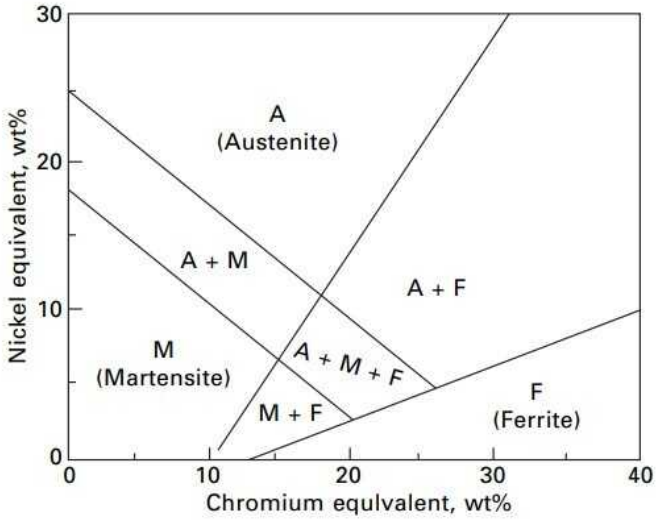

Figure 1.3: *Schaeffler diagram showing stable phases for a given alloy composition after heating to 1050°C for 30 minutes and quenching in water, after reference [5]*

1300 °C and upon cooling its volume fraction gradually increases. The ratio of austenite to ferrite depends on the alloy composition, since individual alloying elements tend to promote formation of either one phase or the other. The end goal in fabrication of DSSs is usually that of obtaining a phase balance close to 45 to 50 % ferrite. In this respect, Schaeffler's diagram (fig. 1.3) is an important tool to achieve a qualitative identification of the type of steel that can be obtained from a certain composition. Specifically, it considers the two contributions given by α-stabilizing elements (included in the *chromium equivalent* Cr_{eq}) and by the γ-stabilizers (expressed as *nickel equivalent* Ni_{eq}):

$$Cr_{eq} = \%Cr + \%Mo + 1.5(\%Si) + 0.5(\%Nb)$$

$$Ni_{eq} = \%Ni + 30(\%C) + 30(\%N) + 0.5(\%Mn)$$

When water quenching from the solution annealing temperature, an elemental distribution close to equilibrium is obtained, represented by islands of austenite evenly distributed in a continuous ferritic matrix. On cooling to 1000 °C and below, detrimental phases can precipitate in a matter of minutes, causing severe reductions in both corrosion and toughness. In the critical temperature range, element diffusion is comparatively slow, so if cooling is performed sufficiently fast, precipitation of secondary phases can be inhibited, which is especially important during welding or after annealing. In the worst case scenario, intermetallic precipitates can only be removed by a complete solubilization treatment followed by water quenching.

1.1.4 Characteristics and morphology of precipitates

A wide spectrum of precipitates can be observed in DSSs, characterized by different morphologies as well as effects on the alloy properties. Their kinetics of formation is controlled either by element solubility or diffusion mechanisms [6]. In the former case, precipitation is inevitable due to cooling rates feasibility limitations (e.g. carbides, nitrides, secondary austenite), while in the latter case phase formation can be effectively suppressed by water quenching, since it avoids prolonged exposure to the critical temperatures (e.g. σ, χ). Most of these microstructural transformations take place in ferrite: the reason of this can be found in its chemical composition, which is enriched in α-stabilizers such as Cr and Mo, which promote precipitation of intermetallics. Moreover, ferrite is characterized by a BCC crystal structure (compactness χ of 68%), which has a majority of octahedral sites and is less compact compared to an austenitic lattice (χ=74%), therefore allowing for element diffusion rates about 100 times faster. In this section a brief description of the most important ones is provided.

- **Sigma (σ) phase** is a hard, embrittling precipitate which forms between 650 and 1000 °C as a δ-ferrite decomposition product. σ phase formation is a significant hazard for the

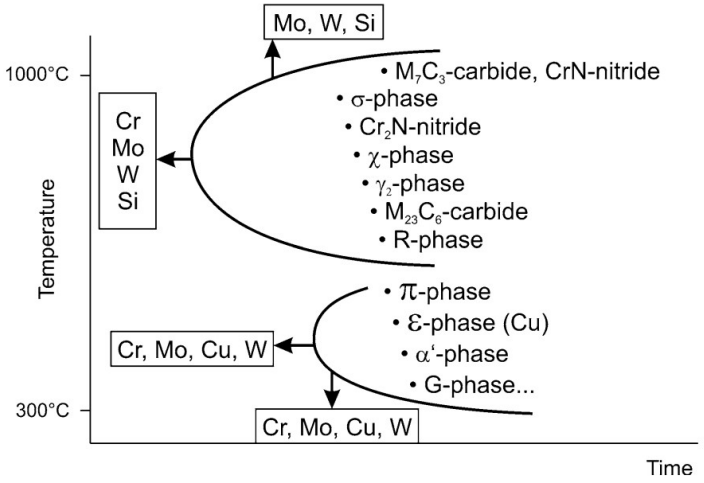

Figure 1.4: *Precipitation diagram of duplex stainless steels, after reference [6]*

more alloyed duplex grades, since the driving force for its precipitation increases with increasing contents of chromium and molybdenum. σ phase nucleates preferentially at δ/γ phase boundaries, δ/δ sub-grain boundaries and high energy δ/δ grain boundaries, leading to a depletion of Cr and Mo in the areas sorrounding the precipitate, inducing a local reduction in pitting corrosion resistance and a decrease in toughness. The σ nuclei can grow into different morphologies, from lamellar eutectoid $\sigma + \gamma_2$ with its typical coral shape, as in fig. 1.5(b), to coarse plates.

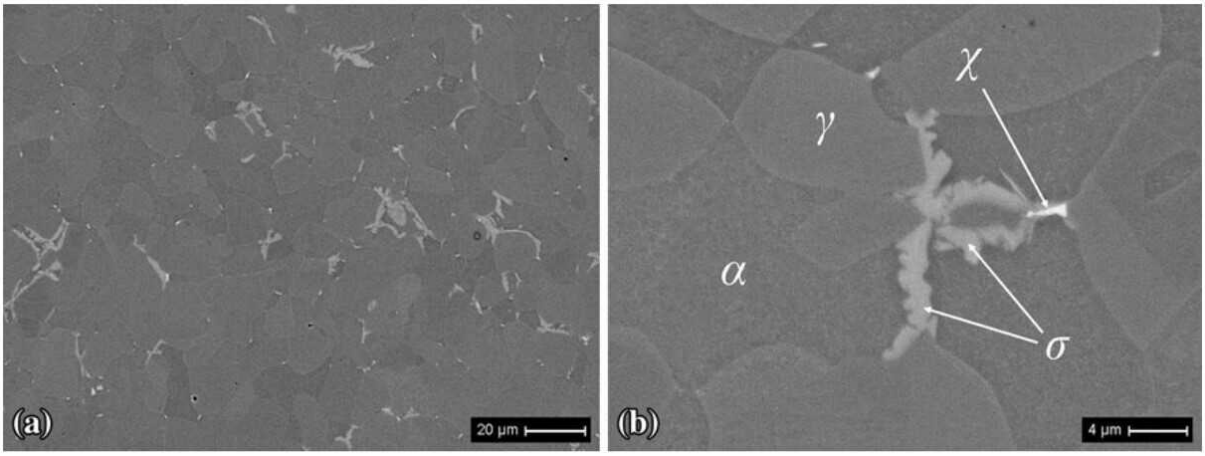

Figure 1.5: *Example of secondary phase precipitation in Zeron100 sample continuously cooled at 0.7 °C/s at lower (a) and higher (b) magnification (source:[7])*

- **Chi (χ) phase** precipitates in the same temperature range as σ, though in much smaller volume fractions. It often nucleates at δ/γ interface and grows into the ferrite, to which it is isomorphic. For this reason, χ phase nucleation is favoured with respect to σ, but it

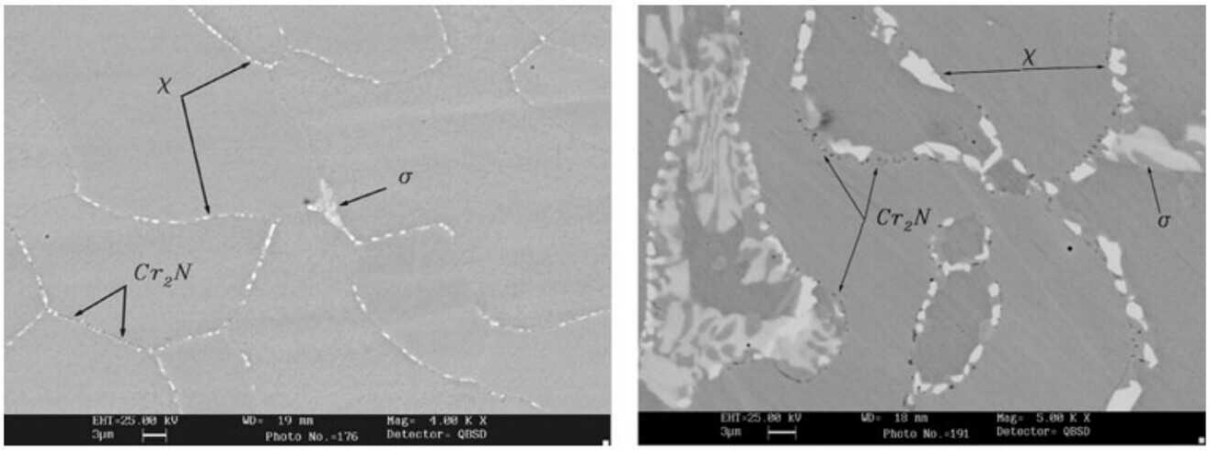

Figure 1.6: *SEM-BSE of 2507: left (900 °C, 5 min) and right (950 °C, 40 min) nitrides and chi-phase transforming to sigma-phase (source: [8])*

provides a suitable nucleation site for the latter. The two phases are therefore often simultaneously present in the microstructure of duplex alloys, making it difficult to analyse them separately. DSSs alloyed with tungsten have been shown to influence diffusion of Mo at phase boundaries, thus encouraging rapid precipitation of Mo-rich χ intermetallic with respect to the base material.

- **Nitrides Cr_2N and CrN** precipitation takes place at grain or phase boundaries when cooling is too slow in the range of 600-900 °C. Nitrogen solubility in ferrite is considerably lower with respect to austenite, especially when temperature begins to drop below 1000 °C: ferrite therefore becomes supersaturated in nitrogen, which is *trapped* in its lattice, leading to the precipitation of chromium nitrides. This behaviour is kindled by the higher solubility (of austenite) for interstitial elements, as well as by the greater number of tetrahedral sites. Nitrides of the CrN type precipitate when nitrogen solubility is exceeded and its diffusion in austenite is inhibited: their precipitation overcomes even cooling rates higher than 2500 °C/s [6]. Due to its similarity to the ferrite lattice, CrN nucleation has a lower activation energy compared to Cr_2N, which is more stable and usually precipitates rapidly after quenching from high temperature solution heat treatment (*quenched-in* nitrides). CrN nitrides are characterized by a primary cubic lattice and precipitate homogeneously in disk-shaped configuration throughout the ferrite matrix; on the other hand, Cr_2N nitrides have a hexagonal close-packed (HCP) crystal structure and can develop both at δ/γ phase boundaries and inside the ferritic grain. The addition of austenite-stabilizing elements can inhibit precipitation of nitrides in the ferrite, which is associated to a decrease in corrosion resistance and toughness, leading to brittle fracture behaviour of DSSs.

- **Alpha prime (α')** formation is caused by the immiscibility gap in the Fe-Cr system, where

ferrite undergoes the *spinodal decomposition*, which consists in a loss of ambient temperature toughness after prolonged exposure at a temperature of 475 °C. The so called *475 embrittlement* can be avoided by keeping to a minimum the residence time of the alloy at such temperatures. α' is more commonly found in Mo-rich duplex grades.

- **Secondary austenite (γ_2)** can be formed in various ways depending on the temperature range. Below 650 °C its formation takes place with a diffusionless transformation, similar to that of martensite; at 650-800 °C diffusion is faster and γ_2 can be found in the shape of Windmanstätten lamellar structures. In the 700-900 °C temperature range γ_2 forms through Ni absorption and expulsion of Cr and Mo, leading to the formation of a eutectoid of $\gamma_2 + \sigma$, thus increasing the susceptibility with respect to pitting corrosion.

- **Carbides $M_{23}C_7$ and M_7C_3** precipitation is a rare occurrence, since modern duplex stainless steels contain less than 0.02 %C. When carbon content is higher, precipitation mainly occurs at γ/δ boundaries, where Cr-rich ferrite intersects with carbon rich austenite, leading to the onset of intergranular corrosion due to the depletion of chromium at grain boundaries.

- **Cu-rich epsilon (ϵ) phase** precipitation takes place in Cu-rich duplex alloys, causing an extension of the low temperature hardening range of the metal.

1.1.5 Hot deformation behaviour of DSSs

The temperature range for hot working of duplex stainless steels is 1000–1300°C, where the austeno-ferritic structure is first established [9]. If hot forming were performed at lower temperatures, deformation would accumulate in the ferrite phase which, being less ductile compared to austenite, is prone to the onset of side cracks and fissures, which eventually lead to the failure of the component. These differences in the mechanical properties of austenite and ferrite can be observed in figure 1.7, where a completely ferritic AISI 430 grade exhibits an elongation % of 20 versus a decidedly higher 45 % belonging to an austenitic AISI 304. Moreover, significant quantities of σ phase can precipitate at lower hot-working temperatures, leading to a reduction in the mechanical properties of the final product. Thermo-mechanical processing induces significant microstructural changes in DSSs, not only in terms of embrittling phase precipitation but also throughout the evolution of softening mechanisms pertaining to the two comprising phases [10], [11]. The dominant deformation mechanism of ferrite differs from that of austenite in that it undergoes a dynamic recovery phenomenon (DRV), activated by its high stacking-fault energy (SFE), which promotes rearrangement of dislocations through climbing and/or cross-slipping. Due to its otherwise limited SFE, DRV in austenite is delayed and dynamic recrystallization (DRX) is instead favoured: once a certain critical strain is

Alloy	Standard	0·2% proof stress (min.), MN m^{-2}	Ultimate tensile strength, MN m^{-2}	Elongation (min.) A5, %	Impact toughness at RT, J	Fluctuating tension fatigue strength, MN m^{-2}
AISI 304	UNS S 30400	210	515–690	45	>300	120 ± 120
AISI 430	UNS S 43000	205	450	20	...	...
23Cr–4Ni (SAF 2304)	UNS S 32304	400	600–820	25	300	245 ± 245
22Cr–5Ni–3Mo (SAF 2205)	UNS S 31803	450	680–880	25	250	285 ± 285
25Cr–7Ni–4Mo (SAF 2507)	UNS S 32750	550	800–1000	25	230	300 ± 300

RT room temperature.

Figure 1.7: *Comparison of the mechanical properties values of austenitic, ferritic and solution annealed duplex stainless steels, after reference [9]*

exceeded, nucleation and growth of new grains is observed. However, some researchers found occurrence of continuous dynamic recrystallization in both ferrite and austenite microstructures for forging temperatures above 1050 °C [12], further confirming the complexity of such interactions. Thus the intrinsic nature of a duplex microstructure in which austenite and ferrite are characterized by different plastic behaviours, as well as different thermal expansion coefficients, leads to non-uniform deformation and stress repartition [13] that are reported to affect not only mechanical properties but also corrosion resistance [14].

As previously stated, in the upper part of the hot working regime, alloying elements are subjected to rapid diffusion and the elemental distribution is close to equilibrium; in hot working practice, it is advisable to reach at least the minimum soaking temperature in order to avoid the formation of scale, which typically occurs at 1150 °C and above, as well as to maintain dimensional stability of the piece [4]. Due to the distinct mechanical behaviour of the two constituting phases, their volume distribution and the intrinsic nature of the δ/γ interphase boundary, DSSs may undergo major problems during thermo-mechanical processing. Therefore, an appropriate selection of deformation temperature and strain rate can help improve their hot workability. A deformation temperature of 1100 °C (lower limit of the hot-working range) was proved to be the optimal one by Mondal et al. [15] in guaranteeing suitable corrosion performance of a SDSS (specifically, low passivation current) after industrially-analogous hot forging (see fig. 1.9).

While cast DSSs can be processed by different routes, one of the most established manufacturing techniques in the oil and gas industry is *open-die forging*, for the production of high strength and corrosion resistant tubing and intervention tools, for example plug systems for downhole oil well completion [16].

Open-die forging consists in the fabrication of near-net shape components on which plastic deformation is obtained by application of uniaxial compression loads. During hot deformation the volume of the billet remains constant, so a height reduction is associated to an increase in

Grade	UNS No.	EN No.	Hot-forming temperature range		Minimum soaking temperature	
			°C	°F	°C	°F
	S32101	1.4162	1100–900	2000–1650	950	1750
2304	S32304	1.4362	1150–950	2100–1740	980	1800
2205	S32205	1.4462	1230–950	2250–1740	1040	1900
2507	S32750	1.4410	1230–1025	2250–1875	1050	1920
	S32520	1.4507	1230–1000	2250–1830	1080	1975
	S32760	1.4501	1230–1000	2250–1830	1100	2010
304	S30400	1.4301	1205–925	2200–1700	1040	1900
316	S31600	1.4401	1205–925	2200–1700	1040	1900

Figure 1.8: *Hot working range for various duplex grades (source:[4])*

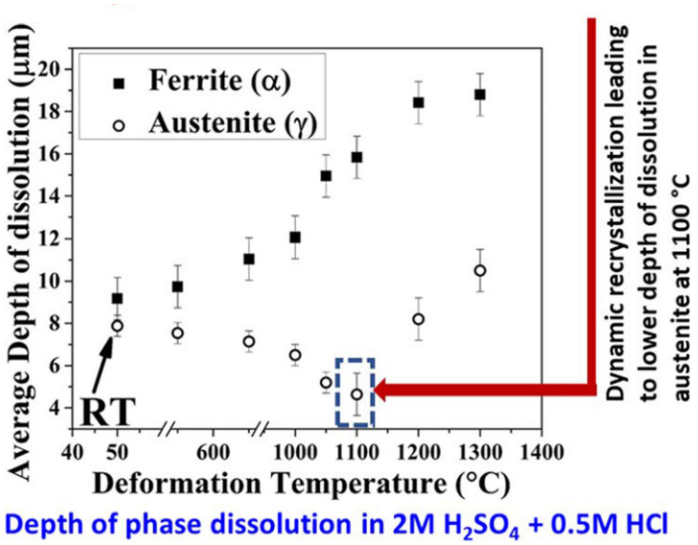

Figure 1.9: *Average depth of dissolution after corrosion testing for each phase versus deformation temperature for ferrite and austenite phases (source: [15])*

diameter [17]. Engineering (ϵ_e) and true (ϵ_t) deformation will be, respectively:

$$\epsilon_e = \frac{h_i - h_f}{h_i}$$

$$\epsilon_t = \ln \frac{h_i}{h_f},$$

h_i and h_f being the initial and final height of the billet. In hot forging, the onset of frictional

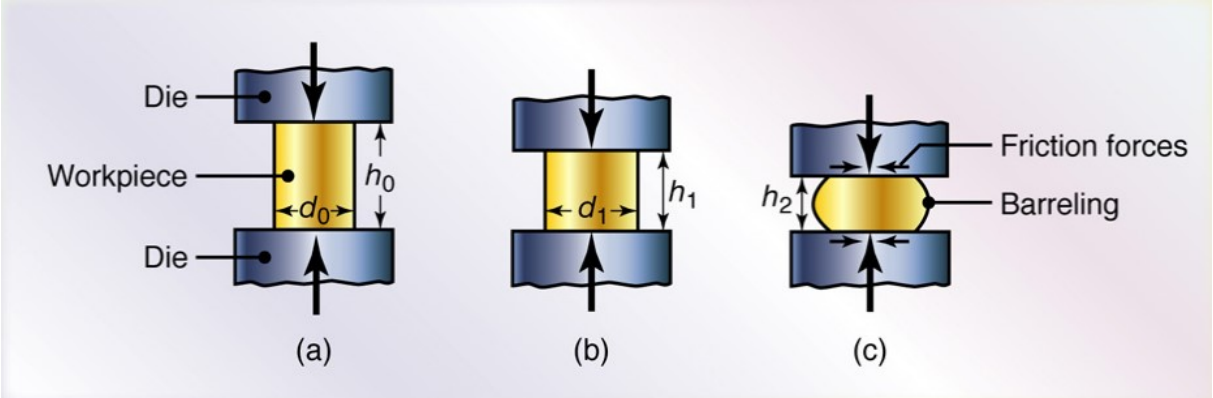

Figure 1.10: *Open-die forging in the ideal case (a, b) and with barreling effect (c), after reference [17]*

constraints between die and work-piece directly affect the plastic deformation of the latter (for example a cylindrical billet). The work-piece material in contact with the surfaces of the punch and bottom platen can infact undergo heterogeneous deformation, called *barreling* [18].

1.1.6 Continuous cooling regime

When slowly cooled from temperatures close to the solution annealing one (1000-1300 °C, depending on composition), duplex stainless steels undergo a loss in toughness and corrosion resistance due to the precipitation of secondary phases, the most dominant effect given by σ phase. Even small amounts of σ phase can reduce significantly the utilization range of the steel, so it is important not only to accurately evaluate the volume fraction of such intermetallic but also to select the most suitable cooling rate required for optimal processing of the material. At temperatures near the solvus, the nucleation of precipitates is slow and their growth is fast, while at lower temperatures the opposite is true, so a solution treatment should be performed at a sufficiently high temperature to redissolve any unwanted phases and cooling fast enough to avoid the intersection with the *nose* of the σ field of existence, which can be observed in the CCT diagram of fig. 1.11. Many studies have demonstrated that the amount of precipitated phases is strongly affected by the cooling rate, while it does not seem to be affected by the temperature of previous solution annealing. In particular, Calliari et alia [7] investigated the precipitation

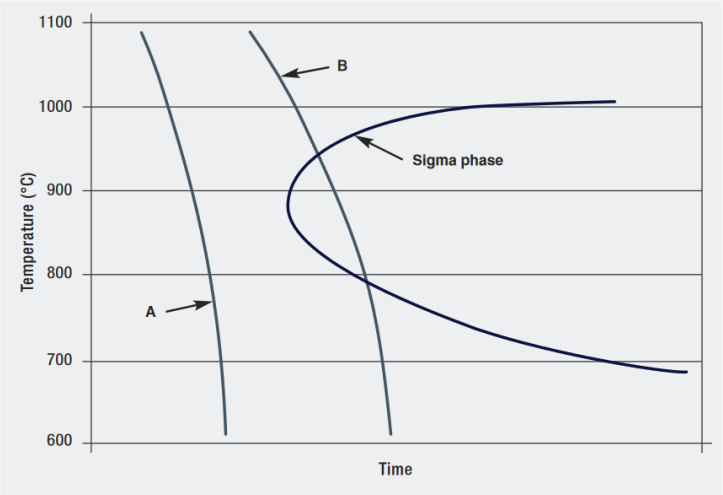

Figure 1.11: *Examples of continuous cooling from solution annealing temperature: at slow rates (B) σ-phase may be formed, while fast cooling (A) avoids it (source: [4])*

of secondary phases in a Zeron100 duplex steel after continuous cooling and found that cooling from a temperature of 1200 °C at a rate of 0.7 °C/s led to a total amount of precipitated inter-metallics around 1%; with a gradual decrease of the cooling rate down to 0.5 °C/s, simulating slow thermal processes, the highest amount of secondary phases detected was found to be about 25%.

1.2 Corrosion of Duplex Stainless Steels

The corrosion properties of stainless steels is determined by their ability to passivate and remain in the passive field during operation. In particular, the corrosion behaviour of stainless steels is comparable or even superior to that of austenitic stainless steels containing similar amounts of chromium and molybdenum. The significant presence of Cr is beneficial in oxidizing acidic environments, while Mo and Ni contribute to the material resistance in mildly reducing acids. Moreover, modern DSSs are also characterized by high nitrogen contents, which conveys exceptional stress corrosion cracking resistance compared to that of austenitic stainless steels. Together with their attractive mechanical properties, DSSs can therefore outperform other stainless steels in many applications, such as in heat exchangers operating with chloride-containing media.

1.2.1 Pitting corrosion

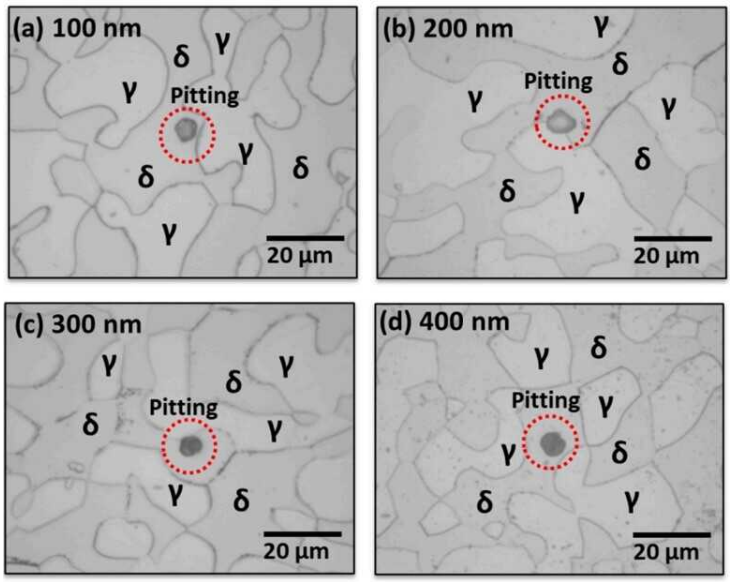

Figure 1.12: *Pitting morphologies of UNS S32760 DSS at different surface roughnesses, after reference [19]*

Due to their passive nature, DSSs are extremely resistant towards generalized corrosion, whereas depending on their chemical composition they might be threatened by localized corrosion phenomena. In particular, they can be sensitive to pitting, a deep penetrating attack that results in the formation of cavities with a diameter of less than a few millimiters, called *pits* (1.12). Initiation time of pitting is stochastic in nature, while propagation once started is catastrophic. In terms of electrochemical cell, the pit represents the anodic area, which is very small

compared to the cathodic zone, made of the external sorrounding area, so involved current densities and penetration rates tend to be very high. Pit formation is usually caused by abnormal conditions, either in terms of irregularities of the passive film or aggressiveness of the environment. Stainless steels tend to be particularly sensitive towards the presence of chloride ions, due to their small size, high diffusivity and strong anionic nature, which concur to their ability of breaking down the passive film. One of the pitting initation theories is based on the *adsorption* of halide ions through imperfections in the oxide layer, for example weak points where inclusions might be located. Cl^- adsorption causes a strong increase in the ionic conductivity and leads to the migration of metal cations into the solution, locally disrupting the passive film. The environment that is created inside the pit becomes increasingly more acidic, due to the hydrolisis of metal ions and related rise of pH. A quick estimation of DSS resistance towards pitting is provided by an empirical index termed *pitting resistance equivalent number* (PREN), which considers the weighted contributions of Cr, Mo, N and, in the alloys in which it is present, W:

$$PREN = \%Cr + 3.3 * (\%Mo + 0.5 * \%W) + k * \%N \tag{1.1}$$

where *k* is a number between 10 and 30, but 16 is the most frequently used value. PRE number thus shows the beneficial effects in improving pitting corrosion resistance of some alloying elements, like nitrogen, which is calculated with a comparatively high factor with respect to chromium. Indeed, highly alloyed duplex grades usually exhibit PRE values ranging between 40 and 45, much higher with respect to the 24-25 of 316L austenitic stainless steel. However, PREN is not sufficient for a precise determination of the pitting resistance of DSSs, since it is based only on composition and does not include any information on phase morphology nor microstructure. Figure 1.13 shows the relationship between PRE number and *critical pitting temperature* (CPT) of DSSs, which is a determining parameter in evaluating pitting corrosion. CPT is described as the temperature at which a current increase occurs, associated with the breakdown of the passive layer at a certain potential; it can be measured by using the modified ASTM-G150 test. For example, super duplex stainless steels, which are characterized by PRE values above 40, usually exhibit a critical pitting temperature of around 80 °C; on the other hand, a 316L austenitic stainless steel has a CPT only as high as 10 °C .

1.2.2 Crevice corrosion

Crevice is a form of localized corrosion which concerns active-passive metals and is caused by the presence of interstices on the surface of a metal, such as cracks or deposits, that establish a condition of differential aeration. During the initial stage of the process, oxygen is depleted from the screened area, by means of the usual mechanisms of passive film growth and oxygen

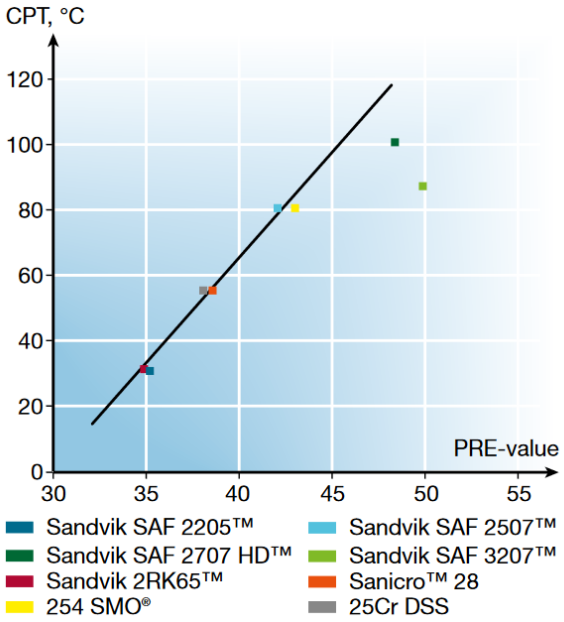

Figure 1.13: *PREn plotted against CPT of commercially available DSSs, showing a linear correlation (source: [1])*

reduction. When the oxygen inside the crevice is completely consumed, the underlying metal shifts to the active state and the onset of a stationary macrocell takes place. Chloride-containing environments favour the initiation of crevice corrosion, which is therefore a significant issue for DSS involved in marine applications, e.g. seawater pumping systems. The high content of alloying elements of UNS J93380 and UNS S32760 (Z100) steels guarantees them a high resistance towards crevice corrosion in chlorinated environments: fig. 1.14 shows the maximum depth of crevice penetration after 60 days of exposure at 16 °C with 1 mg/L chlorine, upon which only Z100 and 6% Mo resisted [20].

1.2.3 Stress corrosion cracking (SCC)

As already mentioned, duplex grades were originally developed to operate in those applications where standard stainless steels show poor performances. One of the main examples is the sensitivity of austenitic stainless steels in chloride-bearing environments, which suffer from stress corrosion cracking at temperatures above 60 °C. DSSs are infact much less prone to SCC, owing to a winning combination of alloying elements, such as nickel and nitrogen (see fig. 1.16), which greatly improve the corrosion resistance of austenite, the phase which tended to be preferentially attacked. However, under specific conditions, duplex stainless steels may be susceptible to SCC, for example when hydrogen-induced cracking is favoured, as in boiling 42% magnesium chloride test, drop evaporation when the metal temperature is high and exposure to pressurized aqueous chloride systems in which the temperature is higher than what is possible

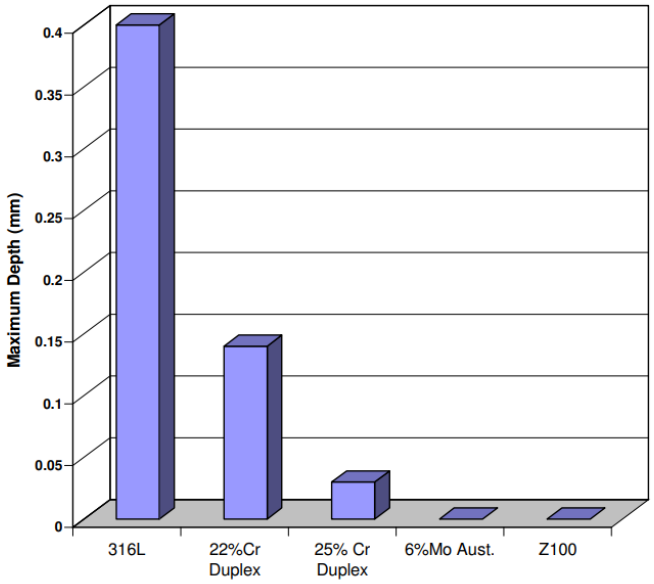

Figure 1.14: *Depth of crevice corrosion in seawater at 16°C with 1mg/L chlorine, after reference [20]*

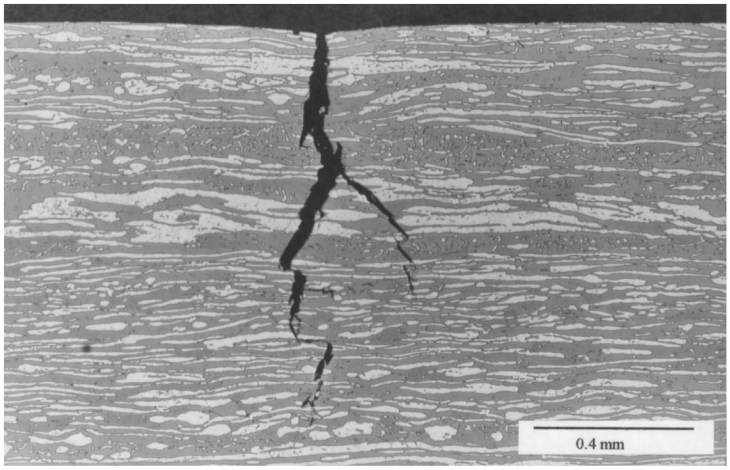

Figure 1.15: *SCC in the gauge length of a duplex stainless steel specimen strained to failure in NACE-01-77 solution at 20°C (source:[21])*

at ambient pressure. Despite their susceptibility to hydrogen cracking, duplex stainless steels can be employed in hydrogen-containing environments as long as the operating conditions are carefully evaluated and controlled. By increasing the ferrite volume fraction the SCC resistance can be enhanced: infact the yield strength of ferrite exceeds that of austenite, which translates into the blocking of transgranular cracks at ferritic grains.

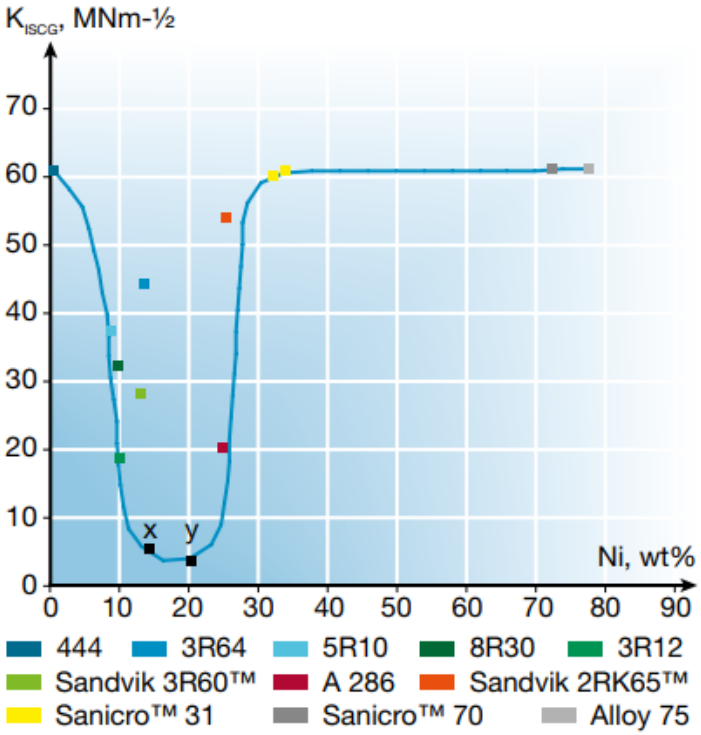

Figure 1.16: *Effect of nickel content on stress intensity factor KISCC (source: [1])*

1.2.4 Intergranular corrosion (IGC)

Sensitization is defined as the precipitation of chromium carbides at the grain grain boundaries of a stainless steel, causing a depletion of Cr in the near matrix (fig.1.17) which becomes susceptible to localized corrosion and stress corrosion cracking. Quoting the ISO 12732-2008 standard, *the extent to which these damage mechanisms develop and propagate will depend on the extent of depletion and the density of depleted zones*. The sensitization process therefore jeopardizes the passivity build-up of the stainless steel and typically occurs in austenitic grades characterized by high contents of carbon, in which the probability of carbide precipitation is significant. On the other hand, DSSs are practically immune to such phenomenon, thanks to their carefully selected alloying composition.

Nevertheless, the precipitation mechanism of detrimental σ phase shows some similarities to the

sensitization phenomenon, for instance the formation of a chromium-depleted region around the chromium-enriched σ intermetallic. Moreover, sensitization does take place in DSSs when they are pronlongedly exposed to the temperature range where chromium carbide precipitation is favoured, that is between 400 and 1050 °C. The extention of the chromium-impoverished areas due to carbide precipitation is defined as the *degree of sensitization* (DOS).

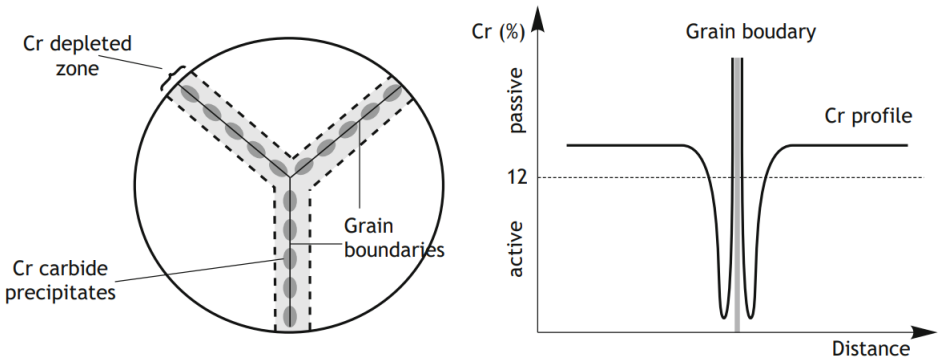

Figure 1.17: *Representation of Cr carbides precipitation and profile of %Cr at grain boundaries (source:[22])*

1.3 Testing

1.3.1 Double Loop Electrochemical Potentiokinetic Reactivation (DL-EPR)

DL-EPR is a simple non-destructive electrochemical test developed to determine the degree of sensitazion in stainless steels and nickel-based alloys, as described in ISO 12732-2008 standard. Originally conceived to test intergranular corrosion in 304 and 304L austenitic stainless steels, the EPR technique can also be successfully used to evaluate other stainless steel grades, by modifying test conditions and evaluation criteria. In particular, it can be a crucial tool in guaranteeing integrity and performance of DSSs through the investigation of σ phase presence [23]–[25]. EPR allows for a quantitative assessment of the effect of sensitization on the material, since it provides a valid correlation between the electrochemical parameters obtained during testing and the actual extent of sensitized areas [26].

EPR involves the plotting of an anodic polarization curve, which graphically represents the behaviour of the current in response to potential changes applied in a corrosion system. The EPR curve can be either unidirectional or bidirectional: the single loop EPR (SL-EPR) test is characterized by a reverse curve, obtained by scanning the potential from positive to negative; this first variant has the disadvantage of being particulary sensitive towards surface finish. With a double

loop EPR test the steel is instead polarized by applying a constant forward scan (in the anodic direction, from the open circuit potential to the passive range), followed by a reverse scan [27]. This second methodology is the most favourably employed, since the sample immersed in an acid solution reaches the active state in simulated freely corroding conditions, thus dissolving any initial surface feature.

During the anodic polarization, a current maximum is observed, known as the *activation current* I_a; as the reverse scan (cathodic polarization) takes place, the passive film formed during the forward scan is expected to gradually dissolve, first *re-activating* the weaker areas deficient in chromium, where the passive film is locally less protective and more easily reduced. Thus an-

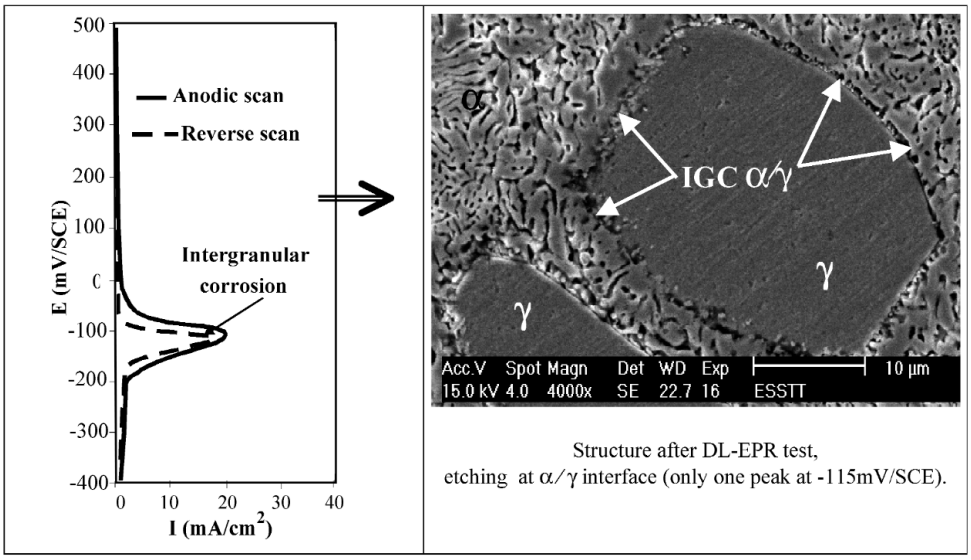

Figure 1.18: *Effect of DL-EPR on aged UNS S31250 DSS with 33 pct H2SO4 + 0.3 pct HCl at 20 °C and a scan rate of 2.5 mV/s, after reference [23]*

other current peak appears, termed *reactivation current* I_r (as is shown in fig. 1.19). As standard ISO 12732-2008 states, the reason for such gradual rise in current lies in the spread of the extent of depletion and the associated variations in passive film properties, which cause a build-up of the activity of all the sites. The greater the value of the reactivation current, the more severe the degree of chromium depletion in the steel; moreover, I_r is approximately proportional to the sensitized area. The degree of sensitization is measured as the ratio of the two current peak values:

$$DOS = \frac{I_r}{I_a}\ \% \tag{1.2}$$

Such a parameter can therefore be employed to differentiate between highly and not sensitized microstructures as well as to characterize in terms of sensitization even moderately degraded samples. A DOS lower than 1% is associated to a near-to-zero sensitazion, from 1 to 5% sensitazion is moderate, while if higher than 5% it can cause major issues to the material.

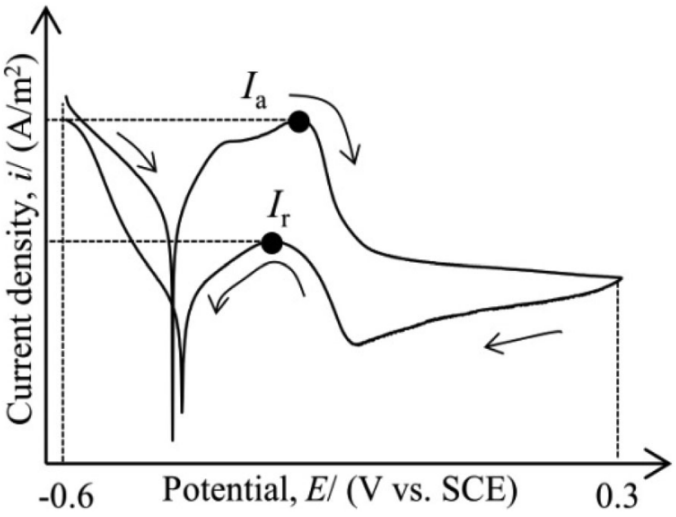

Figure 1.19: *Schematic representation of a DL-EPR curve (source:[28])*

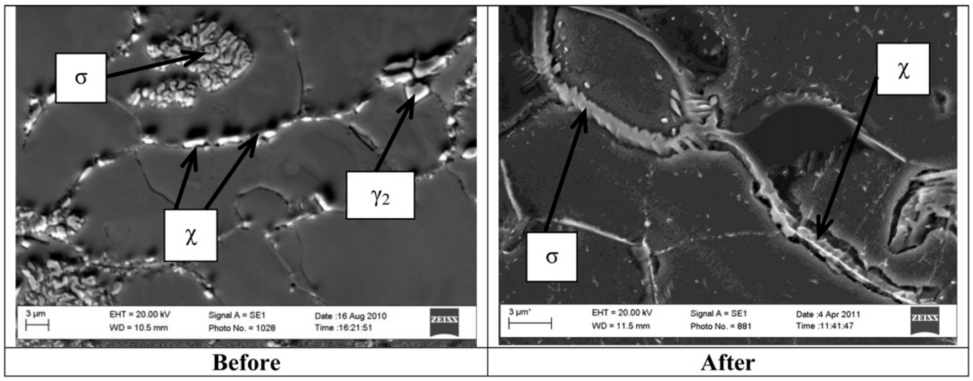

Figure 1.20: *Microstructural aspects of aged UNS S32750 DSS before and after DL-EPR, obtained by SEM (source:[29])*

1.3.2 Anodic polarization

Potentiodynamic polarization tests are carried out to electrochemically determine the pitting potential of the material, when breakdown of the passive film takes place and localized corrosion is initiated. The more noble this potential, the less susceptible is the alloy to onset of pitting. Anodic polarization is performed with a potential scan in the anodic direction starting from the corrosion potential (E_{corr}) and proceeding to +1.6 V_{SCE} (active to noble), while the current is recorded continuously, as shown in the plots of fig. 1.21(b). Anodic polarization plots are an important tool to identify the passive behaviour of the steel when in contact with a specific solution. The parameters which can be obtained from anodic polarization curves are the following [see fig. 1.21(a)]:

- *critical passivation current* (i_{cp}), which is related to the transition from active to passive state and decreases as the tendency towards passivation increases
- *passivity current density* (i_{pit}), corresponding to the formation of the passive layer
- *primary passivation potential* (E_{pp})
- *passivity potential* (E_p), which is the lower limit of the passivity range, upon which current usually does not experience significant variations
- *pitting potential* (E_p) or *transpassivity potential*, which determines the local breakdown of the passive film and the shift towards the onset of noble anodic processes (e.g. oxygen evolution)

For example, UNS J93380 duplex grade in annealed condition exhibits a pitting potential between 900 and 1000 mV_{SCE} in simulated seawater [31].

1.3.3 Critical pitting temperature (CPT)

Critical pitting temperature (CPT) is defined by ASTM G150 and G48 International Standards as the minimum potential-independent temperature at which pitting evolution occurs [32]. The CPT potentiostatic experiment consists in applying a constant potential to the specimen while the cell temperature is raised and the current is recorded [as in fig.1.22)(b)]. When the detected current density equals or exceeds 100 $\mu m/cm^2$ for more than 60 s it means that the sample has undergone pitting attack. In particular, formation of pits is characterized by an early metastable growth, in which the current experiences sudden peaks but for very short times, and a consecutive stable growth, which coincides with the drop of breakdown potential and reaching of CPT. Highly alloyed duplex stainless steels can exhibit immunity towards pitting up to the boiling

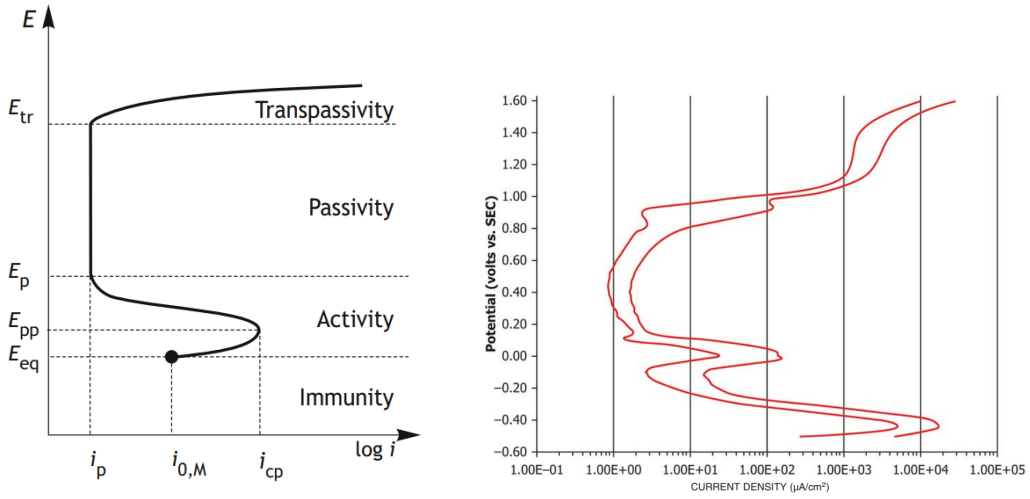

(a) (b)

Figure 1.21: *a) Anodic characteristic of an active-passive metal, from [22] and b) typical potentiodynamic anodic polarization plot from ASTM G5-14 standard [30]*

point of the solution, which can be constituted of different concentrations of either NaCl or ferric chloride. CPT values reported for super duplex steels are between 80 and 90 °C [33], as displayed in the data collected in fig.1.22(a); for instance, Pezzato et al. found that CPT of a 2507 duplex in unsolutionized wrought condition was of 88 °C [34]. CPT is considered

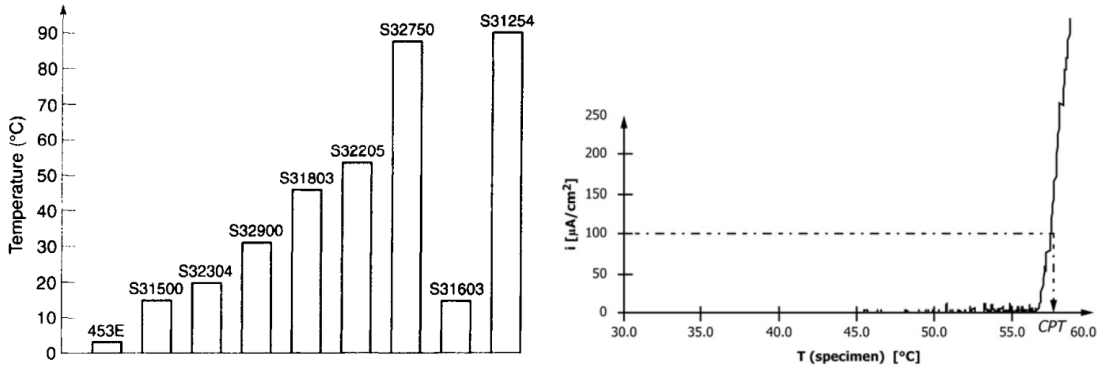

Figure 1.22: *a) CPT determined by a potentiodynamic technique for duplex unwelded sheets in 1M NaCl, after reference [2]; b) Determination of CPT, after ASTM G150-18 standard [35]*

a fundamental reference standard for screening materials in engineering applications, as it can accurately reflect the sensitivity of materials to temperature.

1.4 Reasons and objectives of the thesis

The present work concerns the phenomenon of secondary phase precipitation in UNS J93380 duplex stainless steel, namely a modified 2507 (see 1.1.1) produced by casting and especially designed to operate in chloride-containing environments, such as offshore platforms. The chemical composition of such alloy includes additions of 0.5-1 wt.% copper and tungsten, together with a relatively high nitrogen content of 0.2-0.3 wt%, which together concur to convey a high corrosion resistance to the steel. Active research is currently devoted to maximize the efficiency of thermo-mechanical processing of SDSSs, in pursuit of optimized microstructure and performance of the component. Current industrial practice prescribes full solution annealing after hot processing, followed by water quench to obtain a complete restoration of mechanical and corrosion properties. On account of the technical importance of hot forging of DSSs, for example in the manufacturing of flanges, elbows and discs for high-pressure pipework in petrolchemical industries, documentation on more energetically sustainable, cost-effective and faster hot forging schedules is lacking. As a consequence, microstructure evolution and deformation behaviour of DSS when hot forged directly after solution annealing are comparatively underinvestigated.
This thesis focuses on the intermetallic precipitation behaviour in UNS J93380 SDSS when hot forging is performed at 1100 °C, which is the suggested minimum solution annealing temperature required for this material (see fig. 1.8). In particular, part of the work will be committed to understanding how hot forging affects the thermodynamics of precipitation of σ, χ and especially Cr nitrides, the formation kinetics of which is still unclear.
At the basis of the hot forging simulation is a solution heat treatment, which allows to obtain the best mechanical and chemical characteristics of DSSs, especially considering that at high temperatures all the secondary phases originated from the as-cast microstructure are dissolved. After a selected soaking time during which such microstructure homogenization takes place, deformation can be imposed from a completely solubilized condition. Water quenching is performed in order to keep large quantities of solute atoms in solid solution, thus avoiding re-precipitation. Hot forging of the samples was simulated by application of a true deformation degree of 50% at a given strain rate, chosen amongst the range presented in the article by Cabrera et al. [36]. Before quenching, the specimens are continuously cooled down to 500 °C at various cooling rates, after those proposed in the work of Calliari et al. [7], [8].
Corrosion resistance and electrochemical tests serve as a reliable approach to determine the effects of precipitated secondary phases on DSSs. Assessment of the corrosion properties of the material after hot forging was therefore implemented by electrochemical testing: in particular, double loop EPR technique was chosen as the leading technique of this project, with the aim of proving its simplicity and clear result availability in detecting the presence of intermetallic

precipitates with respect to other conventional corrosion methods. Its validity was appraised throughout complementary specific testing.

Chapter 2

Materials and methods

2.1 UNS J93380 duplex stainless steel

This study concerns a UNS J93380 DSS (AISI Z100, ASTM A890/6A), whose chemical composition is reported in table 2.1. Its equivalent in wrought condition is UNS S32760, more commonly found in the market but with the same content of alloying elements. These alloys were however originally produced as castings, employed for the production of valves and pumps for handling sulphuric acid. They stand out owing to the addition of copper and tungsten, which allow them to withstand more aggressive environments with respect to other duplex grades. The

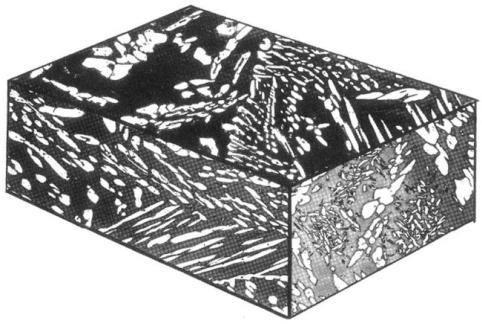

Figure 2.1: *Typical microstructure of DSS in cast form, source:[37]*

presence of copper in modified 2507 super duplex has been shown to be beneficial as an active alloying element in reducing acids [2], outperforming the pitting corrosion resistance even of some nickel-based alloys, like N08020 (see fig. 2.3). Indeed, Cu has been proved to increase the activity of chromium in hyper duplex stainless steels and effectively suppress the σ phase formation. However when added in contents higher than 2.5%, Cu can reduce the hot workability of the steel. Another important contribution in terms of corrosion of UNS J93380 is given

UNS	Element, wt% C	S	P	Si	Mn	Ni	Cr	Mo	Cu	N	Other
Standard 22% Cr											
J92205 (2205)	0.03	0.020	0.04	1.00	1.50	4.5–6.5	21.0–23.5	2.5–3.5	1.00	0.10–0.30	–
J93183 (KCR-D183)	0.03	0.03	0.040	2.0	2.0	4.0–6.0	20.0–23.0	2.0–4.0	1.0	0.08–0.25	0.5–1.5 Co
High alloy											
J93345 (Escoloy)	0.08	0.025	0.04	–	1.00	8.0–11.0	20.0–27.0	3.0–4.5	–	0.10–0.30	–
J93370 (CD-4MCu)	0.04	0.04	0.04	1.00	1.00	4.75–6.00	24.5–26.5	1.75–2.25	2.75–3.25	–	–
J93371 (3A)	0.06	0.040	0.040	1.00	1.00	4.00–6.00	24.0–27.0	1.75–2.50	2.75–3.25	0.15–0.25	–
J93372 (CD-4MCuN)	0.04	0.04	0.04	1.0	1.0	4.7–6.0	24.5–26.5	1.7–2.3	2.7–3.3	0.10–0.25	–
J93550 (KCR-D283)	0.03	0.03	0.040	2.0	2.0	–	23.0–26.0	5.0–8.0	1.0	0.08–0.25	0.5–1.5 Co
Superduplex											
J93380 (Zeron 100)	0.03	0.025	0.030	1.0	1.0	6.5–8.5	24.0–26.0	3.0–4.0	0.5–1.0	0.2–0.3	0.5–1.0W
J93404 (Alloy 958)	0.03	–	–	1.00	1.50	6.0–8.0	24.0–26.0	4.0–5.0	–	0.10–0.30	–

Figure 2.2: *Common cast duplex grades listed in the Unified Numbering System (source: [2])*

by the tungsten content, which has a similar effect to that of Mo in that it enhances stabilization of the passive film. It also reduces the probability of crevice corrosion in heated chloride solutions and was proved to have a retarding effect on σ phase precipitation [38]. UNS J93380 also exhibits a significant amount of nitrogen compared to other duplex grades (see fig. 2.2 for reference). Addition of nitrogen meets multiple purposes, by increasing pitting corrosion resistance, austenite to ferrite ratio and strength. It has a comparable effect to Cr and Mo, since it shifts the pitting potential towards the more noble direction, thus extending the passive potential range. Moreover, nitrogen was found to have a stabilizing effect of duplex grades against precipitation of intermetallic phases, by reducing Cr-partitioning. Additionally, due to its broadening effect on the austenite field, it leads to a reduction in the distance between austenite islands, thus controvertially inhibiting precipitation of nitrides. The concurring effect of these alloying elements results in a PRE number (refer to eq. 1.1) for this duplex grade of 41.8 (see fig. 2.1), making UNS J93380 super duplex the most suitable material in aggressive hydrochloric acid applications.

$$PREN = 25.5 + 3.3 * (3.4 + 0.5 * 0.77) + 16 * 0.24 = 41.8 \tag{2.1}$$

Elements	C	Mn	Si	P	S	Cr	Ni	Mo	Cu	N	W
Weight %	0.03	1.0	1.0	0.03	0.025	24.0-26.0	6.5-8.5	3.0-4.0	0.5-1.0	0.2-0.3	0.5-1.0

Table 2.1: *Chemical composition of the super duplex UNS J93380 in weight %*

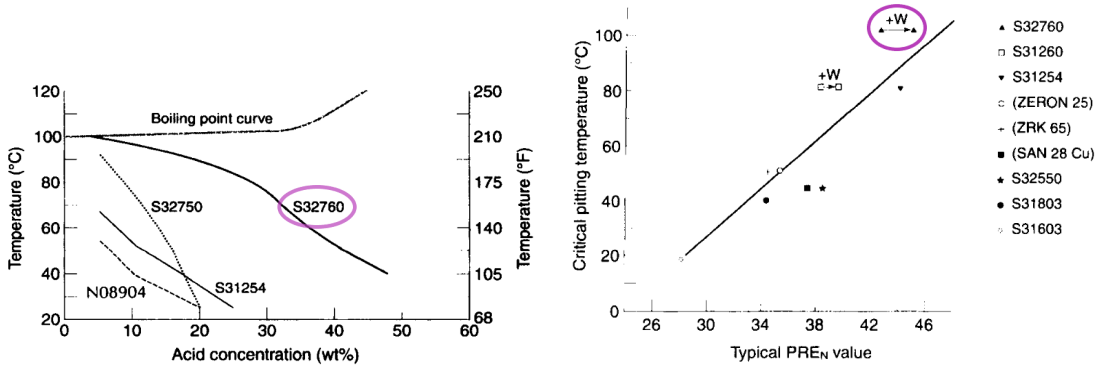

(a) (b)

Figure 2.3: *a) 0.1 mm/yr iso-corrosion curves in sulphuric acid plus 2000 ppm chloride; b) CPT data for wrought stainless steels in sea water plotted against PREN (source: [2])*

2.2 Experimental set-up

2.2.1 Processing

sample	n°	T_{sol} °C	heating rate °C/s	cooling rate °C/s	true deformation %	strain rate s^{-1}	soaking time s	T_{quench} °C
AR	1	-	-	-	0	-	-	-
SQ	2	1100	10	≫10	0	-	300	500
S10	9	1100	10	10	0	-	300	500
S1	3	1100	10	1	0	-	300	500
S05	4	1100	10	0.5	0	-	300	500
S025	12	1100	10	0.25	0	-	300	500
Sstep	14	1100	10	0.35	0	-	300	1000
FQ	5	1100	10	≫10	50	0.005	300	500
F10	10	1100	10	10	50	0.005	300	500
F1	7	1100	10	1	50	0.005	300	500
F05	8	1100	10	0.5	50	0.005	300	500
F025	16	1100	10	0.25	50	0.005	300	500
Fstep	15	1100	10	0.35	50	0.005	300	1000

Table 2.2: *Classification of the samples based on thermo-mechanical processing parameters*

The starting material (noted as as-received or AR) was delivered in cylindrical specimens of 12 mm diameter and 14 mm length, already in solubilized condition. Two types of experi-

ments were performed: one set of samples was subjected to controlled uniaxial compression in a computer-controlled dynamic forging simulator (Gleeble™3800) at a deformation temperature of 1100 °C. To reduce friction and avoid barreling of the specimens, a thin graphite foil was pasted on the edges of each sample before wedging between the punches in the hot compression workstation. Heating to processing temperature was carried out at 10 °C/s and a soaking time of 300 s was selected. Open-die forging tests were performed to a true deformation ϵ_t of 50%, with an applied strain rate of 0.005 s^{-1}, followed by continuous cooling at four different cooling rates down to 500 °C, at which point the sample was subjected to water quenching. The selected cooling rates were 10, 1, 0.5 and 0.25 °C/s. As a reference, one of the samples was water-quenched directly from 1100 °C. Additionally, one specimen was continuously cooled from 1100 °C to 1000 °C and then quenched, in order to verify if any modification might take place in the precipitation of nitrides. Such specimen will be referred to as *step-cooled* sample, to underline that it was thermally treated with an intermediate cooling step. The second set of samples was subjected to the same thermal treatment but without imposing any deformation (see fig. 2.5). Classification of the samples and their relative processing parameters are listed in table 2.2. Enumeration of the specimens is kept as it was first assigned during the experimental campaign, but an alternative nomenclature will be employed for better clarity: S stands for *solution* annealed, Q for *quenched*, F for *forged*, step for *step-cooled*. The letters referred to the thermo-mechanical processing of the samples will be followed by the numbers corresponding to the cooling rate (e.g. 10 for 10 °C/s, 025 for 0.25 °C/s et c.). In the text, ND and DEF will stand for *non-deformed* and *deformed*.

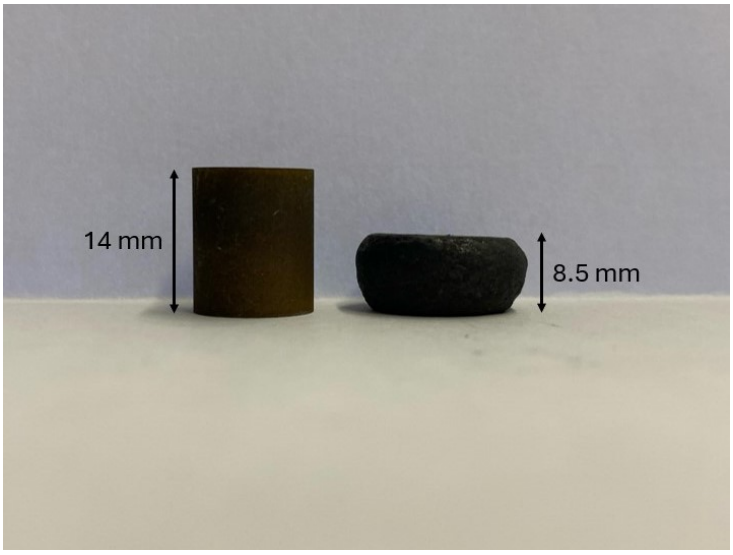

Figure 2.4: *Picture of AR (left) and post-compression (right) specimens*

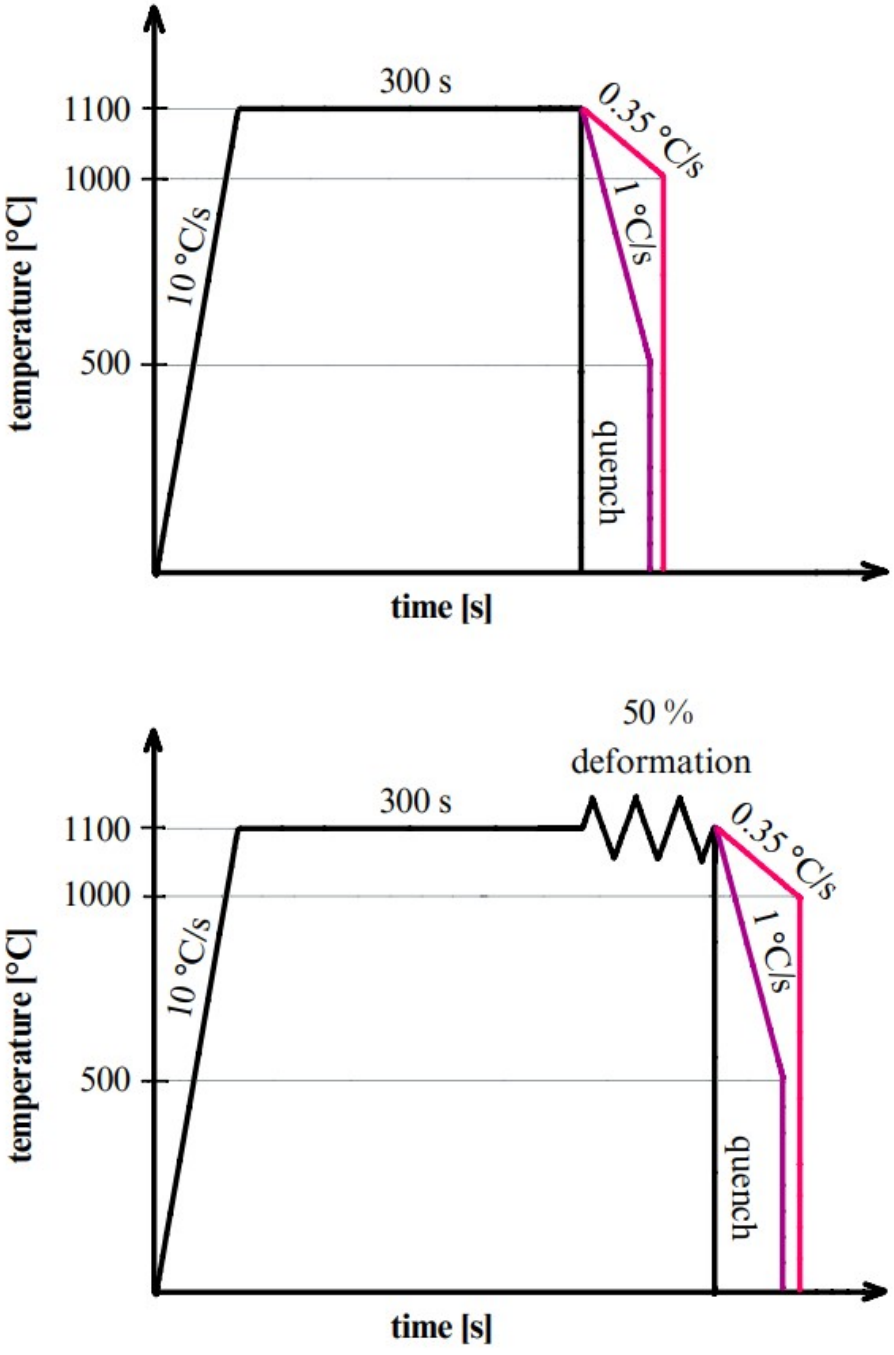

Figure 2.5: *Schematic representation of the two experiments, without and with deformation*

2.2.2 Microstructural, crystallographic and hardness characterization

The post-processing specimens were cut from the transversal short cross section taken from the middle length of the as-received products, where welding of the thermocouple was performed before thermal processing. This was done in order to avoid any effect of differential heating on corrosion performance. For each sample two sections were obtained, one for electrochemical testing and one for microstructure analysis. For cutting the samples, a ATM Brilliant 210 precision abrasive cut-off machine was used. The specimens intended for microstructural characterization were then mounted on a resin support for better handling. All the specimens were polished up to mirror finish following the standard method for metallographic preparation: grinding with 320, 500, 800, 1200 paper grits followed by polishing with diamond paste of 6, 3 and finally 1 μm particle size. The samples were then electrolytically etched with a 20% NaOH solution at 2.5 V for 5-10 s, as per ASTM A923. This type of etching guaranteed suitable contrast between austenite (white) and ferrite (dark). Phase quantification of all the post-processing samples was carried out with ImageJ software, as shown in picture 2.6, which allows to analyse the mictrostructure on a pixel basis, using a manual set threshold. It provides information on the overall phase distribution but its success is based on the quality of etching [39]. Images of un-etched samples were captured with Scanning Electron Microscope (SEM), both in back-scattered and secondary electrons mode, for measuring the volume fraction of secondary phases. Electro-polishing with A2 Struers solution was also performed for 20 s at

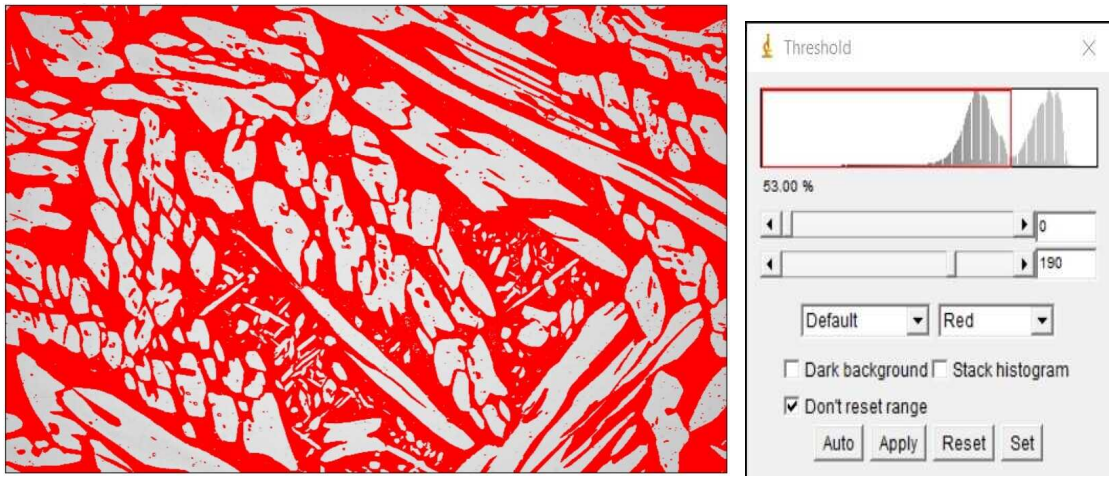

Figure 2.6: *Example of image analysis with ImageJ software*

21 V in order to obtain specimen surfaces without grinding-induced mechanical deformation, therefore achieving grain-contrast SEM-BSE images. Finally, optical and SEM images were taken after DL-EPR and CPT testing were performed on the samples.

Crystallographic investigation was carried out by SEM-EBSD, operated at 5 nA current and 25 kV beam energy; post-processing was done with AZtecCrystal software for nano-analysis from Oxford Instruments. Scans of 600 μm × 600 μm were performed with a step of 0.3 μm.
For this analysis, specimens were mechanically polished up to 1 μm and subsequently electro-polished with A2 Struers solution at 21 V for 30 s.

Finally, Vickers hardness measurements were performed to evaluate the material's resistance against plastic deformation, employing an Affri 250 MRS hardness tester with a diamond indenter applying a 10 kg load. Five measurements were taken for each specimen.

2.2.3 Electrochemical characterization

Electrochemical characterization of the samples was carried out with anodic polarization, DL-EPR and CPT employing a Gamry Interface 1010E potentiostat; as per ASTM G5 standard procedure, the tests were performed in a conventional three-electrode cell using a platinum counter electrode, specimen as the working electrode and a saturated calomel electrode (SCE) as the reference electrode (as depicted in fig.2.7).
Before testing, the corrosion samples were cleaned ultrasonically in denatured ethyl alcohol for 120 seconds and dried with compressed air. For the anodic polarization and critical pitting temperature tests, an adhesive tape was applied on the specimen surface in order to expose a limited surface area of 0.13 cm^2. For all the other tests the considered surface area was the one exposed by the sample holder, of 0.785 cm^2. Special care was taken to prepare samples in order to avoid crevice corrosion.
Follows an account of the performed electrochemical tests:

- The sensitization behaviour of all the specimens was studied with DL-EPR tests, employing a solution of 33% sulphuric acid (11.8 ml in 50 ml of aqueous solution) and 2.5% hydrochloric acid (3.5 ml in 50 ml solution), kept at 25 °C by using a resistive heating platform. At the beginning of the experiment, current conditioning at -0.6 V_{SCE} for 180 s was imposed to remove any existing oxide layer and cathodically polarize the sample. Consequently, open circuit potential (OCP) stabilization for 600 s was performed. Since the scan rate is sensitive to the specific alloy and should give a clear distinction between the activation and reactivation process, preliminary tests were undertaken to establish the optimum rate of 1.68 mV/s. The selected potential range was of ± 0.03 V_{SCE}. The expected OCP should be between -350 mV and -450 mV vs SCE. Free Corrosion potential should be around +200 mV_{SCE} to +600 mV_{SCE}. For each specimen, two DL-EPR tests

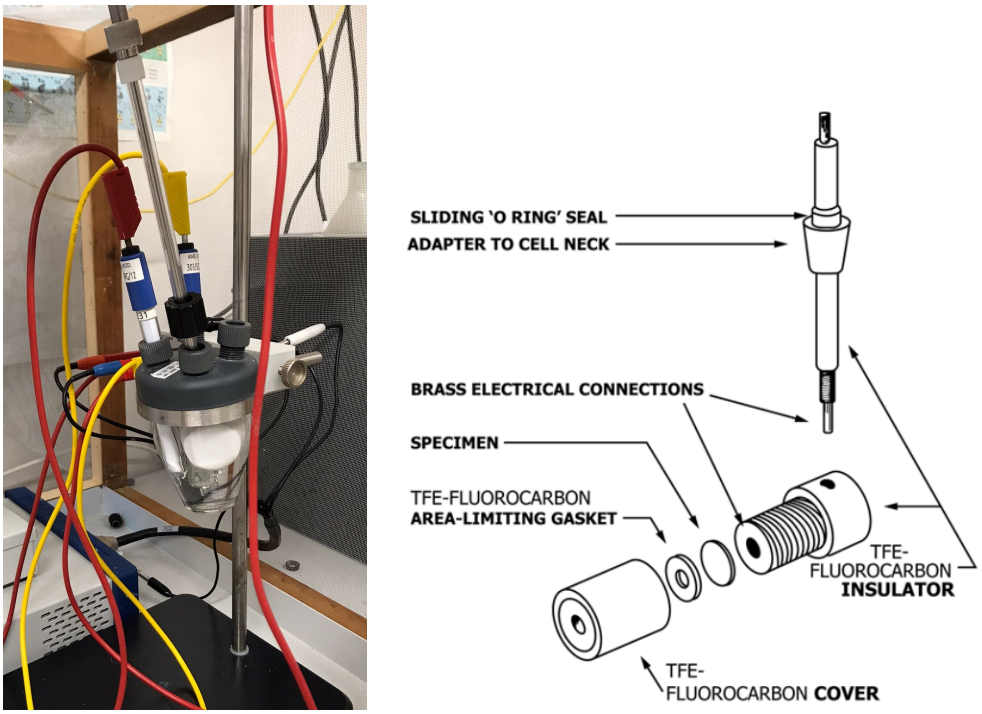

(a) (b)

Figure 2.7: *Three-electrode cell (a) and schematic diagram of specimen holder, after ASTM G61-86 standard [40] (b)*

were performed for repeatibility and the parameter I_r/I_a was obtained, as suggested by ISO 12732 standard.

- Anodic polarization tests were carried out as per ASTM G5-14 at room temperature in a 3.5% NaCl solution, simulating a marine environment. The applied potential scan rate was of 0.3 mV/s. Before the test, OCP stabilization was imposed for 2700 s.

- Critical pitting temperature of a selected set of samples was determined following the ASTM G150 standard. The saturated calomel electrode was inserted into a Lugging capillary filled with the operating solution at 25 °C, in order to keep it at constant temperature for the duration of the whole experiment. The electrodes and the capillary were immersed in a 1 mol/L NaCl solution, which was heated from a starting temperature of 25 °C (deviating from the 0 °C suggested by the standard) at a rate of 1°C/min. A thermostatic bath was used for temperature control. The temperature of the solution was registered every 300 seconds with a mercury termomether. A preliminary conditioning of the current was applied for surface cleaning for 60 s at a selected voltage of -0.6 V_{SCE}, after which the OCP was recorded for 600 s for stabilization. The experiment was carried out at a constant voltage of +0.7 V_{SCE}.

Chapter 3

Experimental results

In this chapter the data collected from the experiments will be presented, starting from a detailed analysis of the microstructure images obtained with SEM, optical microscope and EBSD, an evaluation of hardness macro-indentations and concluding with the results regarding corrosion properties.

3.1 Microstructural analysis

3.1.1 Primary phase quantification

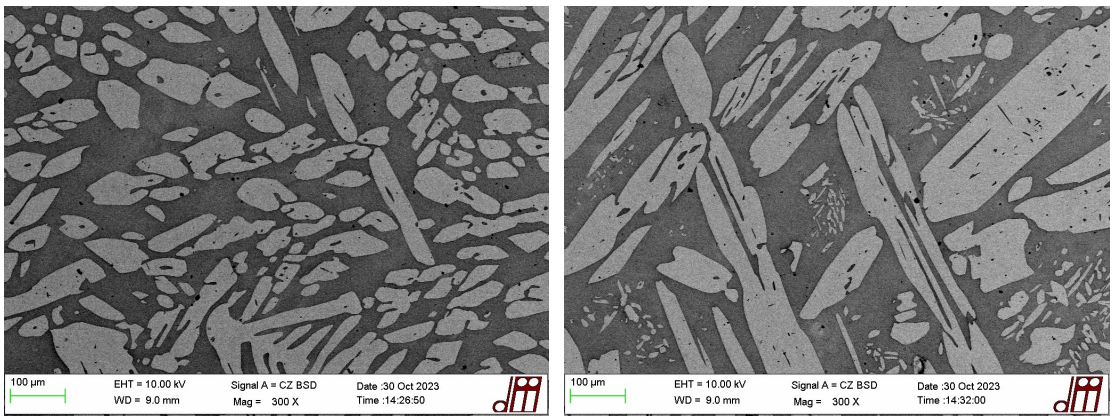

(a) (b)

Figure 3.1: *BSE micrographs showing the microstructure of AR sample obtained after electrolytic etching with 20% NaOH at 300x magnification*

Fig.3.1(b) shows the microstructure of the as-received sample: wide white-coloured primary austenite islands in a dark ferritic matrix can be observed, together with evenly distributed

clusters of secondary austenite γ_2. The latter is a solidification structure frequently encountered after high temperature cooling, developing with the shape of elongated speckles subsequent to a Windmanstätten precipitation mechanism [41], [42]. In order to verify if any significant changes in the δ/γ ratio occurred after thermal processing and hot forging, phase quantification by means of image analysis (IA) with ImageJ software was carried out. OM images at 100x magnification of samples post-electrolytic etching with 20% NaOH were used (about 6 per sample), in the attempt of maximizing contrast between the two phases and thus allow more precise measurements, for which the average and standard deviation are presented displayed in table 3.1.

The obtained values do not show significant changes in the austenite/ferrite ratio, besides a maximum ferrite content found in samples SQ (simply quenched) and Sstep (step-cooled). The minimum δ content is found in sample F025, in which a significant presence of secondary phases was observed.

true deformation %	**sample**	**cooling rate** °C/s	**ferrite volume fraction** %	±
0	AR	-	54	1
	SQ	$\gg$10	59	3
	S10	10	52	6
	S1	1	57	2
	S05	0.5	56	3
	S025	0.25	54	1
	Sstep	0.35 step	59	2
50	FQ	$\gg$10	56	2
	F10	10	56	3
	F1	1	57	2
	F05	0.5	55	4
	F025	0.25	48	4
	Fstep	0.35 step	57	2

Table 3.1: *Ferrite volume fraction calculated by IA*

3.1.2 Secondary phase quantification

Optical microscope examination

Figure 3.2 shows optical micrographs obtained for specimens etched in 20% NaOH. Overall a coarser microstructure with fragmented austenite boundaries is observed in post-deformation samples, along with an increase in secondary phase content (darker-coloured) with decreasing cooling rate. Even at low magnification it is possible to observe that while at 0.25 °C/s ND intermetallics precipitate at γ/δ grain boundaries, in the same sample with deformation secondary

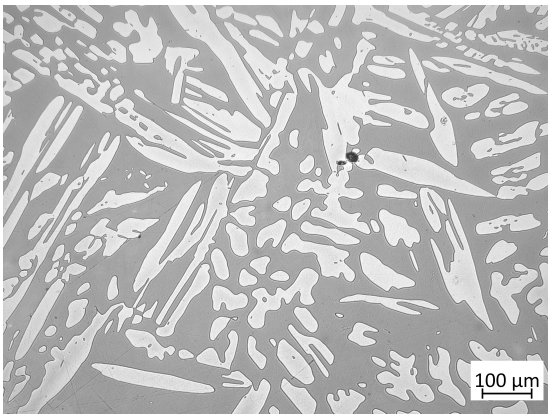

(a) SQ

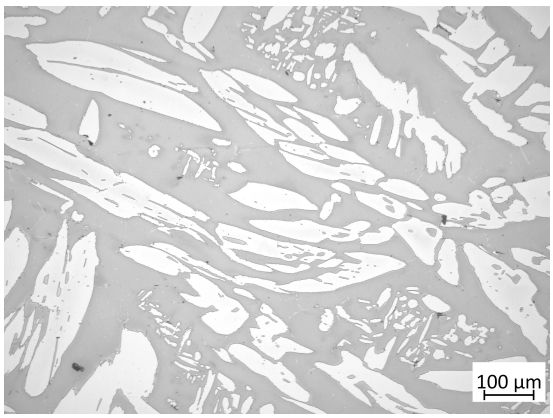

(b) FQ

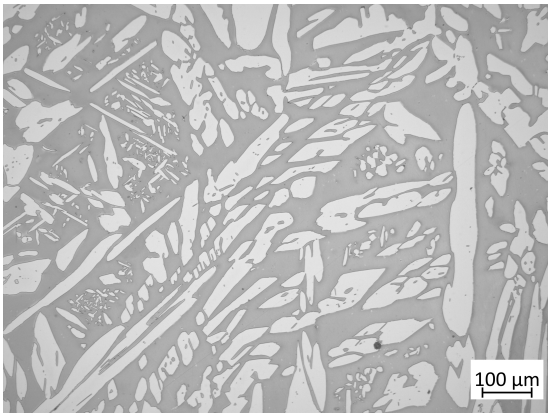

(c) S05

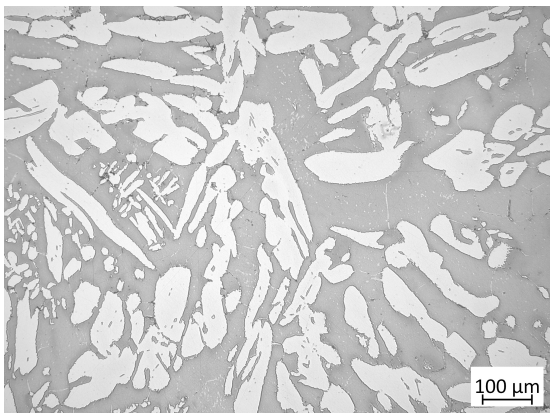

(d) F05

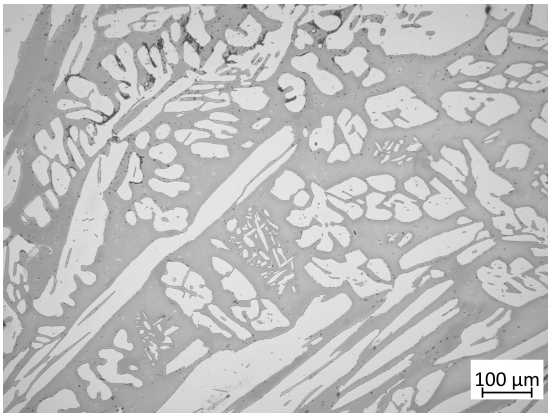

(e) S025

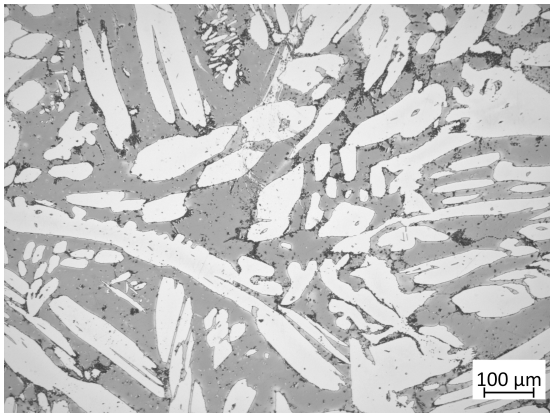

(f) F025

...

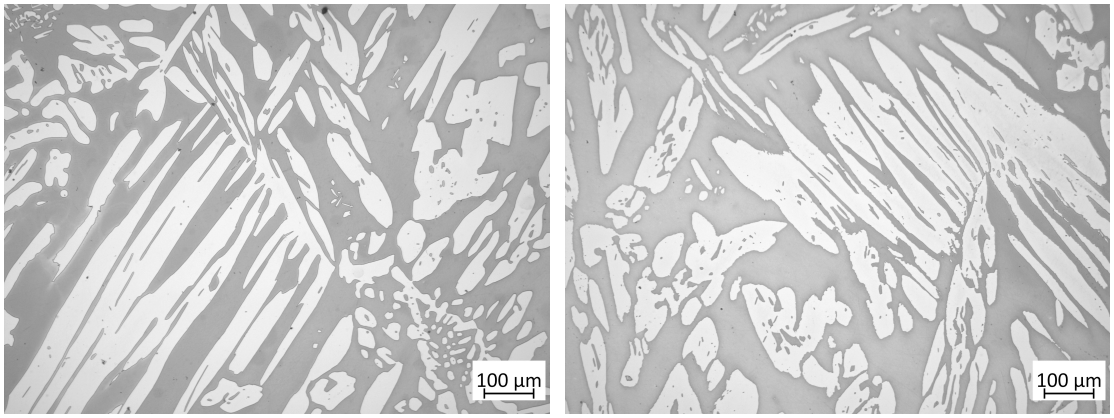

(g) Sstep (h) Fstep

Figure 3.2: *Optical micrographs after electrolytic etching in 20% NaOH*

phase precipitation interests ferrite/ferrite grain boundaries as well.

SEM examination

Secondary phase quantification required higher magnification and thus SEM images of electropolished samples in BSE mode were captured to achieve better resolution and improve visibility of the different precipitates. For each sample pictures of different regions were taken following a grid-like scheme, with a total of 30-40 fields per sample at 700x magnification, in order to determine a representative percentage of precipitates that is independent of the areas of higher and lower density which were detected during metallographic inspection. To consider the non-uniform distribution of data points, an alternative statistical approach using the median and median absolute deviation (MAD) was chosen, less sensitive to outliers with respect to standard deviation. The obtained calculations are presented in table 3.2.

From SEM-BSE images of electropolished specimens (fig.3.3) it can be seen that the interaction of back-scattered electron beam with the surface of the sample causes ferrite and austenite to appear dark grey and almost indistinguishable, while σ phase with its eutectoid morphology appears with a faded grey/white colour, due to its high Cr content (atomic number Z=24), and χ is bright white, since it is richer than σ in the heavy element Mo (Z=42) and is also enriched in Cr [43]. Due to their nano-scale size (50-100 nm), quenched-in nitrides are more difficult to detect with SEM-BSE and quantification would be precise only with instruments with a higher resolving power, like transmission electron microscope (TEM) [14]; intergranular nitrides appearance in BSE images is that of minute black-dot chains, owing to the lower atomic scattering factor of nitrogen; throughout the analysis, nitrides were detected either at δ/γ interfaces, inside ferritic grains or at δ/δ grain boundaries, as shown in fig.3.3(a). Isothermal nitrides (precipitated after cooling from lower temperatures) are coarser than quenched-in ones

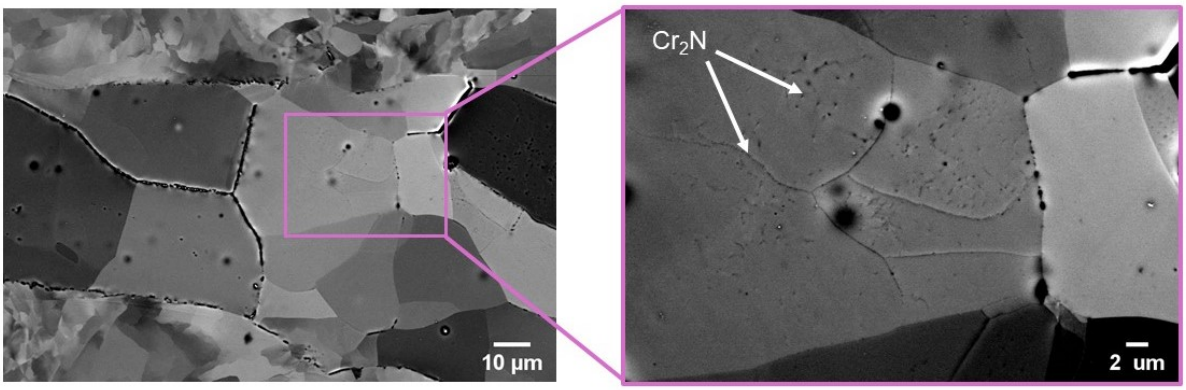

(a)

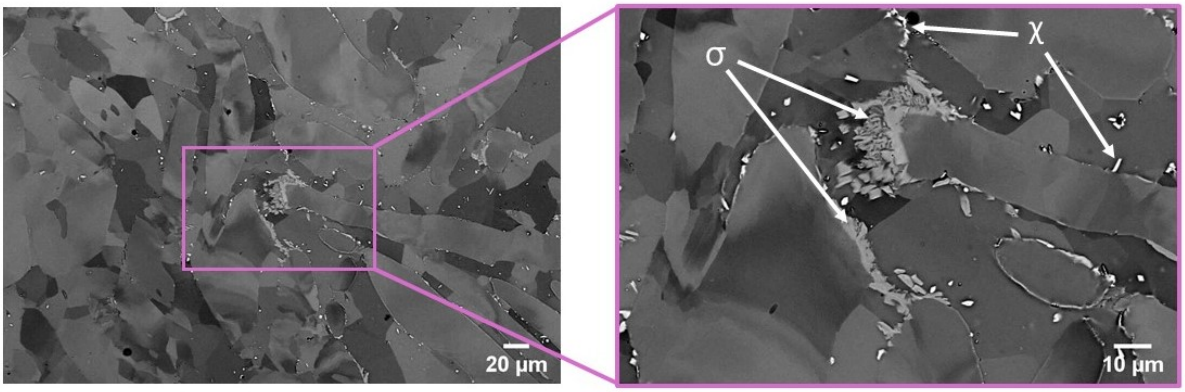

(b)

Figure 3.3: *SEM-BSE secondary phase morphologies after electropolishing for 20 s at 21 V of continuously cooled specimens: a) at 10 °C/s DEF, b) at 0.25 °C/s ND*

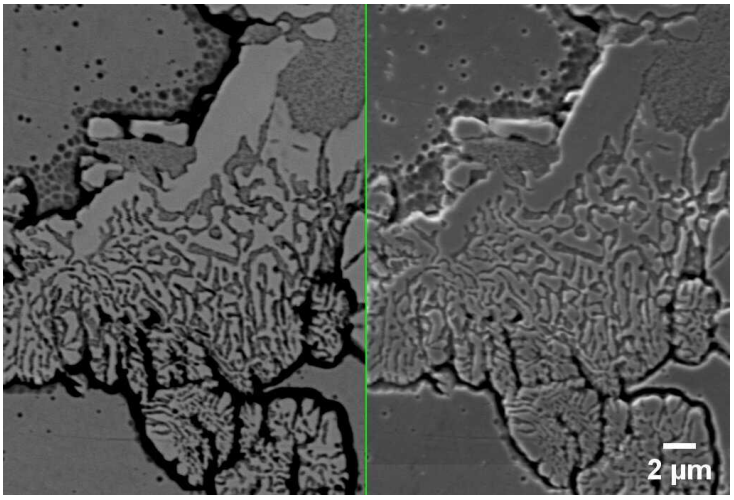

Figure 3.4: *Morphology of σ and γ_2 secondary phases precipitated in sample F025 in SEM-BSE (left) and SEM-SE (right) images*

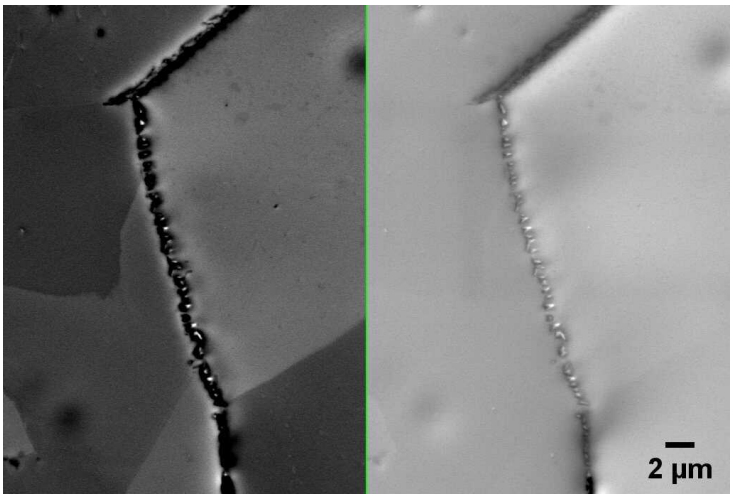

Figure 3.5: *Morphology of intergranular nitrides precipitated at γ/δ interface in sample F10 in SEM-BSE (left) and SEM-SE (right) images*

(80-250 nm), although their black appearance in BSE images makes them easily confused with inclusions and porosities. A magnification of precipitated nitrides is shown in fig. 3.5, where electro-polished sample F10 is displayed. It appears that precipitation of nitrides has occurred at austenite/ferrite grain boundary, as it takes place with an impoverishment of chromium from the ferrite matrix, which leads to a co-operative formation of Cr-poor secondary austenite [44], [45].

Samples SQ and Sstep, which exhibited maximum contents of ferrite, are accordingly characterized by non-detectable percentages of $\sigma + \chi$ phases. However, from accurate analysis of the SEM-BSE images, it is observed that both specimens show black vein patterns of nitrides 3.8(b), located at δ/δ boundaries as well as inside the ferritic grains in the shape of rodlike colonies.

It can be observed from fig. 3.8(a) that at an intermediate cooling rate of 0.5 °C/s, χ phase particles are more numerous with respect to σ. However, by halving the cooling rate σ phase reaches the same volume fraction and embeds χ particles, even exceeding its content when deformation is applied; thus as cooling rate is reduced, content of σ increases to its maximum value and χ gradually decreases. Such a transformation agrees with the precipitation kinetics theory according to which χ phase constitutes a suitable site for nucleation of σ [8]. Moreover, low cooling rates correspond to longer exposure times of the material at high temperatures, promoting the extent of σ phase transformation [46].

Sample F025 reveals the highest amount of secondary phases ($\sigma + \chi = 4.95\%$). Such result is consistent with the content of ferrite displayed in table 3.1, since precipitation of σ phase originates from δ/γ interface, consuming ferrite. Both SEM-BSE and SEM-SE images of sample F025 etched with 20% NaOH are visible in fig. 3.4: in BSE version, presence of dark gray

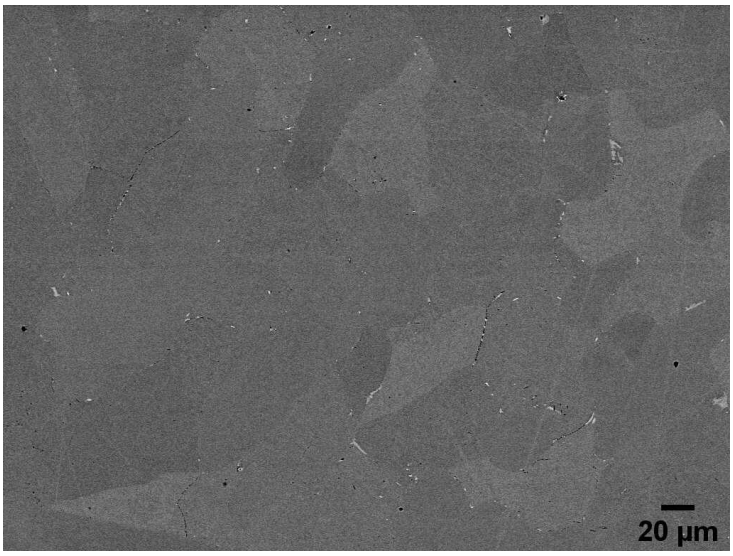

Figure 3.6: *SEM-BSE image sample F05 after mechanical polishing*

secondary austenite enclosed by eutectoid σ is detected, its colour related to its being devoid of heavy elements such as Cr and Mo. Formation of σ phase is known to create favourable conditions for γ_2 precipitation, which typically occurs in nitrogen-rich duplex microstructures at high temperatures [45]. Moreover, as precipitation of nitrides is associated to rejection of austenite-stabilizing elements like Ni and Cu into the ferritic matrix, the co-operative growth mechanism of nitrides and γ_2 is expected to occur [14].

Second in order of high intermetallics content is sample S025, the corresponding uncompressed version of sample F025, with a content of 0.26 %, followed by sample F05 with 0.25 %. Fig.3.3(b) shows how eutectoid σ phase in sample S025 branches off from austenite bands into the ferritic matrix, while white χ spots decorate the boundaries of austenitic grains, alongside with σ. While morphology and growth of σ and χ are very similar in samples F05 and S025, they do not share the exact same configuration of nitride precipitates. In particular, specimen F05 seems to be characterized by a higher density of nitrides, in the shape of the afore-mentioned dot chains, mostly at γ/δ interfaces but to a certain extent also at δ/δ grain boundaries, as can be seen in fig. 3.6. On the other hand, in sample S025 γ/δ nitrides are predominantly identified.
Sample F1 exhibits almost the same volume fraction of σ and χ phases, with a visible increase with respect to the sample without forging, in which no secondary phases were detected by SEM examination. A higher amount of precipitates was observed within the ferrite grains, although it is unclear if precipitation of nitrides occurred as a result of quenching from high temperatures. A decided increase in the appearance of intergranular nitrides is observed, as shown in fig. 3.7.

From the collected data it can be pointed out that forging always seems to deteriorate the

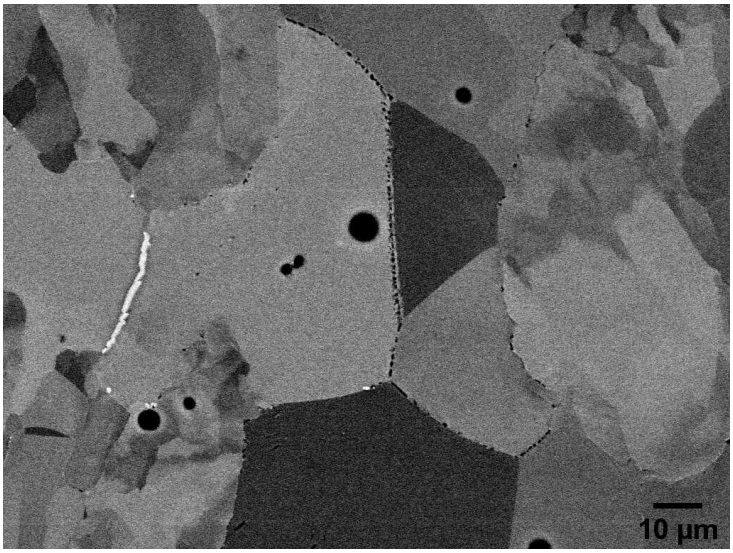

Figure 3.7: *SEM-BSE image of intergranular nitrides precipitated in sample F1*

integrity of the specimens in terms of precipitation of embrittling phases and leads to an increase of the precipitation rate. OM images of forged samples also show that deformation modifies the morphology of the two phases, coarsening and fragmenting their boundaries and thus increasing their surface to volume ratio, especially as cooling rates begin to slow down. There are however no notable differences in dual-phase partitioning. Another important

true deformation	**cooling rate**	**sample**	σ		χ		**total**
%	°C/s		%	±	%	±	%
0	≫10	SQ	<0.01	-	-	-	<0.01
	10	S10	<0.01	-	-	-	<0.01
	1	S1	<0.01	-	-	-	<0.01
	0.5	S05	0.01	0.01	0.03	0.01	0.04
	0.25	S025	0.15	0.08	0.11	0.03	0.26
	0.35	Sstep	<0.01	-	-	-	<0.01
50	≫10	FQ	<0.01	-	-	-	<0.01
	10	F10	<0.01	-	-	-	<0.01
	1	F1	0.05	0.03	0.04	0.01	0.09
	0.5	F05	0.16	0.06	0.09	0.05	0.25
	0.25	F025	4.12	0.55	0.83	0.11	4.95
	0.35	Fstep	<0.01	-	-	-	<0.01

Table 3.2: *Intermetallic phases content at different cooling rates and deformation degree, from 1100 °C*

observation made during examination of the surface of forged electropolished samples is the difference in the texture of austenitic and ferritic grains. In particular, fig. 3.9 shows how

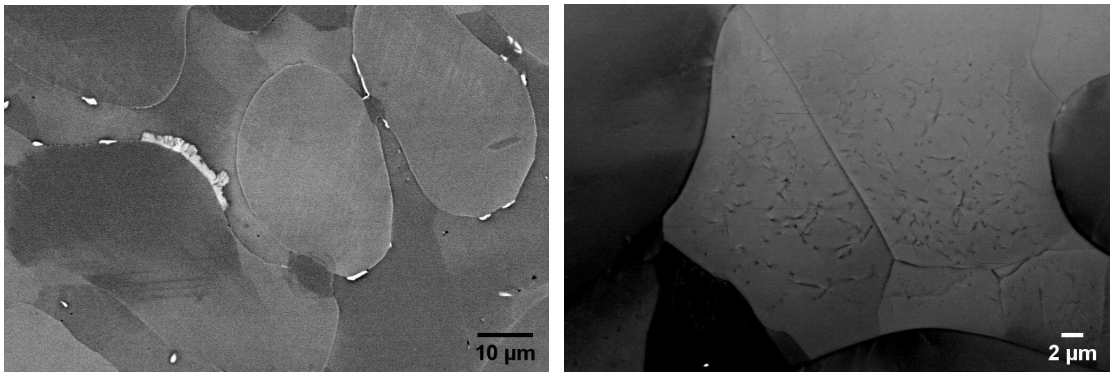

(a)

Figure 3.8: *SEM-BSE images of a) sample S05 after mechanical polishing; b) morphology of intragranular rodlike nitride colonies in sample SQ after electropolishing*

austenitic bands in specimen F10 are composed of seemingly larger and smoother grains, containing a few crystal twins which suggest that partial dynamic recrystallization occurred during forging. Electropolishing also highlights how the two phases acted differently during thermo-mechanical processing, since ferrite appears contituted of smaller fragmented grains, probably due to the difference in the stored energy during the deformation step.

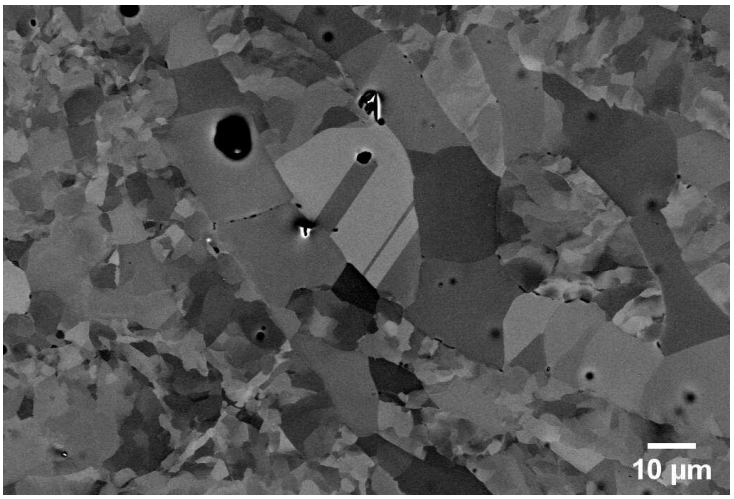

Figure 3.9: *SEM-BSE morphology of re-crystallized austenite after deformation in sample F10*

3.1.3 EBSD analysis

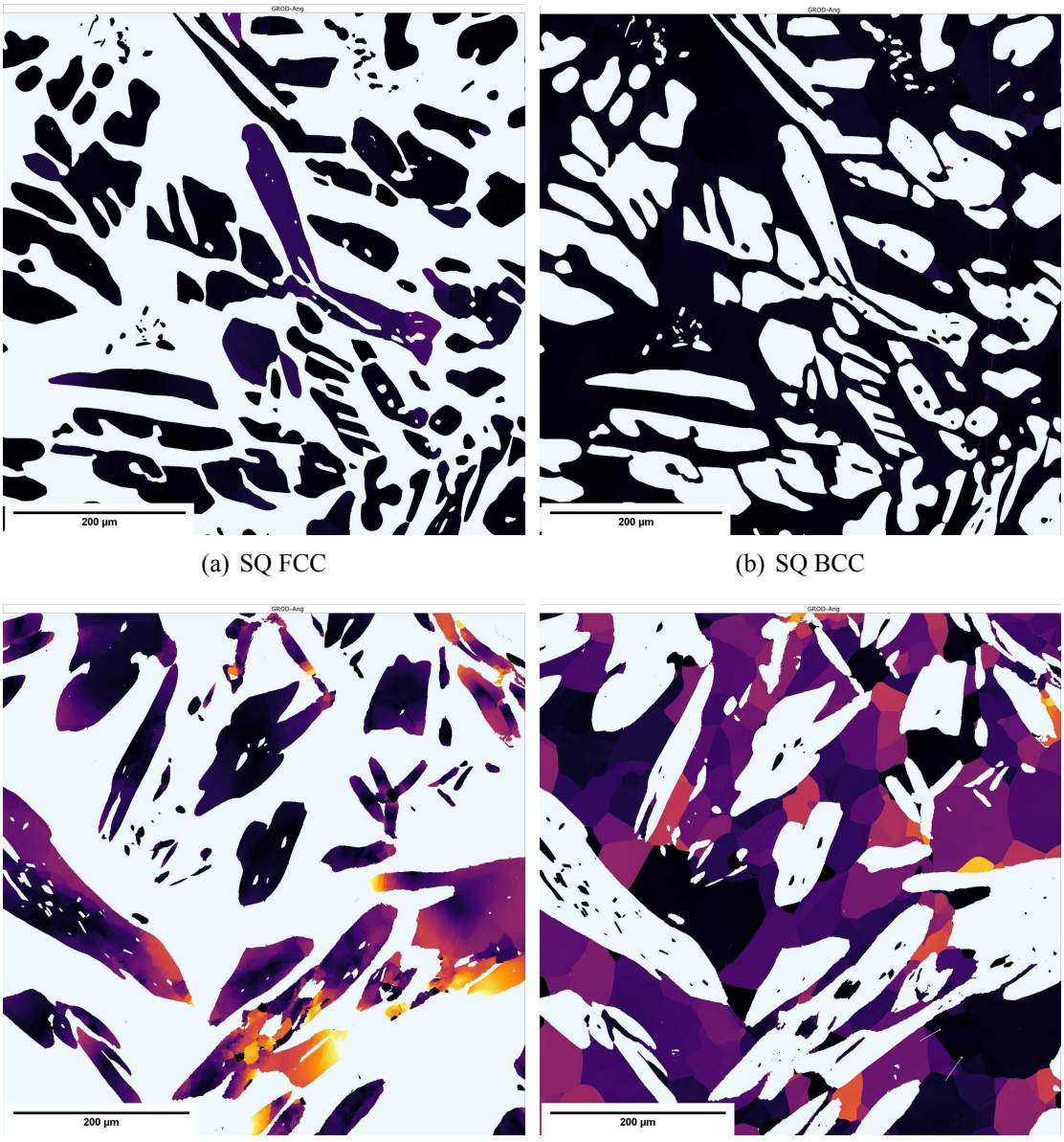

(a) SQ FCC (b) SQ BCC

(c) FQ FCC (d) FQ BCC

...

The thermo-mechanical processing behaviour of the three selected specimens SQ, FQ and F025 was investigated by EBSD approach based on grain reference orientation deviation (GROD) maps. Such maps are usually employed to observe the changes in grain orientation which take place during plastic deformation of polycrystalline materials. Each pixel in the grain is coloured based on the misorientation of the point in the grain with respect to a reference orientation. In this case a threshold angle of 15° was chosen for grain boundary definition. Fig. 3.10 shows GROD heat maps obtained with AZtecCrystal. As it was not subjected to forging, austenite and ferrite phases in sample SQ [fig. 3.10(a), (b)] did not undergo any softening mech-

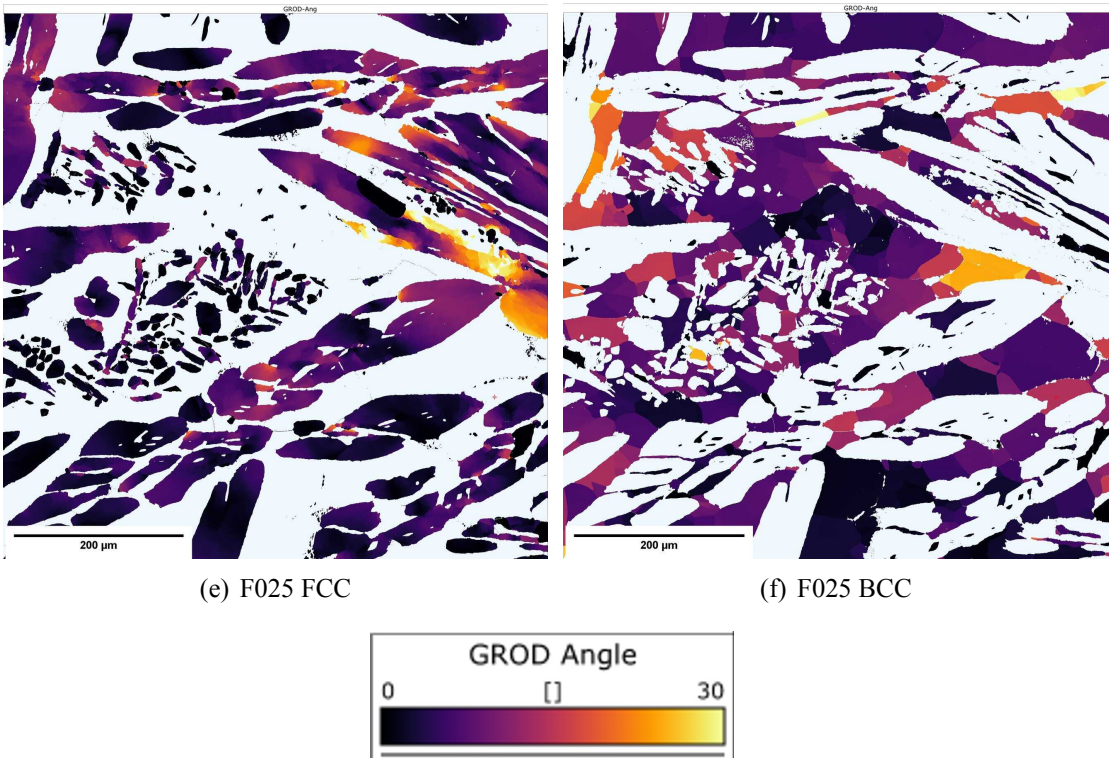

(e) F025 FCC (f) F025 BCC

Figure 3.10: *GROD maps*

anisms, as confirmed by the low local misorientation values (close to 0°, black tinted). On the other hand, as expected by its being the more ductile phase, austenite grains in specimen FQ denote clear signs of plastic deformation, associated to high GROD angles (about 30°, yellow). A significant change in local misorientation of grains with respect to the case without forging is also observed in the ferrite matrix: polycrystal plasticity causes high intergranular localized misorientation gradients, owing to the onset of dynamic recovery of ther ferrite, which leads to different accomodation gradients within the same phase.

Such phenomenon is even more highlighted in GROD maps of specimen F025. In the BCC maps of both forged samples, higher deviations from a GROD angle of 0° seem to be concentrated at interphase boundaries, which might be accounted for by the elastic and plastic mismatch between neighbouring grains belonging to different phases, thus favouring the activation of a high number of dislocation slip systems [47]. Nevertheless, confirmation of this hypothesis requires further elaboration of the EBSD images.

Moreover, specimen F025 is characterized by the beginning of dynamic recrystallization of austenite, which is outlined by the presence of clean black grains [see fig. 3.10(e)].

Fig. 3.11 shows the inverse pole figure EBSD maps for samples SQ and FQ. From IPF showed in fig. 3.11 it can be observed that specimen SQ is characterized by very few, coarse ferrite grains. IPF of specimen FQ exhibits a much more fragmented microstructure, in which subrains

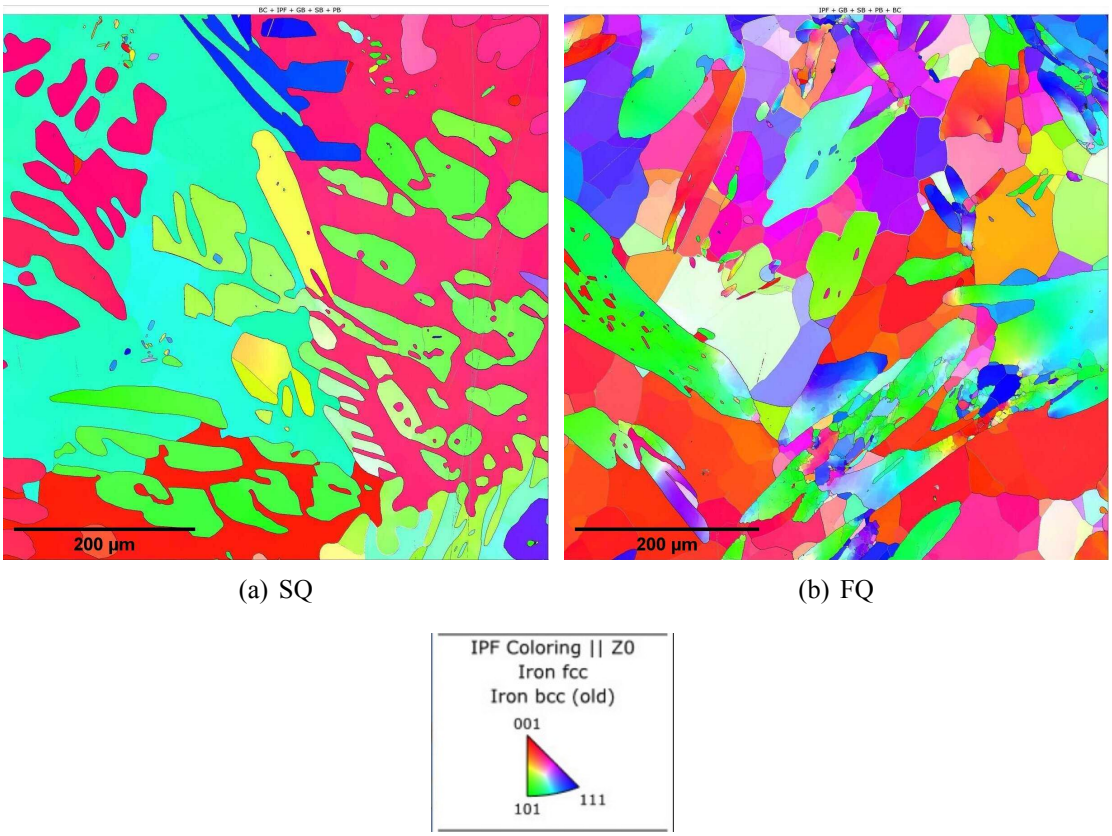

(a) SQ (b) FQ

Figure 3.11: *IPF of specimens SQ and FQ*

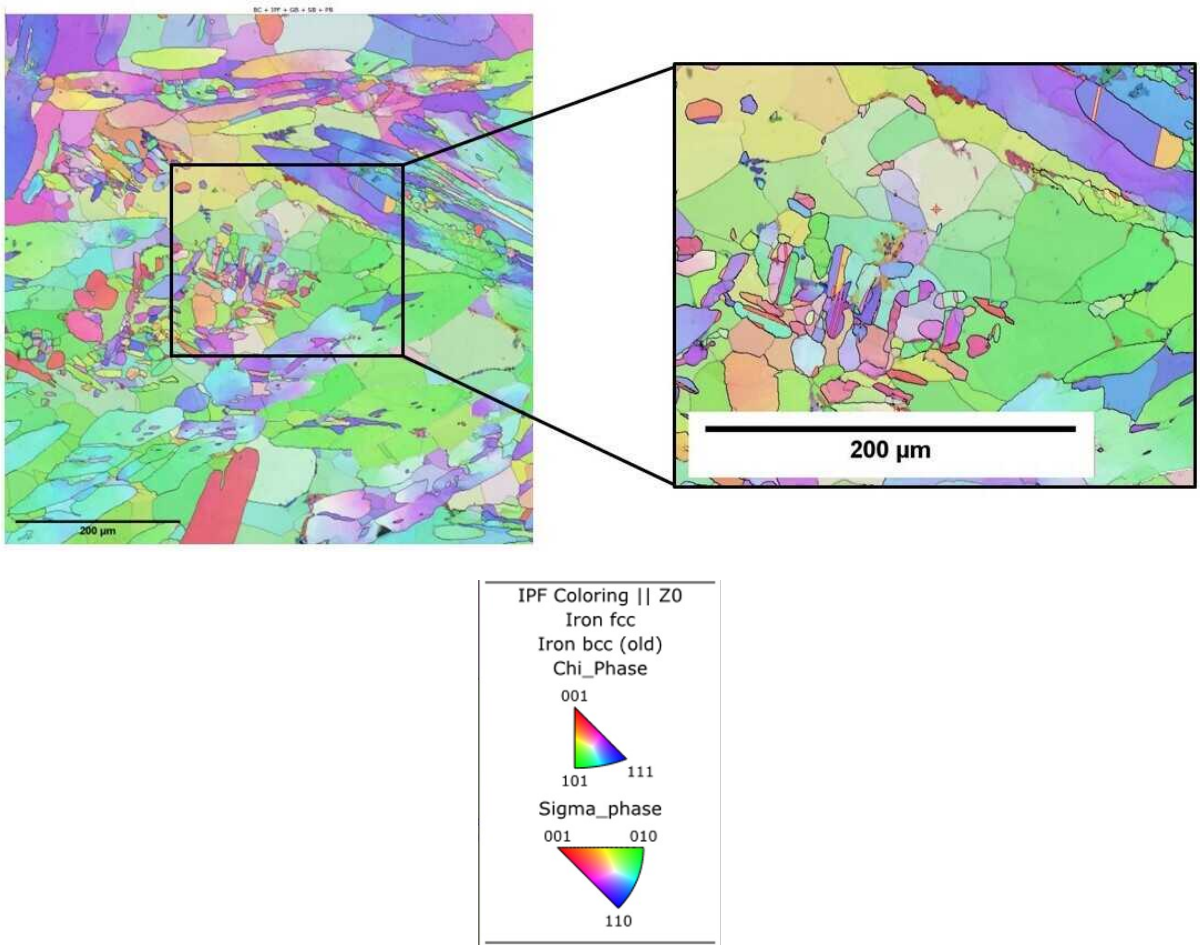

Figure 3.12: *IPF of specimen F025 with zoom on austenite twinning crystals*

are visible inside grains of ferrite. Moreover, clear signs of deformation are observed inside the austenite bands, hinted by the variety of colour-coded orientations that are found within each grain, highlighting the local misorientation caused by dislocation accumulations near grain phase boundaries. IPF maps of specimen F025 show the presence of twin nucleation sites, grown

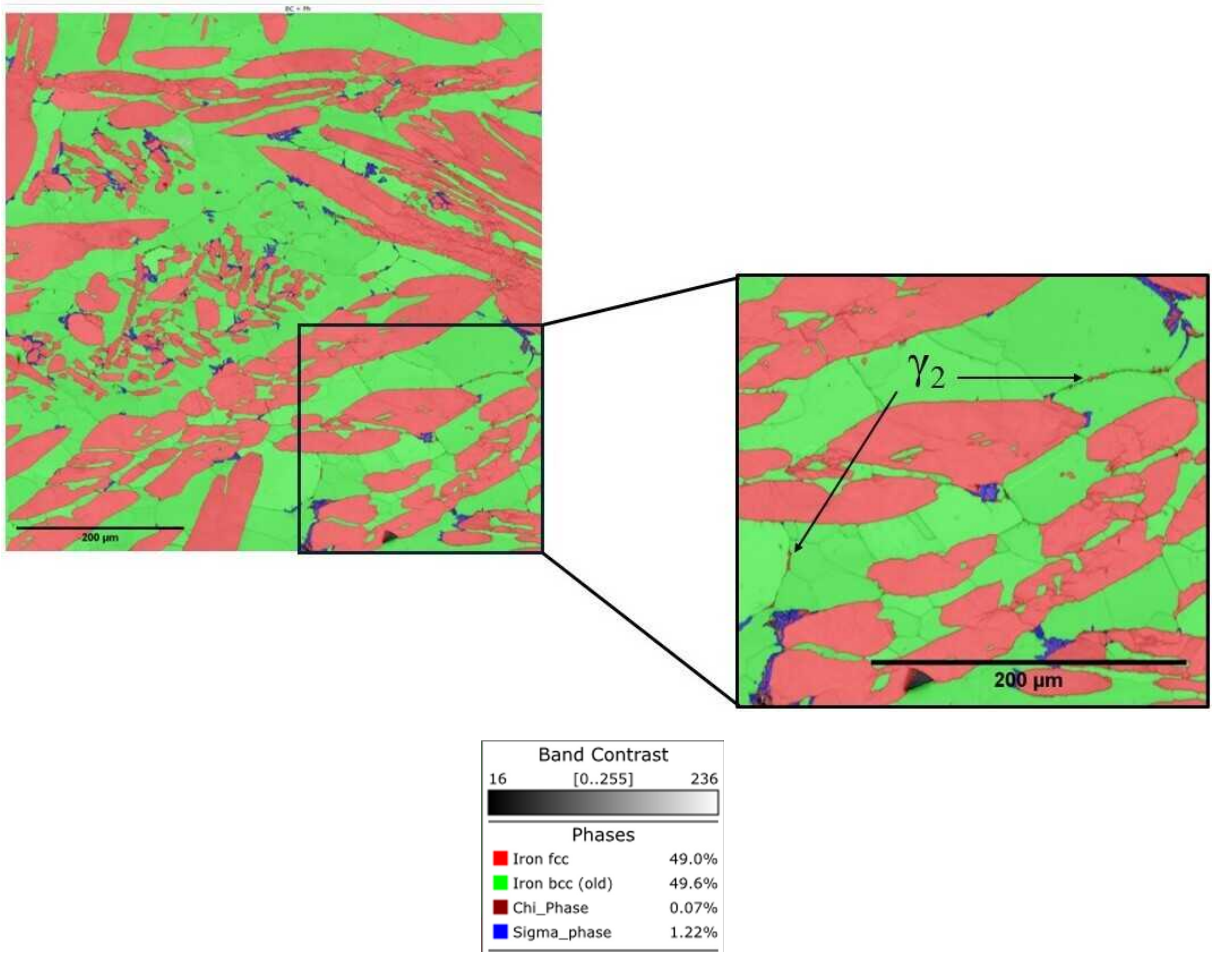

Figure 3.13: *Phase map of specimen F025 with zoom on allotriomorphic austenite bulging from δ/δ interfaces*

within deformed austenite grains, as can be observed in the upper right corner of fig. 3.12.
Fig. 3.13 shows the phase map of specimen F025, in which sporadic precipitation of red-coloured allotriomorphic austenite took place at ferrite/ferrite grain boundaries, as a result of prolonged exposure at high solubilization temperature. Moreover, blue σ clusters are visible at γ/δ interfaces, together with smaller spots of dark red χ phase, thus confirming the precipitate morphology which was previously observed by SEM. It is interesting to note that although precipitation of σ at γ/δ interfaces in specimen F025 is significant, some of the austenite/ferrite boundaries are precipitate-free. Haghdadi et al. suggested infact that propensity of sigma precipitation is directly related to the interface crystallographic properties [48]. While coherent and

low energy δ/γ interface in DSSs is usually well described by Kurdjumov-Sachs (K-S) orientation relationship, a study found that σ phase nucleates preferentially at large deviations from K-S, since larger $\Delta\theta_{K-S}$ are associated to lower activation energy barrier for σ phase formation [49].

3.2 Hardness evaluation

Table 3.3 shows the obtained values of Vickers hardness in the various thermo-mechanical processing conditions, while in fig. 3.14 hardness data are presented graphically.

These results are consistent with those found by other authors for thermo-mechanically treated

sample	**HV10**	±
SQ	277	7
FQ	279	5
S10	258	6
F10	261	4
S1	252	3
F1	263	4
S05	253	4
F05	258	8
S025	252	3
F025	270	8
Sstep	270	5
Fstep	273	7

Table 3.3: *Vickers hardness measurements with 10 kg load*

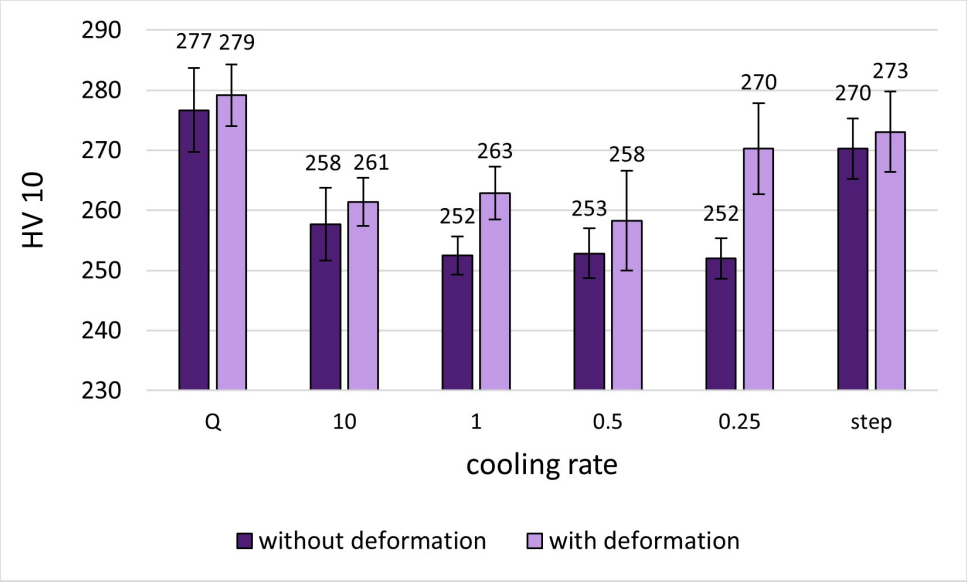

Figure 3.14: *Histogram of hardness level trend*

Zeron100 and high nitrogen DSSs [14]. In particular, it can be observed that annealing plus

deformation provide an increase in hardness, especially in specimens continuously cooled at 0.25 °C/s. While a general hardness increase in the forged specimens is probably caused by the texture evolution induced by plastic deformation, which is associated to a rise in the dislocation density [50], the significant shift in specimen F025 is most probably related to the precipitation of higher contents of σ and χ, whose significant brittleness is caused by their composition and crystal structure. Initial stages of precipitation of such intermetallics are characterized by a less noticeable embrittlement, as demonstrated also by Pardal et al. [51]. It is interesting to observe how sample F025 reaches the same hardness level as sample Sstep, although from microstructural investigation they exhibited very different contents of secondary phases. However small the size of precipitated chromium nitrides, it seems clear that their fine dispersion throughout the ferritic matrix is associated to higher hardness, confirmed by the highest hardness values obtained in samples SQ and FQ, in which intragranular nitride colonies were detected but σ and χ were absent. A similar behaviour with slightly less high values of hardness is observed in samples Sstep and Fstep.

Overall, hardness appears to have a constant trend in specimens cooled at 10, 1, 0.5 and 0.25 °C/s, with a modest increase after hot forging except in the case of specimen F025, in which the significantly higher presence of σ causes a noticeable rise in hardness.

3.3 Corrosion tests

3.3.1 DL-EPR results

Electrochemical evaluation

Figures 3.16(a) and 3.17(a) show the activation current I_a and reactivation current I_r of the tested specimens with and without deformation at different cooling rates, in the EPR solution of 33% H_2SO_4 + 2.5% HCl, at the scanning rate of 1.68 mV/s. The optimal solution was selected after several trial tests on AR specimen, in order to obtain a DOS around 0.01 % as the minimum value for appearance of reactivation peaks. Amongst thermally treated samples without deformation, a faint reactivation current is observed for samples cooled at high rates (SQ and S10), while no reactivation is found for the step-cooled sample. From 1 down to 0.25 °C/s an increasing trend can be detected, though reactivation current values remain limited. The same trend is seen for the samples with deformation; in particular, a noteworthy increase in I_r is observed at 0.25 °C/s, while comparable values are found at higher rates, in the same order of magnitude of the sample cooled at 0.5 °C/s. The lowest I_r is identified for the step-cooled sample, as was previously found in its non-deformed equivalent. Calculation of the DOS% in fig. 3.16(b) when no deformation is applied shows that sensitization gradually gets more substantial with decreasing cooling rate. Samples continuously cooled at high rates exhibit a DOS$<$1, meaning that sensitization is not significant. The highest degree of sensitization is found at 0.25 °C/s, with values of 7.18% for specimen S025 and of 22.47% for F025. In the latter example the increase of DOS after deformation is pronounced, while no significant changes are detected after deformation at 1 °C/s and 0.5 °C/s. Overall, the lowest DOS is observed in both configurations in the step-cooled sample, confirming that slow cooling from the solution annealing temperature to 1000 °C followed by quenching might be beneficial in the context of improving the the material tendency to sensitize.

Examples of DL-EPR polarization curves are displayed in fig.3.18, while linear plots assembling the DL-EPR response of all the specimens can be observed in figure 3.15. A decision was made to show the logarithmic plots obtained only for selected samples, where significant aspects emerged: this was done in order to ensure better clarity of the images without overlapping of exceeding data (also given the complexity of the curves). First, the AR sample curve was compared with the step-cooled sample without deformation (Sstep) in fig.3.18(a), for which the lowest DOS value was found, and with the sample cooled at 0.25 °C/s with 50% deformation (F025), which instead showed the maximum DOS [fig.3.18(b)]. During the forward potential scan of samples Sstep and F025, two current peaks can be detected: the first one, very faint, corresponding to the active dissolution of ferrite (around -0.3 V_{SCE}) and the second one,

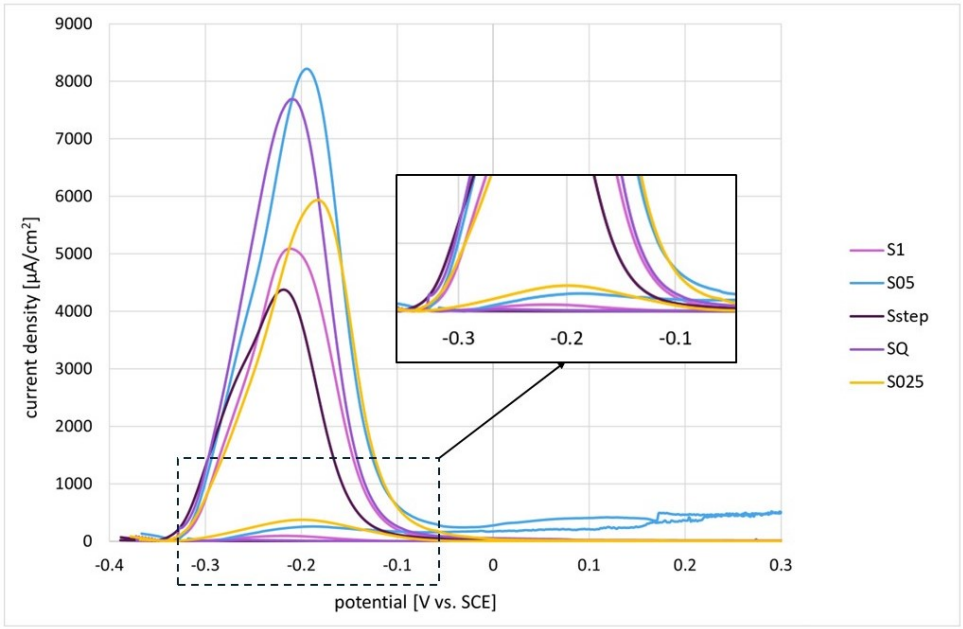

(a)

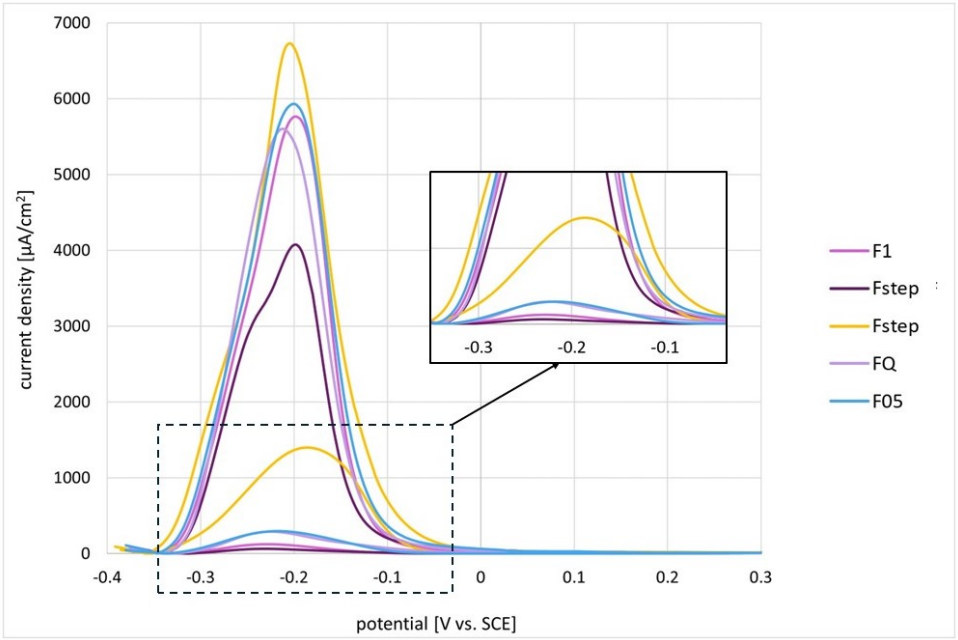

(b)

Figure 3.15: *Linear DL-EPR polarization plots of selected samples without deformation (a) and post-deformation (b) with local zoom where I_r appears*

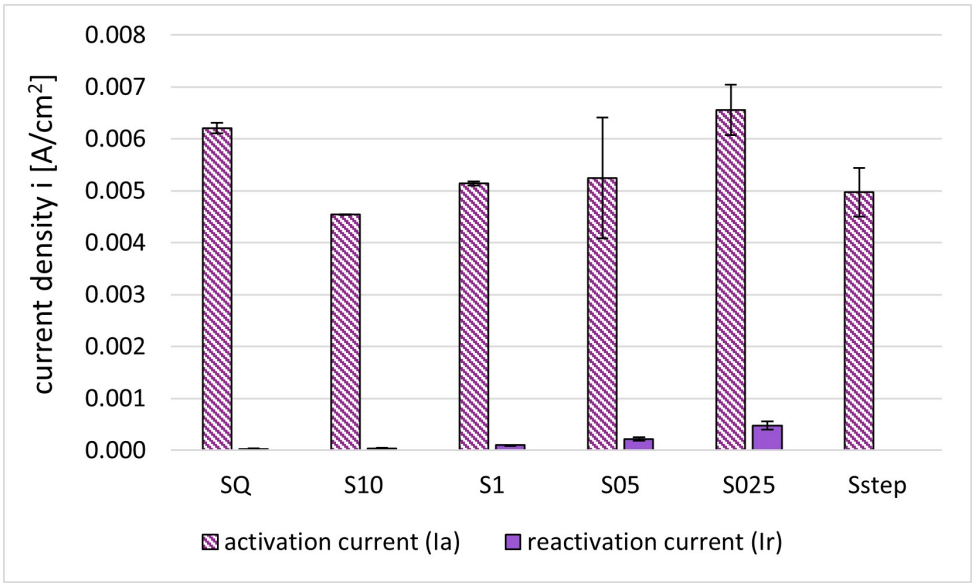

(a)

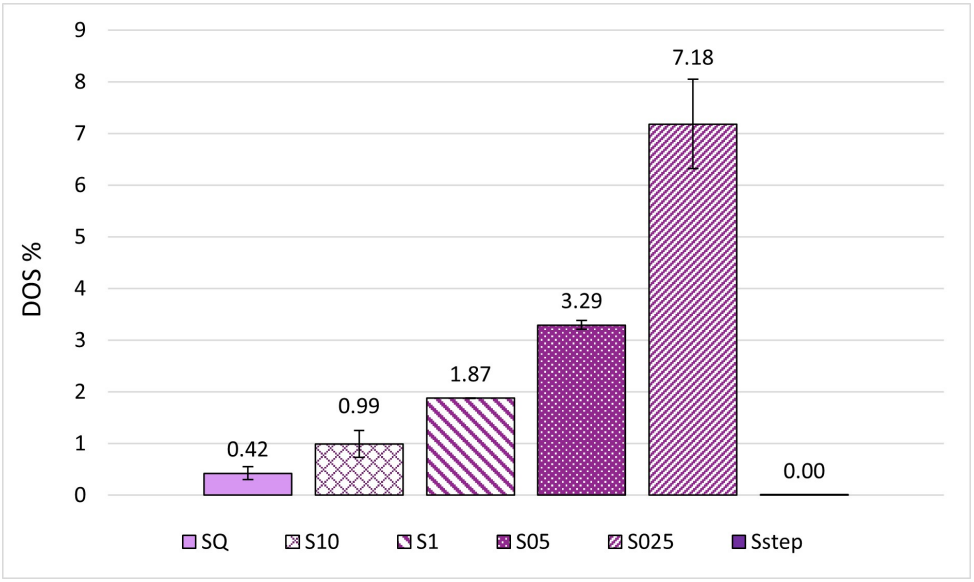

(b)

Figure 3.16: *DL-EPR parameters of specimens without deformation with different cooling rates obtained in solutions of 33% H_2SO_4 + 2.5% HCl at 1.68 mV/s: a) Ia, Ir; b) DOS %*

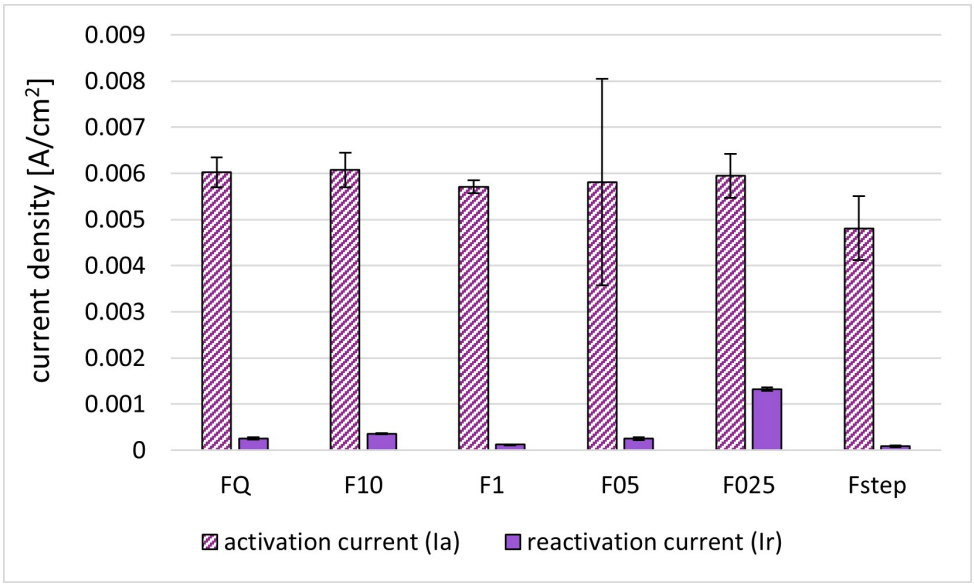

(a)

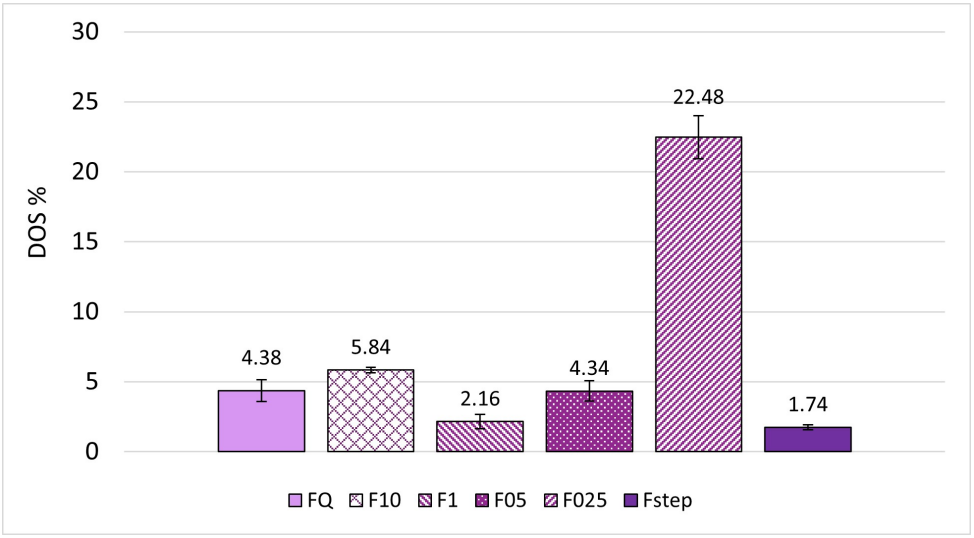

(b)

Figure 3.17: *DL-EPR parameters of specimens with 50% true deformation with different cooling rates obtained in solutions of 33% H_2SO_4 + 2.5 % HCl at 1.68 mV/s: a) Ia, Ir; b) DOS %*

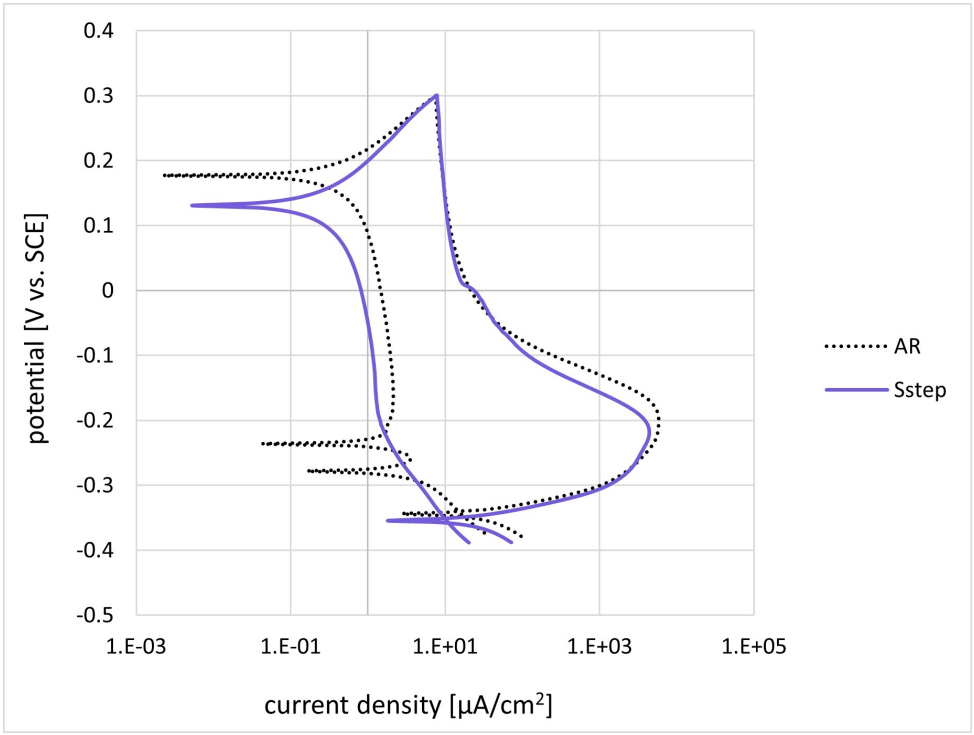

(a)

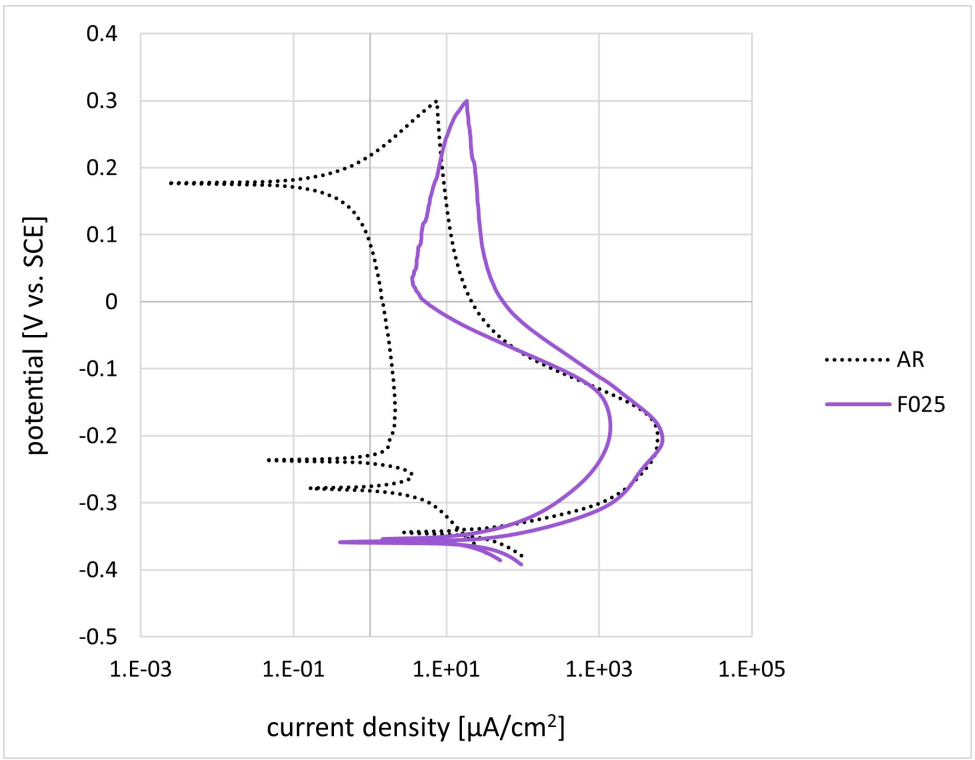

(b)

Figure 3.18: *DL-EPR polarization plots in 33% H_2SO_4 + 2.5% HCl at 1.68 mV/s*

clearly marked and matching the activation peak of the AR sample, associated to the activation of austenite (-0.2 V_{SCE}) [26]. The ferrite peak is not completely visible due to the relatively high imposed potential scan rate [28]. Moreover, while the passivity range of sample Sstep is characterized by almost identical current densities as the AR sample, sample F025 exhibits larger values (18.63 $\mu A/cm^2$ vs. 7.55 $\mu A/cm^2$ at +0.3 V_{SCE}); this shift is probably caused by the stronger sensitization of Cr-depleted grain boundaries in sample F025, which are therefore more prone to a corrosion attack and thus experience an increase in corrosion current. As can be observed from the graphs, current density during the backward potential scan is lower than the one measured during the forward scan, due to the formation of the passive film, which protects the material from the aggressive solution. The AR sample is characterized by a smooth and extended repassivation range, interrupted by a well-defined reactivation peak at -0.26 V_{SCE}, appearing as reactivation of the areas adjacent to σ and χ phase precipitates takes place. Being impoverished of Cr and Mo, these regions only form a weak and unstable passive film, more susceptible to acid attack and thus subject to higher current densities. This is particularly evident in the DL-EPR curve of sample F025, whose reactivation begins earlier (about 0 V_{SCE}) and reaches its maximum at -0.18 V_{SCE}, hinting to a very strong sensitization of the steel. Consistently with what expected, sample Sstep does not show any sign of a reactivation peak at the selected scan rate. Another comparison is presented in fig.3.19, where DL-EPR curves of sample F05 and sample S025 are shown. The two plots exhibit almost-matching current peaks, although during the backward scan current density of sample F05 is characterized by slightly lower values. Table 3.2 showed that the same volume fraction of secondary phases measured in the sample continuously cooled at 0.25 °C/s was found for the sample cooled at double the rate with an applied deformation of 50%. This represents an interesting result, since the two samples share very similar DOS % values, confirming that DL-EPR can be an effective method for quantification of the influence of certain precipitates.

Figure 3.15 shows DL-EPR curves with linear current density on the y axis. The local zoom on reactivation peaks confirms that an exceedingly slow cooling rate of 0.25 °C/s brings about a strong current increase during the cathodic scan, especially if preceded by forging. Nevertheless, continuous cooling at different rates without deformation does not cause as severe a shift in reactivation current, as can be seen in fig. 3.15(a) where the various peaks appear flatter.

Microstructure evaluation

SEM-SE specimen surfaces after DL-EPR polarization are shown in Figure 3.22, while optical micrographs of some of the most significant samples are presented in fig.3.20. Quenched sample with no deformation [fig. 3.20(a)] shows a considerable intergranular attack of the ferrite phase (detected as thin black grooves in both SEM and OM images), especially where interdistances

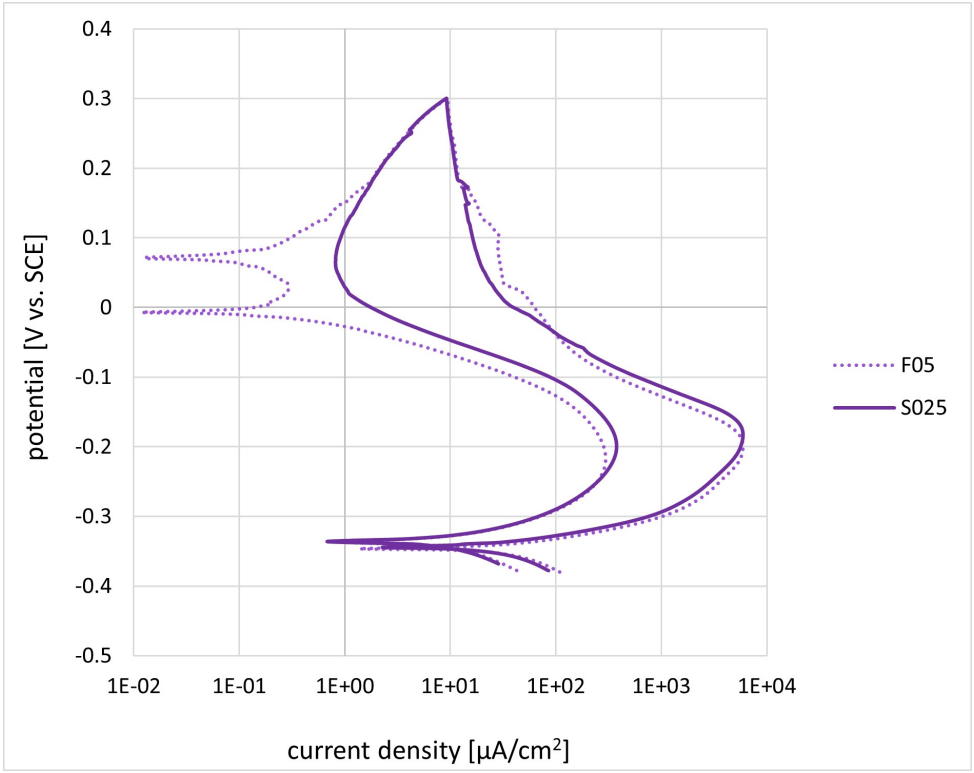

Figure 3.19: *DL-EPR plots of sample F05 and S025*

between γ and δ are wider; moreover, δ/δ grain boundaries act as nucleation sites for nitrides, as the dramatic cooling rates associated with quenching do not allow for the diffusion of nitrogen into austenite.

By reducing the cooling rate to 10 °C/s [fig. 3.22(c)], the issue of secondary phase precipitation persists, as it is also confirmed by literature with CCT curves of fig.3.21. Though σ and χ phases are not detected, nitrides are the first intermetallics to be formed and can be observed both at δ/δ interfaces and in the center of the ferritic grains. Deformation before quenching seems to exacerbate intergranular corrosion at ferritic grain boundaries as well as precipitation of nitrides, which are clearly distinguishable in fig. 3.22(b) in the shape of white thin needles. A worsening effect of deformation is also perceived in the specimen continuously cooled at 10 °C/s (d), where supersaturation of nitrogen is observed, as well as a significant sensitization at ferritic grain boundaries. Continuous cooling at 1 °C/s with no imposed deformation (e) causes strong precipitation of nitrides at γ/δ interfaces. With deformation (f), nitrides appear to precipitate both within ferrite grains, where they are expected to form from supersaturation, as well as at grain boundaries. Additionally, deformation contributes to an increase in sensitization products encircling the ferritic grains, rather than at the austenite interface. With a reduction in the cooling rate to 0.5 °C/s (g), an unmistakable rise in the presence of σ spikes is noted, forming at austenite crystal boundaries close to precipitated nitrides and growing up towards the δ phase.

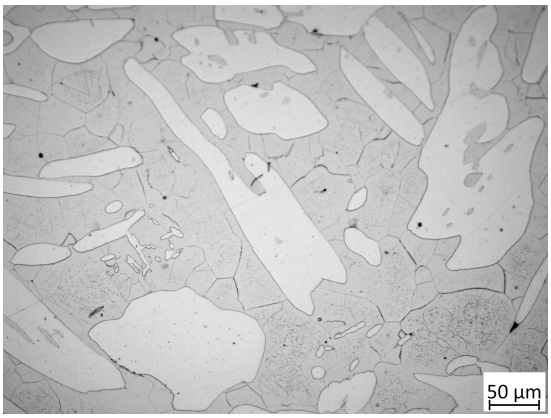

(a) SQ

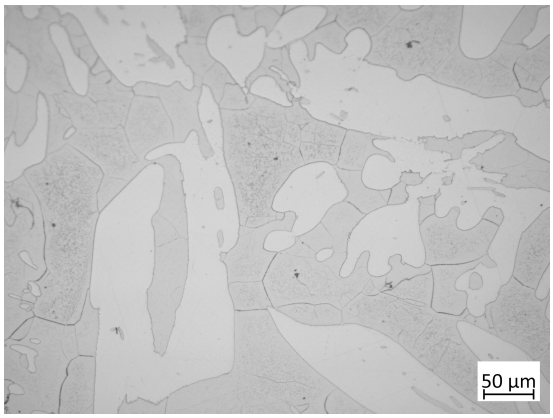

(b) FQ

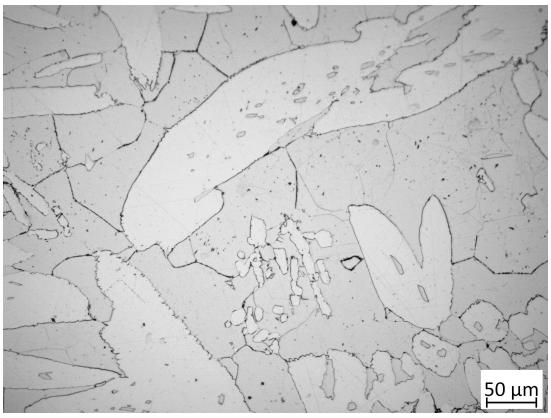

(c) F1

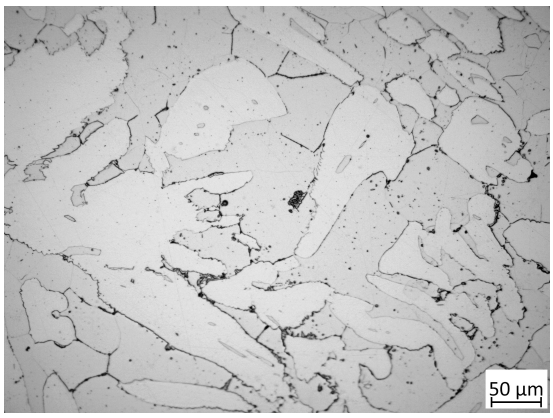

(d) F05

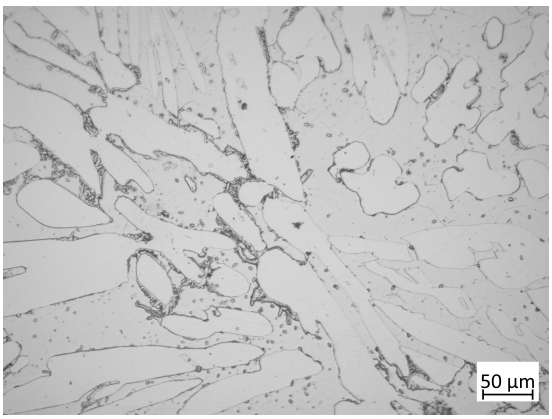

(e) S025

Figure 3.20: *Optical micrographs of specimens after DL-EPR*

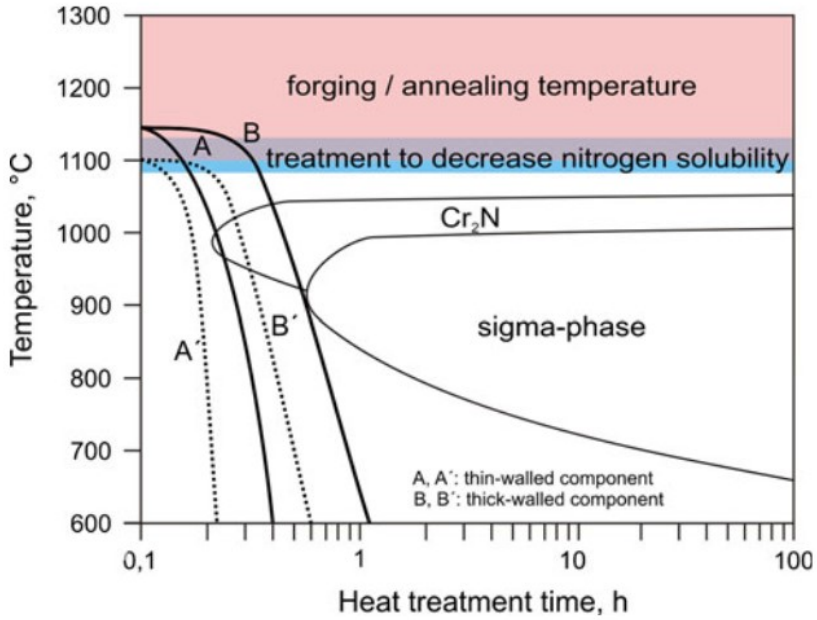

Figure 3.21: *Schematic representation of the heat treatment of thin- and thick-walled components, after reference [6]*

Small traces of χ phase can also be observed in the same areas, while nitrides content seems to be decreasing. With deformation (h), significant changes appear in the microstructure of this sample: rather large σ clusters are found at the fragmented edges of austenite bands; the intermetallic exhbits the typical coral-shaped morphology, with secondary austenite in-between its branches. A further reduction in the continuous cooling rate to 0.25 °C/s (i) worsens the precipitation of secondary phases at γ/δ boundaries, whilst χ phase speckles are detected throughout the ferritic matrix. Distinct sensitization around σ phase precipitate is observed, with no detection of nitrides. A very similar configuration is found for the equivalent sample with deformation (j), which exhibits more locally corroded areas (coloured black) at austenite/ferrite interfaces. Larger sensitized areas coincide with higher contents of σ, consuming Cr from ferrite in addition to promoting the formation of Cr-impoverished and Ni-rich γ_2 [8]. Interesting prompts arise from observation of SEM-SE images of step-cooled sample: in the case without deformation (k) the ferritic matrix appears homogeneous, with faint vein-patterned grain boundaries but without intermetallics of any kind; hot deformation seems to change this condition, clearly showing white nitride clouds inside δ grains, as well as distinct intergranular attack at δ/δ grain boundaries.

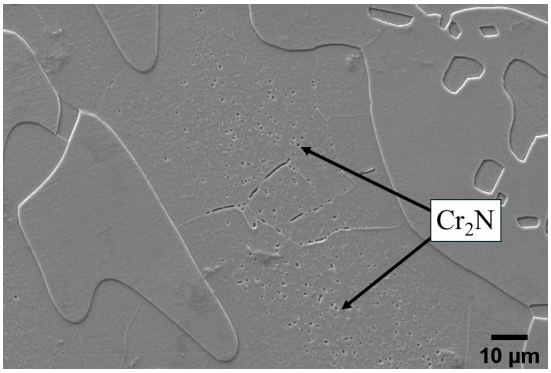

(a) SQ

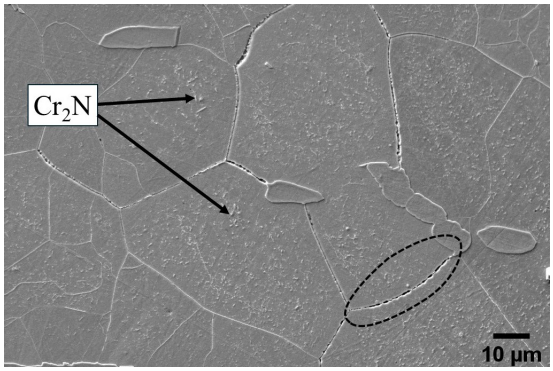

(b) FQ

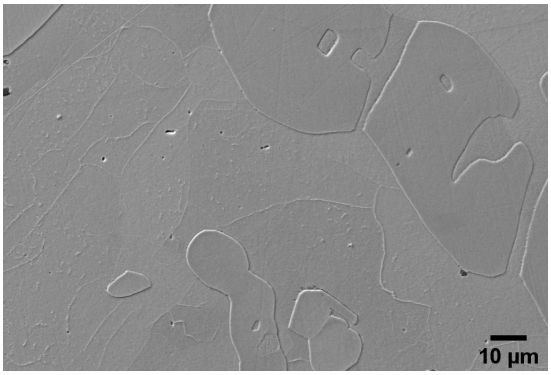

(c) S10

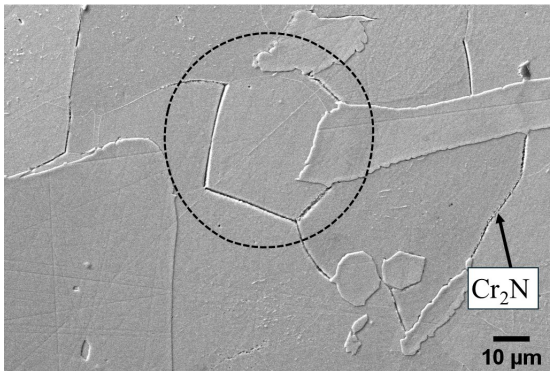

(d) F10

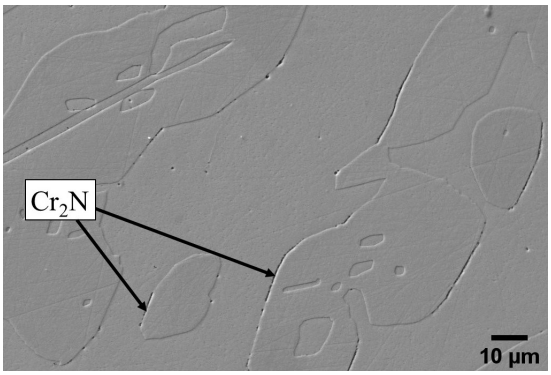

(e) S1

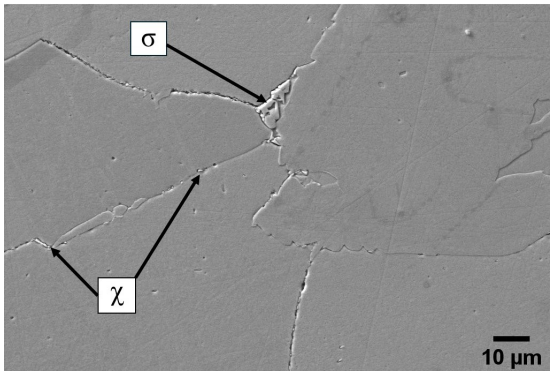

(f) F1

…

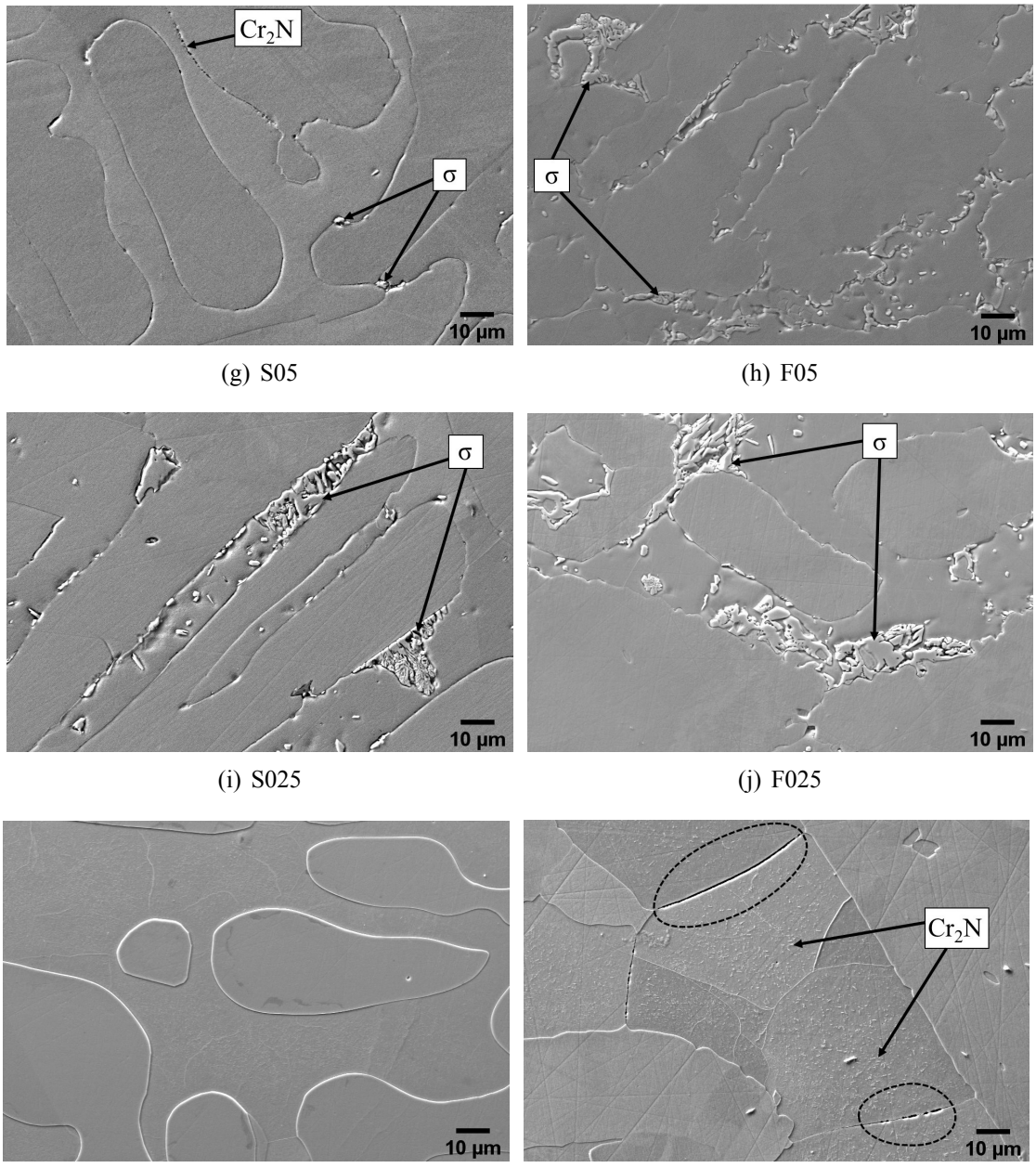

(g) S05 (h) F05

(i) S025 (j) F025

(k) Sstep (l) Fstep

Figure 3.22: *SEM-SE images at 2000x mag. of microstructural evolution of the samples after DL-EPR, before (left) and after (right) hot forging; examples of sensitized areas are highlighted with dashed circlets*

3.3.2 Anodic polarization results

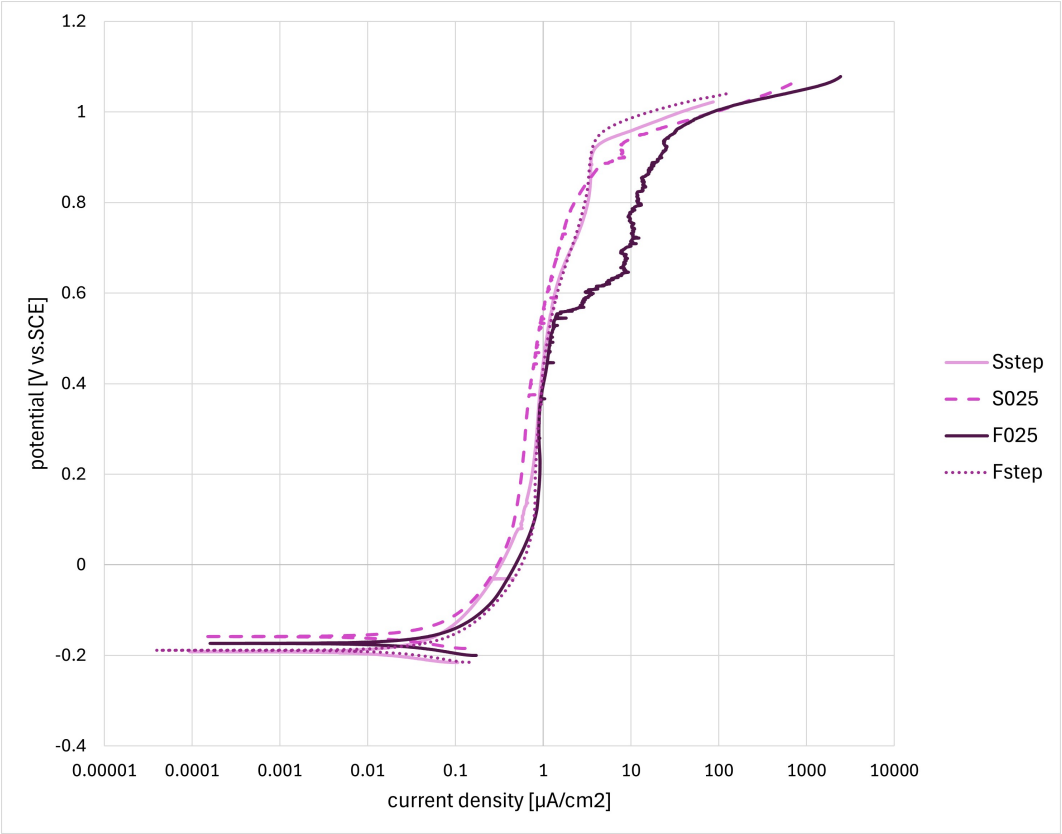

Figure 3.23: *Potentiodynamic anodic polarization curves obtained in 3.5% NaCl solution at 0.3 mV/s*

Anodic polarization tests were carried out on selected specimens with maximum and minimum DOS% values in order to understand if any matching trend with DL-EPR results existed. In particular, samples continuously cooled at 0.25 °C/s and at 0.35 °C/s to 1000 °C followed by quenching were chosen. Anodic polarization was performed on both thermally treated and forged specimens (see figure 3.23). Table 3.4 shows the parameters obtained from the potentiodynamic polarization plots. While pitting potentials found for samples without deformation and sample Fstep exhibit similar values around +0.9 V_{SCE}, specimen F025 displays a strong reduction in pitting corrosion resistance. In this latter case, anodic polarization results confirm what was previously found with DL-EPR: Cr-depleted areas resulting from intermetallic precipitation are not only way more susceptible to intergranular corrosion but also to the onset of pitting. It is reasonable to assume that the high degree of sensitization found in this sample (about 22%), together with its higher volume fraction of $\sigma + \chi$ phases, might translate to a significantly lower resistance of the passive film in correspondence of sensitized regions. However, it is also true that in the same sample without deformation no apparent change can be detected in pitting potential (only a slight increase in pitting current), although its DOS was equal to 7.18 %, substantially

higher with respect to the step-cooled sample (0.001 % without deformation and 1.74 % with deformation). Other studies have confirmed the fact that despite the presence of small amounts of precipitated secondary phases, the obtained results prove the effective protection provided by the passive layer on the investigated material [46].
Overall, anodic polarization does not seem to highlight with the same precision as DL-EPR the effects of sensitization in the steel. An important factor to take into consideration is that superduplex stainless steels performance in terms of pitting corrosion is first-rate, meaning that they exhibit exceptionally high values of pitting potential, as already mentioned in the previous chapters. The potential range in which they are expected to pit overlaps with the potential associated to the evolution of oxygen (OER), which is of 1 V_{SCE} in 3.5% NaCl aqueous solution. In alkaline aerated solutions, the oxygen reduction reaction consists in the oxidation of a water molecule as following:

$$O_2 + H_2O + 4e^- \rightarrow 4OH^- \tag{3.1}$$

Since the anodic polarization tests carried out during this experimental campaign were not in deaerated conditions, the rise in current observed at high polarizing potentials might be caused by OER rather than by transpassive dissolution due to localized corrosion of the steel.

sample	$\mathbf{E_{corr}}$	$\mathbf{E_{pit}}$	$\mathbf{i_{corr}}$	$\mathbf{i_{pit}}$
	V_{SCE}	V_{SCE}	$\mu A/cm^2$	$\mu A/cm^2$
Sstep	-0.19	0.93	3.91E-05	3.84
Fstep	-0.19	0.95	1.96E-03	4.59
S025	-0.16	0.90	1.31E-04	8.52
F025	-0.17	0.56	1.60E-04	2.14

Table 3.4: *Parameters obtained from anodic polarization plots in 3.5% NaCl solution at 0.3 mV/s*

3.3.3 CPT results

According to ASTM G150-18, the potentiostatic critical pitting temperature measurement is employed for product acceptance, alloy development studies and manufacturing control, since it provides a reliable assessment of pitting susceptibility in stainless steels. However, studies on the correlation between critical pitting temperature and intergranular corrosion sensitivity of DSSs are insufficient and the effects of the degree of sensitization on pitting resistance are still to be explored. Figure 3.24 shows the CPT curves obtained by applying a constant potential of +0.7 V_{SCE} to the electrochemical cell, while current and temperature are recorded. After approximately 60 seconds of response, current density stabilizes at 0.1-1 $\mu A/cm^2$ due to formation of the protective passive film. At low electrolyte temperatures metastable current peaks never ex-

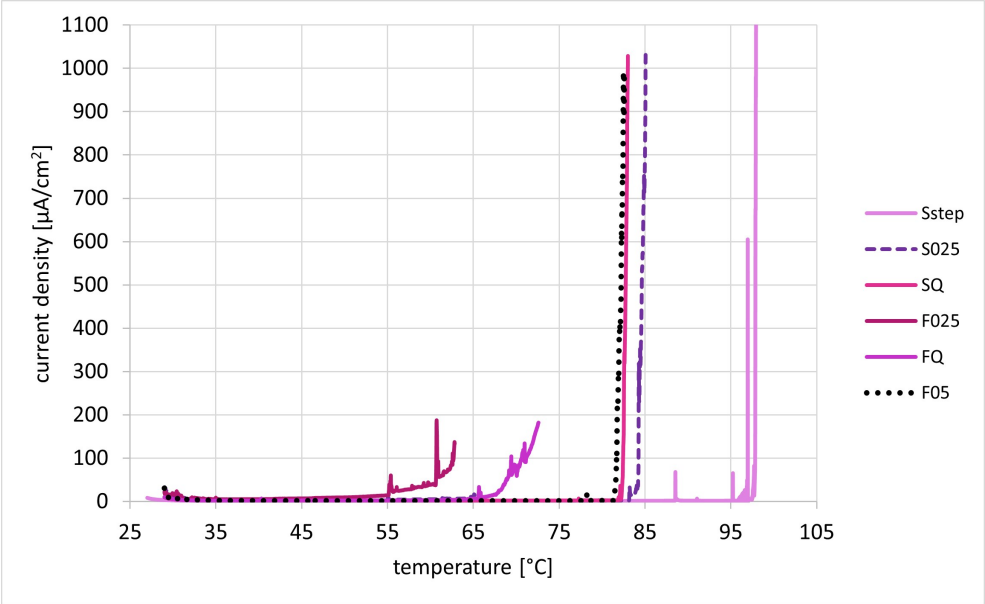

Figure 3.24: *Evaluation of CPT in UNS J93380 with potentiostatic measurements of various continuous cooling rates*

ceeding 20 μA/cm^2 appeared, whose transience is related to the development of unstable pits that get repassivated in a few seconds, as a dynamic equilibrium between chloride-ions attack and passive film formation is kept up. As the temperature rises, a sharp increase in current density takes place, meaning that formation of stable pits has occurred as passivity has been overcome. Table 3.5 lists the average CPT values measured on a selected set of samples, along with their experimental accuracy. In particular, quenched samples (SQ, FQ), continuously cooled at 0.25 °C/s (S025, F025) before and after deformation and at 0.5 °C/s with deformation (F05) were chosen in order to investigate the effect of high and slow cooling rates on pitting resistance; CPT test was performed also on the specimen Sstep, on which the intermediate cooling step was carried out. The obtained values are also presented in the histogram of fig. 3.25 for better

specimen	SQ	FQ	F05	S025	F025	Sstep
CPT [°C]	77 ± 1	67 ± 1	77.5 ± 2	75 ± 3	57 ± 2	91 ± 1

Table 3.5: *Critical pitting temperatures (CPT) of UNS J93380 in various thermal processing conditions*

clarity. The highest value was obtained for specimen Sstep, in which stable pitting initiated at about 90 °C, corresponding to the expected temperature for solution annealed UNS J93380 [34], [52]. The DL-EPR curve of the sample showed no reactivation peak, meaning that sensitization had not occurred; this was confirmed by the fact that neither σ or χ phases were detected by micrograph evaluation. A slow cooling rate with the addition of hot deformation leads to a strong CPT reduction, with a minimum value of 57 °C for sample F025, which showed the largest con-

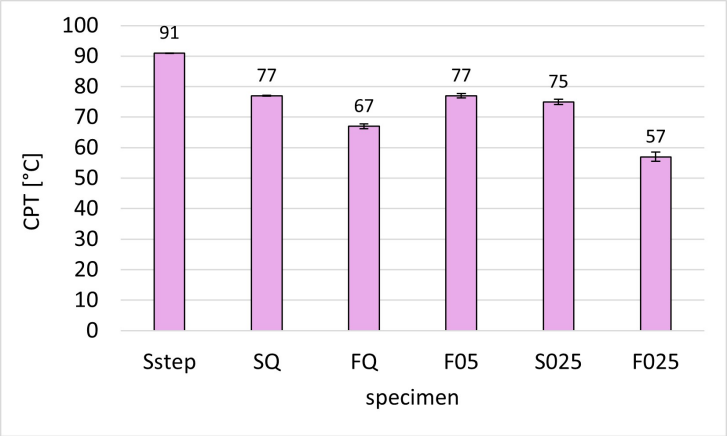

Figure 3.25: *CPT results*

tent of secondary phases as well as the highest DOS. Such strong pitting susceptibility can be traced back to the Cr-depleted areas created by the extensive σ-phase precipitation, where lower Cr concentration weakens the passive film and acts as a preferential attack site for chloride ions [53].

Sample S025 exhibits a significant CPT increase of approximately 20 °C, which is consistent with the difference in DOS found for the two samples. This can be attributed to the fact that precipitates forming with simple cooling at 0.25 °C/s are small, therefore sensitized areas will also be limited; thus while IGC occurs, it will not be as severe as after hot forging. Hot deformation infact leads to a distinct coarsening of precipitates, which worsens the IGC susceptibility as well as the resistance towards pitting due to larger Cr-depleted areas.

It is interesting to note that the simply quenched sample shows a very similar CPT value to the one continuously cooled at 0.25 °C/s, although DL-EPR resulted in a DOS of 0.4 % for the former and 7 % for the latter. This finding is probably related to the difference in the depth of sensitization in the two samples: sample S025 might be characterized by more widespread precipitation of rather small-sized intermetallics, whose related sensitized areas affect IGC during DL-EPR but not so much pitting [54]. Another confirmation of this hypothesis is presented by the fact that forged and quenched sample exhibits a worse behaviour towards pitting with respect to sample S025, although their DOS is very similar. In addition to the distribution and size of σ phase, the decrease in critical pitting temperature might also be caused by precipitation of alternative secondary phases. A contributing effect is likely to arise from precipitation of χ phase and nitrides at δ/δ grain boundaries, the latter of which appears to be significant in sample FQ. Ebrahimi et. al [55] found that Cr_2N precipitates are likely to lead to formation of chromium-deficient zones, especially when they precipitate co-operatively with Cr-poor secondary austenite, resulting in a great decrease in CPT. Other studies also confirmed that as both χ and Cr_2N can be expected to cause Cr and Mo depletion from the surrounding matrix, their

precipitation is associated to a consistent reduction in the PREn of these localized areas [46]. For example, Nilsson et al. [44] found direct evidence of pitting attack on aged 2507 DSS in which σ-phase was completely absent.

Sample F05, forged and continuously cooled at 0.5 °C/s, exhibits a CPT of 77 °C. With the

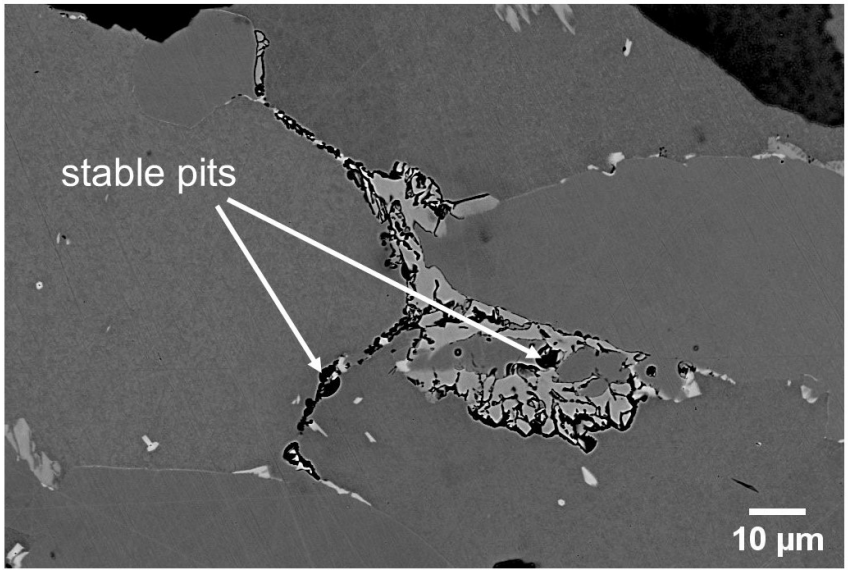

Figure 3.26: *SEM-BSE pit morphologies on the surface of specimen F025 after CPT test (2000x mag.)*

same DOS as sample FQ (about 4 %), sample F05 is characterized by a higher content of both σ and χ but in this study it was found to display higher tolerance with respect to pitting corrosion, confirming the fact that nitride precipitation in sample FQ can be more detrimental than expected.

SEM-BSE image of figure 3.26 shows the location of stable pits in sample F025, predominantly occurring next to σ phase structures and at δ/δ grain boundaries, which are prone to intergranular corrosion. Fig. 3.27 reveals the morphology of pits formed during CPT measurements: the cavities are few and far between on the surface of the specimens and exhibit jagged edges similar to erosion. It appears as if after the triggering of the first pit the attack was enforced in the same area, as a potential confirmation of the presence of particularly sensitized spots spread throughout the surface.

Overall, the correlation between critical pitting temperature and sensitization does not appear to be linear, as confirmed by previous studies [54]. From the obtained measurements, it is reasonable to assume that the critical pitting temperature is less affected by the extent of sensitized areas but rather by their depth. Pitting may also be triggered at different temperatures depending on where the area exposed to the electrolyte is located, since intermetallic precipitation does not necessarily occur evenly throughout the surface of the specimen. Moreover, the samples were characterized by a certain degree of intrinsic porosity originated from casting, which could def-

initely act as nucleation sites for pitting.

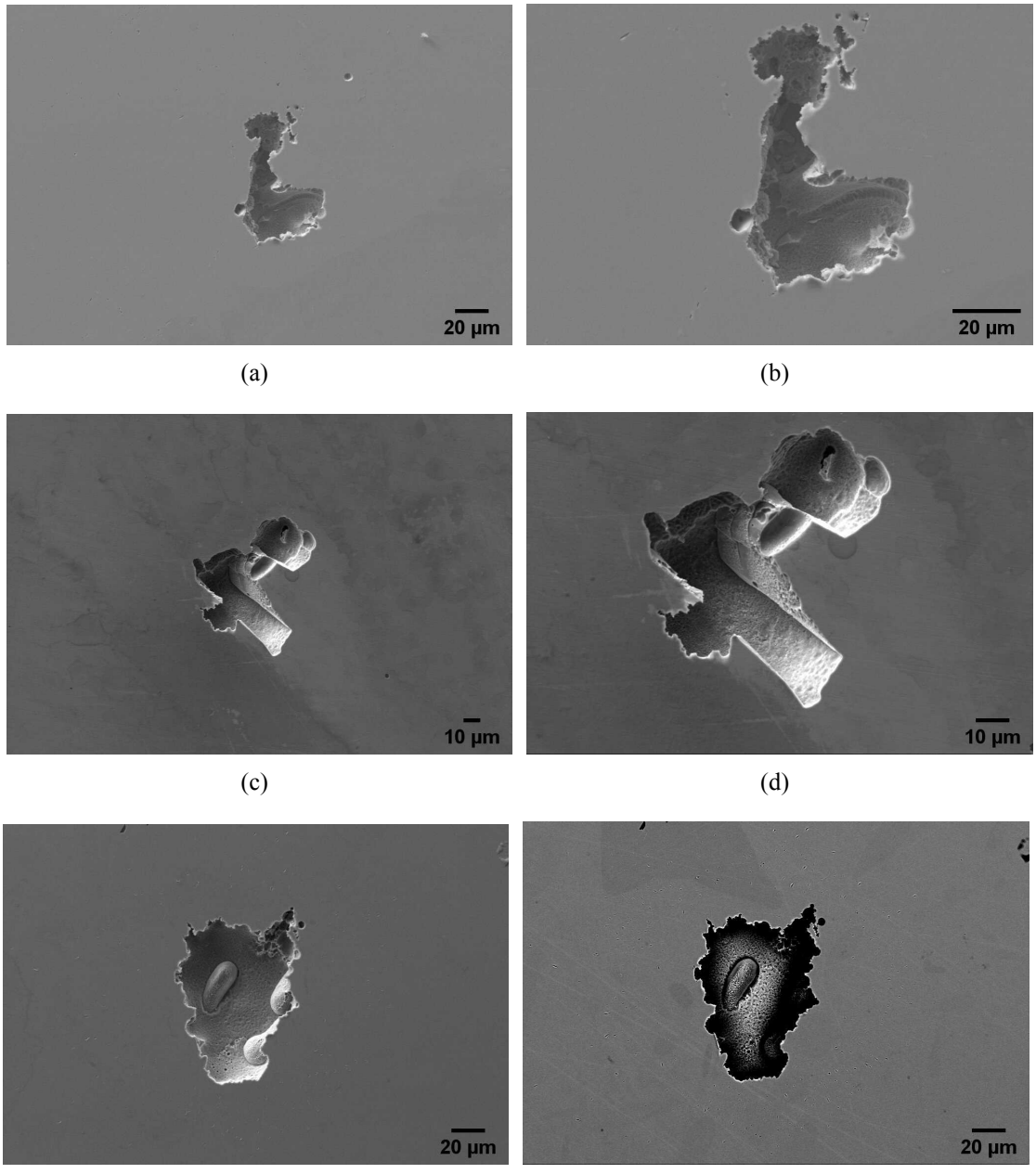

Figure 3.27: *SEM-SE images at 1000x (left) and 2000x mag. (right) of pit morphologies after CPT on specimens: a), b) S025; c), d) Sstep; images e), f): comparison between SEM-SE and BSE at 2000x mag. of pit formed on simply quenched sample*

Chapter 4

Conclusions

In this research, the influence of precipitated secondary phases on the microstructure and corrosion behaviour of UNS J93380 duplex stainless steel under various thermo-mechanical processing was investigated. Amongst the many objectives of the experimental campaign, the analysis focused particularly on:

- the compared effects of rapid and slow continuous cooling from high solution annealing temperatures on the thermodynamics and kinetics of secondary phase precipitation, mainly σ, χ and chromium nitrides;
- the effect of forging followed by continuous cooling on the morphology of secondary intermetallic precipitates;
- the corrosion behaviour associated to different thermo-mechanical processing parameters, especially in terms of intergranular corrosion and pitting;
- the sensitivity of DL-EPR technique to the presence of secondary phases and how it relates to other standard corrosion measurements, such as CPT.

State of the art

As of today, duplex stainless steels are successfully employed in many industrial applications under severe corrosion conditions, like oil extraction, paper manufacturing and seawater handling systems. DSS cast products are commonly subjected to open-die forging in order to obtain components for the piping industry, which are assembled together by subsequent welding processes. Current industrial practice consists in heating the piece to 1130-1150 °C to dissolve any impurities coming from casting, followed by forging in the range 1000-1150 °C [56]. A final

solution annealing treatment is performed at the same temperature in order to eliminate precipitated intermetallics, which are known to cause embrittlement of the structure. This research explores the suitability of an alternative thermo-mechanical processing technique, which does not require repeated heating schedules but performs open-die forging right after a selected soaking time at solution annealing temperature and quenching or continuous cooling directly after hot deformation.

When considering the effects of forging on precipitation of secondary phases, issues regarding the corrosion response of the material are a priority. Intermetallic precipitation is reported to cause alloying elements depletion from the ferritic matrix, jeopardizing the resistance towards intergranular corrosion. Part of this work addresses the efficiency and reliability of double-loop electrochemical potentiokinetic reactivation on duplex stainless steels, an established technique for detecting sensitization in austenitic grades. The obtained results were compared to the ones revealed by metallographic inspection and to other corrosion examinations.

Microstructure and DOS

Metallographic inspection of the thermo-mechanically processed samples showed that a decrease in the cooling rate is associated to an increase of the volume fraction of precipitated secondary phases; it was observed that either without or with forging the first precipitate to nucleate was intergranular χ phase, which acted as a nucleation site for the growth of eutectoid σ, whose maximum measured volume fraction was of 4.95 % for the specimen forged and cooled at 0.25 °C/s. For all specimens, austenite appeared free from secondary phase precipitates, as diffusion and segregation rates of alloying elements are slower in this phase. Micrographs of samples cooled at high rates highlighted the presence of pepperlike nitride colonies precipitated within the ferrite grains due to nitrogen supersaturation. At lower cooling rates (e.g. 1 °C/s) a majority of intergranular isothermal nitrides were observed, caused by the longer exposure times at high temperatures.

DOS calculations for samples subjected to high temperature solution annealing followed by simple cooling seem to reflect the trend of secondary phase precipition, since DOS appears to increase with increasing intermetallics content. Moreover, the step-cooled sample exhibited minimum reactivation during DL-EPR as well as no detectable content of σ or χ.

Open-die forging causes a change in the overall trend of the specimens. In general, deformation causes recrystallization phenomenona associated to an increase in the amount of grain boundaries as well as misorientation among grains, which favour σ phase nucleation [57]. While forging always leads to a rise in the precipitates content and worsens the sensitization behaviour with respect to the case without deformation, the correlation between secondary phase volume fraction and degree of sensitization is not linear. Forged specimens cooled at

high rates (FQ, F10) are characterized by irrelevant contents of σ and χ but reveal a DOS of 4-5 %, in the same order of magnitude as sample F05, in which a content of 0.25 % $\sigma + \chi$ was found. Additionally, specimen F1 has a lower DOS compared to the afore-mentioned samples, although showing a secondary phase content of 0.09 %.
More severe sensitization on specimens with comparatively low amounts of $\sigma + \chi$ can be related to the formation of either intergranular or intragranular chromium nitrides, whose presence was confirmed but not quantified. Many studies state that nucleation and growth of such nitrides is associated to a depletion of Cr from the sorrounding matrix [44]–[46], which makes these areas susceptible to intergranular corrosion and thus appreciated by potentiokinetic reactivation techniques [53]–[55].
Observation of the micrographs obtained after DL-EPR shows that preferential dissolution has occurred along ferrite/ferrite grain boundaries in both quenched samples (SQ, FQ) as well as in sample F10. In samples cooled at lower rates no selective dissolution of ferrite was detected, while IGC originated along the austenite/ferrite grain boundaries. An exception to this behaviour is represented by sample Fstep, in which unexpected sensitization at δ/δ grain boundaries appeared, probably due to nitride precipitation in those areas and confirmed by a higher DOS when compared to the equivalent solutionized sample .

As demonstrated by microstructure observation together with examination of DL-EPR plots, an intermediate cooling step at low rate from 1100 to 1000 °C followed by water quench is not sufficient to solve the issue of quenched-in nitrides. Quenching from lower temperatures as well as heating to higher solubilization temperatures or applying higher degrees of deformation would be recommended to avoid formation of unwanted phases.

DOS and CPT

CPT results confirmed that the existence of other precipitates might overshadow the effects of χ and σ regarding pitting corrosion, with the exception of specimens Sstep and F025, which exhibited respectively the highest and lowest critical pitting temperatures as well as DOS (see fig. 4.1). The surprising result was that samples SQ, F05 and S025 all exhibited comparable CPT values. Comparing these measurements with microstructural and DL-EPR analysis, it was found that F05 and S025 have both the same volume fraction of σ and χ and same order of magnitude DOS, thus showing correspondence between these parameters. On the other hand, sample SQ showed much lower content of such phases and minimal reactivation, leading to the conclusion that presence of quenched-in nitrides, especially when intragranular, can strongly affect pitting corrosion but appear to have a milder effect on sensitization. In particular, assumptions can be made regarding the ability of DL-EPR to detect more or less deeply sensitized areas: while very

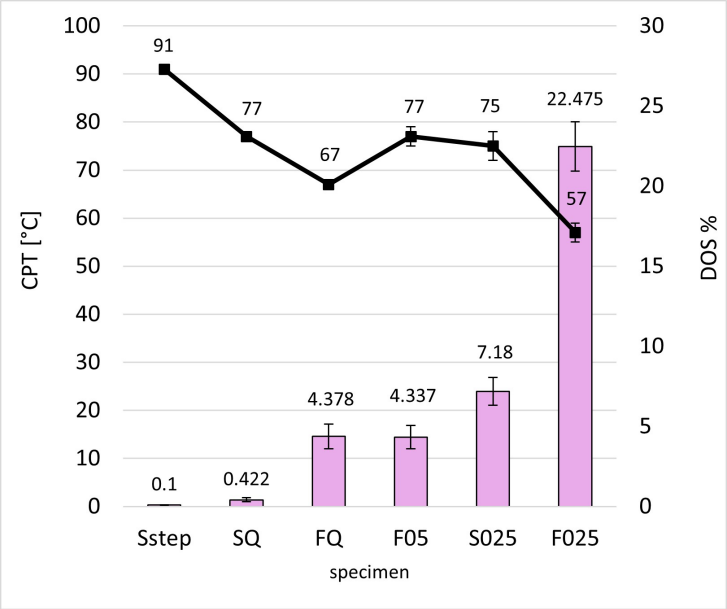

Figure 4.1: *Correlation between the DOS and CPT of UNS J93380 in various thermo-mechanical processing conditions*

susceptible to the extent of Cr-depleted regions created after precipitation of σ, reactivation of small areas where the passive film is weaker might be more difficult. This assumption is also confirmed by the fact that specimen FQ, while exhibiting the same DOS as specimen F05, reported a much lower CPT of 67 °C. A significant presence of precipitated nitrides was infact observed in this sample, which also explains its lower CPT with respect to SQ, probably due to the enhanced nucleation rate provided by plasticized grain boundaries after forging.

Crystallographic orientation

Examination of electro-polished specimens revealed an unusual arrangement of the microstructure, where ferrite seems to have undergone dynamic recrystallization (DRX) along with austenite. As previously mentioned in the introductory chapter, softening mechanisms and texture evolution after hot forging of DSSs can result to be more complex than usually delineated, due to the occurrence of continuous dynamic recrystallization: although quite similar to DRV, it consists in the continuous fragmentation of the grains due to dislocation reorganization caused by plastic strain, which might actually favour new grain nucleation [12].
In order to further investigate the local crystal structure and misorientation gradients developed after plastic strain, analysis of EBSD GROD maps and IPF was carried out. The occurrence of austenite dynamic recrystallization observed during SEM analysis was confirmed by the presence of twins in forged specimen, especially in sample F025. Moreover, in the same specimen small isolated islands of allotriomorphic austenite precipitated at δ/δ grain boundaries as a con-

sequence of σ phase nucleation and deformation.

Future developments

The microstructural analysis carried out during this research mainly focused on characterization of the specimens in terms of precipitated volume fractions of σ and χ phases. Measurement of nitride content by means of SEM image analysis was not pursuited, due to the nano-scale size of such precipitates and the difficult task of distinguishing them from inclusions and porosities. Future investigations will be carried out through transmission electron microscopy (TEM) which, owing to its higher resolving power compared to SEM, allows to detect particles in the order of 1-2 nm.
Regarding the EBSD examinations carried out during this research, which were barely outlined, further examination will be carried out to provide better understanding on DRX and DRV mechanisms that took place during thermo-mechanical processing.

Bibliography

[1] J. Nilsson, *The Sandvik handbook to physical metallurgy – stainless steels and special metals*, vol. 4, ch. 5, pp. 59–77.

[2] R. Gunn, *Duplex Stainless Steels: Microstructure, Properties and Applications*. Woodhead Publishing, Oct. 1997.

[3] H. M. Cobb, *The History of Stainless Steel*. ASM International, Jan. 2010.

[4] International Molybdenum Association (IMOA), *Practical guidelines for the fabrication of duplex stainless steels, 3rd edition*, London (UK), 2014.

[5] V. Kain, *Stress Corrosion Cracking: Theory and Practice*. Woodhead Publishing Series in Metals and Surface Engineering, 2011, ch. 5, pp. 199–244.

[6] M. Knyazeva and M. Pohl, *Duplex Steels. Part II: Carbides and Nitrides*. 2013, ch. 2, pp. 343–351.

[7] I. Calliari, P. Bassani, K. Brunelli, M. Breda, and E. Ramous, "Effect of continuous cooling on secondary phase precipitation in the super duplex stainless steel zeron-100," *Journal of Materials Engineering and Performance*, vol. 22, no. 12, pp. 3860–3866, Dec. 2013.

[8] I. Calliari, M. Pellizzari, M. Zanellato, and E. Ramous, "The phase stability in Cr–Ni and Cr–Mn duplex stainless steels," *Journal of Materials Science*, vol. 46, pp. 6916–6924, 2011.

[9] J. Nilsson, "Super duplex stainless steels," *Materials Science and Technology*, vol. 8, pp. 685–700, Aug. 1992.

[10] J. H. Kang, S. J. Heo, J. Yoo, and Y. C. Kwon, "Hot working characteristics of S32760 super duplex stainless steel," *Journal of Mechanical Science and Technology*, vol. 33, no. 6, pp. 2633–2640, Jun. 2019.

[11] W. Min, L. Baosheng, Z. Shoulu, *et al.*, "Hot Deformation Behavior and Softening Mechanism of As-Cast S32750 Super Duplex Stainless Steel at Low and High Strain Rates," *Journal of Materials Engineering and Performance*, vol. 29, no. 2, pp. 727–738, Feb. 2020.

[12] B. Riad, C. Bellel, K. Charlie, C. Thierry, H. Mohammed, and B. Brigitte, "Microstructure, mechanical behavior, and crystallographic texture in a hot forged dual-phase stainless stee," *The International Journal of Advanced Manufacturing Technology*, vol. 116, pp. 1115–1132, 2021.

[13] M. Ma, H. Ding, Z. Y. Tang, J. W. Zhao, Z. H. Jiang, and G. W. Fan, "Effects of Temperature and Strain Rate on Flow Behavior and Microstructural Evolution of Super Duplex Stainless Steel under Hot Deformation," *International Journal of Iron and Steel Research*, vol. 23, pp. 244–252, 3 2016.

[14] J. A. Pennington, "Effect of hot working and heat treatment parameters on the microstructure and properties of zeron® 100 superduplex stainless steel," Ph.D. dissertation, University of Sheffield, 2018.

[15] R. Mondal, S. K. Bonagani, P. Raut, *et al.*, "Dynamic Recrystallization and Phase-Specific Corrosion Performance in a Super Duplex Stainless Steel," *Journal of Materials Engineering and Performance*, vol. 31, no. 2, pp. 1478–1492, Feb. 2022.

[16] G. Hitchcock, W. Deans, D. Thompson, and A. Coats, "Pin-hole and crack formation in a duplex stainless steel downhole tool," *Engineering Failure Analysis*, vol. 8, pp. 213–226, 3 2001.

[17] S. Kalpakjian and S. R. Schmid, *Manufacturing Engineering and Technology, 7th Edition*. Pearson Education, Inc., 2014.

[18] K. Manisekar and R. Narayanasamy, "Effect of friction on barrelling in square and rectangular billets of aluminium during cold upset forging," *Materials Design*, vol. 28, pp. 592–598, 2 2007.

[19] S. Oh, D. Kim, K. Kim, D. Kim, W. Chung, and B. Shin, "The effect of surface roughness on re-passivation and pitting corrosion of super duplex stainless steel uns s32760," *International Journal of Electrochemical Science*, vol. 18, 2023.

[20] R.Francis, G.Byrne, and G.Warburton, "The corrosion of superduplex stainless steel in different types of seawater," *Rolled Alloys Technology Group*, 2011.

[21] A. El-Yazgi and D. Hardie, "Stress corrosion cracking of duplex and super duplex stainless steels in sour environments," *Corrosion Science*, vol. 40, pp. 909–930, 6 Jun. 1998.

[22] P. Pedeferri, *Corrosion Science and Engineering* (Engineering Materials). Springer International Publishing, 2018.

[23] T. Amadou, H. Sidhom, and C. Braham, "Double loop electrochemical potentiokinetic reactivation test optimization in checking of duplex stainless steel intergranular corrosion susceptibility," *Metallurgical and Materials Transactions*, vol. 35, no. 11, pp. 3499–3513, Nov. 2004.

[24] J. Hong, D. Han, H. Tan, J. Li, and Y. Jiang, "Evaluation of aged duplex stainless steel UNS S32750 susceptibility to intergranular corrosion by optimized double loop electrochemical potentiokinetic reactivation method," *Corrosion Science*, vol. 68, pp. 249–255, Mar. 2013.

[25] D. Assis, Rocha, Margarit-Mattos, Serra, and Mattos, "Practical aspects on the use of on-site double loop electrochemical potentiodynamic reactivation technique for duplex stainless steel," *Corrosion Science*, vol. 74, pp. 250–255, Sep. 2013.

[26] F. Zanotto, "Electrochemical potentiodynamic reactivation: Dual and Single loop EPR," it, *Università di Ferrara*, 2023.

[27] V. Číhal and R. Štefec, "On the development of the electrochemical potentiokinetic method," *Electrochimica Acta*, vol. 46, no. 24, pp. 3867–3877, Aug. 2001.

[28] R. Wang, M. Imagawa, M. Honda, T. Mori, and H. Fukuhara, "Double-loop electrochemical potentiokinetic reactivation behaviour of continuously cooled SUS329J4L duplex stainless steel," *Corrosion Engineering, Science and Technology*, vol. 53, no. 1, pp. 44–50, Mar. 2018.

[29] K. S. De Assis, F. V. De Sousa, M. Miranda, I. C. Margarit-Mattos, V. Vivier, and O. R. Mattos, "Assessment of electrochemical methods used on corrosion of superduplex stainless steel," *Corrosion Science*, vol. 59, pp. 71–80, Jun. 2012.

[30] "ASTM G5-14: Standard reference test method for making potentiodynamic anodic polarization measurements," *ASTM International*, 2021.

[31] M. Martins and L. C. Casteletti, "Microstructural characteristics and corrosion behavior of a super duplex stainless steel casting," *Materials Characterization*, vol. 60, no. 2, pp. 150–155, Feb. 2009.

[32] "ASTM G48-11: Standard test methods for pitting and crevice corrosion resistance of stainless steels and related alloys by use of ferric chloride solution," *ASTM International*, 2020.

[33] X. Q. Xu, M. Zhao, Y. R. Feng, F.-g. Li, and X. Zhang, "A Comparative Study of Critical Pitting Temperature (CPT) of Super Duplex Stainless Steel S32707 in NaCl Solution," *International Journal of Electrochemical Science*, vol. 13, no. 5, pp. 4298–4308, May 2018.

[34] L. Pezzato, M. Lago, K. Brunelli, M. Breda, and I. Calliari, "Effect of the Heat Treatment on the Corrosion Resistance of Duplex Stainless Steels," *Journal of Materials Engineering and Performance*, vol. 27, no. 8, pp. 3859–3868, Aug. 2018.

[35] "ASTM G150-18: Standard test method for electrochemical critical pitting temperature testing of stainless steels and related alloys," *ASTM International*, 2018.

[36] J. Cabrera, A. Mateo, L. Llanes, J. Prado, and M. Anglada, "Hot deformation of duplex stainless steels," *Journal of Materials Processing Technology*, vol. 143-144, pp. 321–325, 2003.

[37] W. Songqing and G. B. C.D. Lundin, "Metallurgical evaluation of cast duplex stainless steels and their weldments," *U.S. Department of Energy*, 2005.

[38] Y. Han, Z. Liu, C. Wu, *et al.*, "A short review on the role of alloying elements in duplex stainless steels," *Tungsten*, pp. 419–438, 5 2023.

[39] J. Jonsson, *Quantitative evaluation of phase fractions in duplex stainless steels*, `https://www.https://www.outokumpu.com/expertise/2020/quantitative-evaluation-of-phase-fractions-in-duplex-stainless-steels`, Accessed: 05/03/2024, 2020.

[40] "ASTM G61-86: Standard test method for conducting cyclic potentiodynamic polarization measurements for localized corrosion susceptibility of iron-, nickel-, or cobalt-based alloys," *ASTM International*, 2018.

[41] J. W. A. Menezes, H. Abreu, S. Kundu, H. K. D. H. Bhadeshia, and P. M. Kelly, "Crystallography of widmanstatten austenite in duplex stainless steel weld metal," *Science and Technology of Welding and Joining*, vol. 14, 2014.

[42] W. Xiao Han, S. Zhi Gang, H. Jian Guo, F. Han, W. Bao Shun, and W. Ming Hua, "Effect of newly formed widmanstatten austenite during high temperature cooling on mechanical properties in UNS S32750 duplex stainless steel," *Materials Science Engineering A*, 851 2022.

[43] D. M. Escriba, E. Materna-Morris, R. L. Plaut, and A. F. Padilha, "Intermetallic phase precipitation in duplex stainless steels during high temperature exposition (conference paper)," Aug. 2018.

[44] J. Nilsson and A. Wilson, “Influence of isothermal phase transformations on toughness and pitting corrosion ofsuper duplex stainless steel saf 2507,” *Materials Science and Technology*, vol. 9, Jul. 1993.

[45] A. J. Ramirez, S. D. Brandi, and J. C. Lippold, “Secondary austenite and chromium nitride precipitation in simulated heat affected zones of duplex stainless steels,” *Science and Technology of Welding and Joining*, vol. 9, pp. 301–313, 4 2004.

[46] E. Bettini, U. Kivisäkk, C. Leygraf, and J. Pan, “Study of Corrosion Behavior of a 2507 Super Duplex Stainless Steel: Influence of Quenched-in and Isothermal Nitrides,” *International Journal of Electrochemical Science*, vol. 9, pp. 61–80, Jan. 2014.

[47] I. Gutierrez-Urrutia, F. Archie, D. Raabe, F.-K. Yan, N.-R. Tao, and K. Lu, “Plastic accommodation at homophase interfaces between nanotwinned and recrystallized grains in an austenitic duplex-microstructured steel,” *Science and Technology of Advanced Materials*, vol. 17, no. 1, pp. 29–36, Mar. 2016.

[48] N. Haghdadi, D. Abou-Ras, P. Cizek, P. Hodgson, A. Rollett, and H. Beladi, “Austenite-ferrite interface crystallography dependence of sigma phase precipitation using the five-parameter characterization approach,” *Materials Letters*, pp. 264–268, 7 2017.

[49] Y. S. Sato and H. Kokawa, “Preferential precipitation site of sigma phase in duplex stainless steel weld metal,” *Scripta Materialia*, vol. 40, no. 6, pp. 659–663, 1999.

[50] G. M. Paolucci, *Appunti dalle lezioni di Metallurgia per la Laurea in Ingegneria Meccanica: Struttura, Proprietà e Comportamento dei Materiali Metallici*. Libreria Progetto, 2002, vol. 1, pp. 229–231.

[51] J. Pardal, S. Tavares, M. C. Fonseca, J. de Souza, R. Côrte, and H. de Abreu, “Influence of the grain size on deleterious phase precipitation in superduplex stainless steel UNS S32750,” *Materials Characterization*, vol. 60, pp. 165–172, 2009.

[52] H. Tsaprailis, M. Ianuzzi, B. Tossey, and L. F. Garfias-Mesias, “Testing of high corrosion resistant metallic coatings for tensioner risers and piston rods exposed to marine environments,” *NACE International*, 09289 2009.

[53] S. Zhang, Z. Jiang, H. Li, H. Feng, and B. Zhang, “Detection of susceptibility to intergranular corrosion of aged super austenitic stainless steel S32654 by a modified electrochemical potentiokinetic reactivation method,” *Journal of Alloys and Compounds*, vol. 695, pp. 3083–3093, 2017.

[54] M. Sun, L. He, X. Li, and P. Li, “Correlation between critical pitting temperature and degree of sensitization of UNS S32750 duplex stainless steel corrosion,” *International Journal of Electrochemical Science*, vol. 15, pp. 1557 – 1570, 2020.

[55] N. Ebrahimi, M. Momeni, M. Moayed, and A. Davoodi, “Correlation between critical pitting temperature and degree of sensitisation on alloy 2205 duplex stainless steel,” *Corrosion Science*, vol. 53, pp. 637–644, 2011.

[56] G. J. Collie and I. Black, “A comparison of cold forming, hot forging, and induction bending as methods of producing duplex stainless steel elbows for high-pressure pipework,” *Proceedings of the Institution of Mechanical Engineers| Part B: Journal of Engineering Manufacture*, vol. 222, pp. 453–465, 2008.

[57] K. Lo, C. Shek, and J. Lai, “Recent developments in stainless steels,” *Materials Science and Engineering R*, pp. 39–104, 65 2009.